UNIVERSITY OF OKLAHOMA

GRADUATE COLLEGE

MOLECULAR BEAM EPITAXY OF ANTIMONY QUANTUM WELLS FOR PROBING TOPOLOGICAL SURFACE STATES

A DISSERTATION

SUBMITTED TO THE GRADUATE FACULTY

in partial fulfillment of the requirements for the

Degree of

DOCTOR OF PHILOSOPHY

By

KAUSHINI S. WICKRAMASINGHE
Norman, Oklahoma
2017

MOLECULAR BEAM EPITAXY OF ANTIMONY QUANTUM WELLS FOR PROBING TOPOLOGICAL SURFACE STATES

A DISSERTATION APPROVED FOR THE
HOMER L. DODGE DEPARTMENT OF PHYSICS AND ASTRONOMY

BY

_____
Dr. Michael B. Santos, Chair

_____
Dr. Rui Q. Yang

_____
Dr. Kieran Mullen

_____
Dr. Sheena Q. Murphy

_____
Dr. Chung Kao

To my loving parents and grandparents

Acknowledgements

First, I owe an enormous gratitude to Dr. Michael Santos, my dissertation advisor, for his constant guidance and encouragement over the years throughout this research. Thank you for providing me an opportunity to join your research group and being an understanding mentor. I enjoyed working with him and his company all the time. Also, his discussions and inputs on physics related topics as well as non-physics related topics gave me an insight into things that are completely new to me. Surely the training and experience I gained through this work will help me to move forward in my carrier.

I would like to convey my sincere gratitude for my reading committee members, Dr. Sheena Murphy, Dr. Kieran Mullen, Dr. Chung Kao, and Dr. Rui Yang, for their suggestions and helpful feedback throughout this work. I also would like to thankfully acknowledge Dr. Matthew Johnson for his support.

I want to thank Tetsuya Mishima for his timely efforts in support of my research and lab work and providing me cross-sectional TEM images included in the dissertation. My thanks are due to Joel Keay and Preston Larson, for the training on characterization techniques. A big thanks to Chomani Gaspe for training me on MBE and initial lab work. My sincere thanks to my group members, Lu Li and Jeremy Massengale, and former group members Mukul Debnath, Sangeetha Vijeyaragunathan and Ye Hao for all their support. I also want to specially thank Shayne Cairns and Liu Zhonghe for their kind support towards this goal. I further would like to acknowledge all faculty and staff from the Homer L. Dodge Department of Physics and Astronomy,

for their generous help. I want to express my gratitude to the Graduate College and International Student Services at OU for doing their service responsibly.

High magnetic field data was taken at the National High Magnetic Field Laboratory (NHMFL) in Tallahassee, FL. A special thank goes to administrative and technical staff at NHMFL for allowing us to use their facility and every support given during our visits there. The dissertation research was supported by the National Science Foundation under Grant Nos. DMR-1207537 and DMR-1229678. I would also like to thankfully mention the financial support granted for the research travel, by Scholarships from Arts and Sciences and Graduate Students Senate (GSS) at OU.

Thank you, all of my dear friends at OU for making my graduate student life more bearable and often fun. Above all, I am indebted to my loving parents and my only sister for being with me and inspired me always.

Table of Contents

List of Tables

List of Figures

Abstract

A topoelectronic transition was predicted for an Sb quantum well (QW) as a function of QW thickness. Bulk Sb is a semimetal with a negative bandgap, with neither the conduction band minimum nor the valence band maximum at the Γ point. The Dirac point for the topological surface states is at the Γ point. In this dissertation, we present a detailed structural analysis of ultra-thin Sb QWs grown using a novel molecular beam epitaxy procedure that controls the thickness of the QW down to a few angstroms. Also, we studied the electronic properties of the topological surface states by suppressing the bulk conductivity through quantum confinement and enhancing the surface conductivity through remote n-type doping at the Γ point.

Conductivity measurements on undoped QWs (0.7 to 6 nm thick) show a suppression of the bulk states, such that the surface conductivity is ~20% of the total conductivity for a 3.8 nm-thick QW. Interpretation of Hall-effect measurements, which nominally indicate p-type conduction for undoped QWs, was complicated by the presence of both electrons and holes.

Therefore, we carried out experiments to populate the topological electron states by doping the GaSb barrier layer with tellurium (Te) atoms, creating donor states at the Γ point. At the Γ point of the QW, the topological electron states have a lower energy than any of the bulk conduction band minima. Remote n-doping of Sb QWs was confirmed by analyzing the spacer dependence of the Hall coefficients in a low magnetic field of 0 – 0.15 T and a temperature of 20 K.

From high field magnetoresistance measurements, we deduced that holes still contributed significantly to the conductivity even though the Hall voltage indicated

nominally n-type conduction. By further analyzing the fine features in the longitudinal resistance, we deduced that the surface states in a remotely-doped QW have an electron concentration of ~3.3×10^{12} cm^{-2} and a mobility of ~1600 – 2000 $cm^2/V\cdot s$. Assuming the initial electron concentration, before doping the Sb QW, is 2×10^{12} cm^{-2} (i.e. the lowest possible value estimated from theory), we calculated that the maximum amount transferred to the QW is ~1.3×10^{12} cm^{-2} when using GaSb barrier material and a Te-doping concentration of 1×10^{18} cm^{-3}. The fine features that we interpreted as Shubnikov de Haas oscillations are of the order of the noise level; thus we cannot be certain of this interpretation. Therefore, we suggest future experiments to resolve this uncertainty.

Chapter 1: Introduction

The different states of matter were first categorized very crudely as solids, liquids or gases. However, some states of matter, such as superfluids, plasmas, and liquid crystals, behave in ways that are much more complex than these categories would suggest. Despite this huge variety, there are many important phenomena in crystalline solids that have been understood for many decades. For example, a material being a conductor, insulator, semiconductor or a semimetal was explained using the theory of electronic bands during the first half of the 20^{th} century. The discovery of the Quantum Hall Effect in 1980 highlighted the important roles of disorder and edges states in determining the electrical conductivity of two-dimensional electron systems. In the same era, physicists started using topological concepts in mathematics to understand the phases of matter exhibited in dramatic discoveries of exotic materials. In 2016, the Nobel Prize in Physics was awarded to David J. Thouless, F. Duncan M. Haldane, and J. Michael Kosterlitz for their pioneering work in using advanced topological concepts in mathematics to study strange phases or states of matter [1]. Recent applications of topological concepts have led to the predictions and experimental discoveries of topological insulators (TI) in both two dimensions and three dimensions [2, 3].

Topological insulators are a new phase of matter in which the bulk conductivity is like that of a typical insulator, but the conductivity is novel at the surfaces or edges. TIs can be divided into two types, 2D and 3D TIs. The edges are conducting in 2D TIs whereas the surfaces are conducting in 3D TIs. These edge states and surface states are spin locked, carry current only in one direction, and are predicted to exhibit quantized conductance. Moreover, these charge carriers are highly protected from backscattering.

2D TI states were first experimentally observed in the CdTe/HgTe material system [3] whereas the 3D TI states were observed in alloys of $Bi_{(1-x)}Sb_x$ [4]. After the initial discovery, many alloys were found to exhibit 3D TI states. Yet all these materials have a major drawback. Although they are expected to be good insulators in their bulk, in reality, significant bulk conduction has been observed due to unintentional doping or crystalline defects. Because of this, transport measurements have been unable to isolate the surface conduction due to TI states from the bulk conduction. By gating and doping, efforts have been made to overcome this issue.

In this dissertation, we chose to investigate the transport properties of elemental Sb, which was theoretically predicted to exhibit a 3D TI nature for a thickness range of 2.7 – 7.8 nm [5]. Bulk Sb is a semi-metal, but when its thickness is reduced below 7.8 nm, Sb becomes a 3D TI due to suppression of bulk conduction via quantum confinement. One advantage of an elemental TI is that the simple stoichiometry may reduce unintentional doping and defects.

The dissertation chapters are organized as follows: Chapter 2 is dedicated to briefly reviewing the theory of topological insulators, mainly Z_2 topological insulator, and outlining the history of TIs.

Chapter 3 gives an overview of Molecular Beam Epitaxy, components and calibration. Also, structural characterization using Field-Emission Scanning Electron Microscopy (FESEM) and Atomic Force Microscopy (AFM) are discussed briefly towards the end of this chapter.

In Chapter 4, structural properties are discussed in depth using FESEM and AFM microscopy. Fine features of the Sb layer are analyzed and discussed by using a ball and stick model and considering the effects of physical strain.

Chapter 5 gives an overview of electrical measurements and theory. This chapter discusses Hall-effect measurements, and briefly describes Landau levels and Shubnikov de Haas (SdH) oscillations, which we used to analyze the electrical properties of the Sb/GaSb structures.

Chapters 6 and 7 include electrical properties of undoped Sb QW and remotely-doped Sb QWs. In these chapters, we extract the contribution from the surface states for the measured conduction. Further, for doped Sb QWs, the position of the Fermi level, and the mobility and density of surface electrons are deduced using Hall-effect measurements and SdH oscillations in high magnetic fields up to 18 T.

Chapter 2: Theory and History of Topological Insulators in a Nutshell

2.0 Introduction

The widely-known classification of a material as being a conductor (or metal), semimetal, semiconductor or an insulator, is explained using the theory of electronic bands. The conduction or valence band is partially filled in a metal, while both the valence and conduction bands are partially filled in a semimetal (see Figure 2.1). Semiconductors and insulators have a completely filled valence band and an empty conduction band at 0 K and the Fermi level lies in the band gap. If the band gap is less than ~3 eV, the material is considered a semiconductor because there is significant thermal excitation of electrons across the bandgap at room temperature. If the band gap is more than ~3 eV, the material is considered an insulator. When the topological order is included in the classification, semiconductors/insulators can be divided into two categories, trivial insulators or (non-trivial) topological insulators. Trivial insulators include BN, MgS, and diamond. A topological insulator (TI) has an insulating interior volume, or bulk, like a trivial insulator, but it also has gapless surface states (edge states in 2D) with conducting states protected by time reversal symmetry. In this chapter, we discuss topological insulators by introducing topology and then the analogy of the quantum Hall effect and topological insulators. Further, we briefly discuss Z_2 topological insulators in 2D and 3D, and finally outline the history of TIs.

2.1 Topological Order and Quantum Hall Analogy to TIs

Topology is the study of geometrical properties and spatial relations which are unaffected by smooth changes in the shape or size of the objects. Topology is connected

to the genus g of a geometrical object. For a 2D surface, g counts the number of holes and the object is topologically classified accordingly.

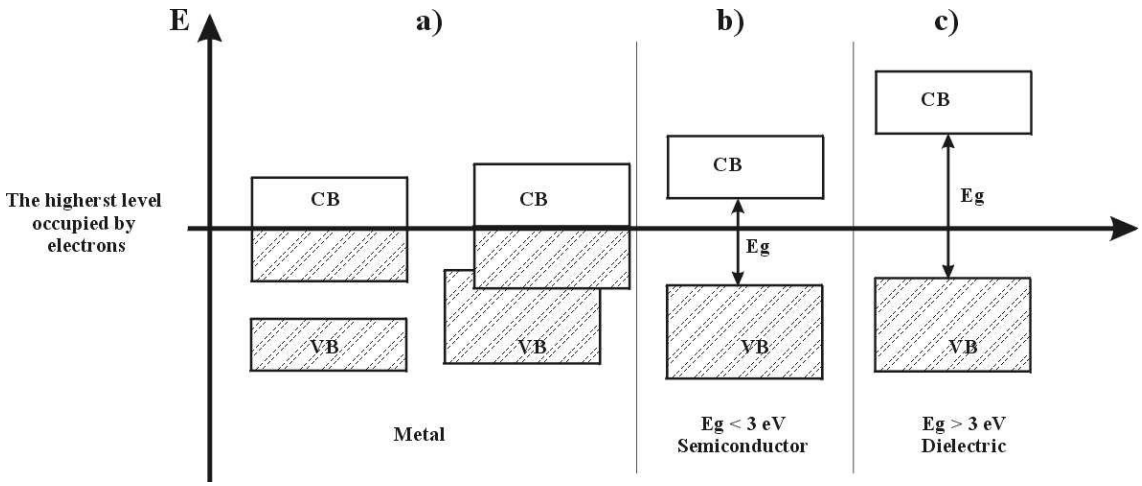

Figure 2.1. Schematic diagram representing electron population in (a) a metal, (b) a semiconductor and (c) an insulator. A metal with overlapping bands would be a semimetal if the highest level occupied by electrons, passed through the overlapping bands.

.

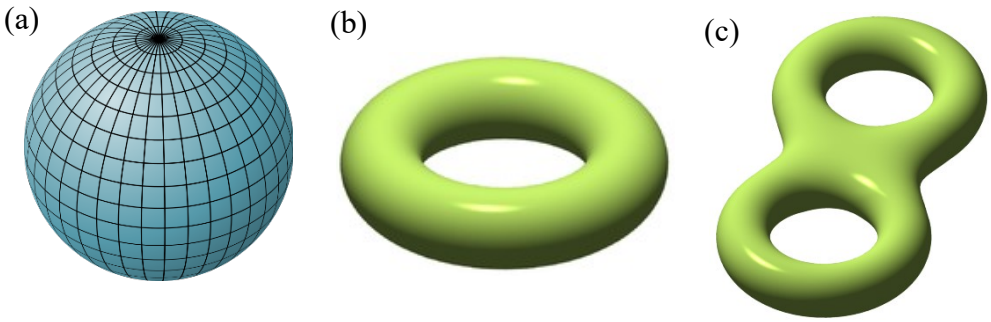

Figure 2.2. The genus g of an object. (a) For a sphere, g=0, (b) a donut g=1, and (c) a pretzel $g = 2$.

Let's consider a simple illustration: a sphere has $g = 0$, a donut has $g = 1$ and, a pretzel has $g = 2$, as shown in Figure 2.2. A donut cannot be smoothly deformed into a sphere without filling the hole. Hence these two belong to two different topological classes.

There is also a mathematics theorem [6] which states that the integral of a Gaussian curvature over a closed surface is a quantized topological invariant and its value is related to g. Similarly, to distinguish a normal insulator from a topological insulator, we define a topological invariant $n \epsilon \mathbb{Z}$ ($\mathbb{Z}$ is an integer) called the Chern invariant which is also an integral of a related curvature [7].

Topological order has been used to characterize the correlated fractional quantum Hall states [8] of a 2D electron system in GaAs. In addition, Thouless et al. in 1982 [9] used topological considerations to describe the integer quantum Hall (IQH) effect observed in a 2D electron system in Si or GaAs. Topological insulators are analogs to IQH states. The IQH states are formed when electrons confined in 2D are subjected to a strong perpendicular magnetic field: electrons move in circular orbits with cyclotron frequency ω_c, leading to quantized Landau levels with energy $\varepsilon_{nk} = (m + \frac{1}{2})\hbar\omega_c$ with integer values for m (see Figure 2.3). When N Landau levels are completely filled and the rest are empty, an energy gap separates the occupied and empty states like for an insulator. But at the perimeter of the sample, electrons exhibit skipping orbits which allows conduction at the edges that gives rise to quantized Hall conductivity,

$$\sigma_{xy} = N\frac{e^2}{h} \tag{2.1}$$

To explain the difference between the integer quantum Hall state and the ordinary insulator using topological considerations, Thouless, Kohmoto, Nightingale, and den Nijs (TKNN) [9] used the topological invariant $n \epsilon \mathbb{Z}$ ($\mathbb{Z}$ is an integer), known as the Chern invariant. TKNN explained the physical nature of the Chern invariant using a Berry phase associated with the Bloch wave function $|u_m(\boldsymbol{k})>$. Given that there are no accidental degeneracies when k traverses around a closes loop, $|u_m(\boldsymbol{k})>$ acquires a well-defined Berry phase given by a line integral of $\mathcal{A}_m = i\langle u_m|\nabla_k|u_m\rangle$. This can be expressed as a surface integral of Berry flux $\mathcal{F}_m = \nabla\times\mathcal{A}_m$. The Chern invariant is the total Berry flux in the Brillouin zone,

$$n_m = \frac{1}{2\pi}\int d^2k \;\; \mathcal{F}_m \tag{2.2}$$

When the sum is over all occupied bands, the total Chern number n is obtained and equal to N in equation 2.1

In 1988, Haldane et al. [10] showed that the IQH effect results from breaking of time reversal symmetry for a 2D semimetal. He obtained a Chern invariant of ± 1 for an IQH state. However, if the inversion symmetry is broken, $n = 0$ and the material is a trivial insulator/semiconductor. Geometrical space is analyzed to calculate the genus of an object. The reciprocal space in a Brillouin zone is used to calculate the Chern number, or the topological invariant, for a topological insulator. This analogy is shown in Figure 2.3: the insulator has a Chern number $n = 0$, analogous to $g = 0$, and an IQH state has $n = 1$, analogous to a donut with $g = 1$.

2.2 Z_2 Topological Insulators in 2D and 3D

In order to observe the IQH state, a strong magnetic field is needed. In contrast, a topological insulator exhibits edge states without a magnetic field, as a result of strong spin orbit coupling. Unlike in an IQH state, the TI surface/edge states are protected from elastic backscattering due to time reversal (TR) symmetry [7]. Another difference is the edge states are chiral in an IQH state, but non-chiral in a TI [11]. In a TI, the edge states are "helical," indicating that their spin is locked at a right angle to their momentum. Along the same edge/surface, a spin-up electron propagates in the opposite direction to a spin-down electron (see Figure 2.4). It is possible to transmit these helical edge states through strong disorder by flipping the spin and changing the path by $\pi - (-\pi) = 2\pi$.

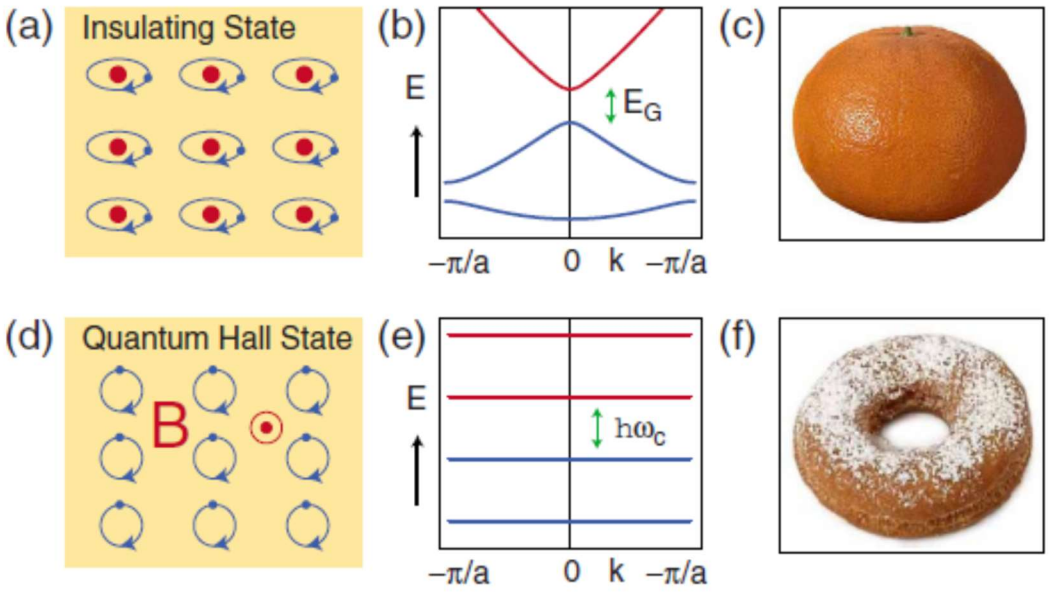

Figure 2.3. Trivial and non-trivial insulators. (a)-(c) insulating state. (a) An atomic insulator. (b) A simple model of an insulating band structure. (c) An object with g =0. (d)–(f) A quantum Hall state. (d) Cyclotron motion of electrons. (e) Landau levels, which may be viewed as a band structure. (f) An object with g =1. The Chern number n that distinguishes the two states is a topological invariant analogous to the genus [7].

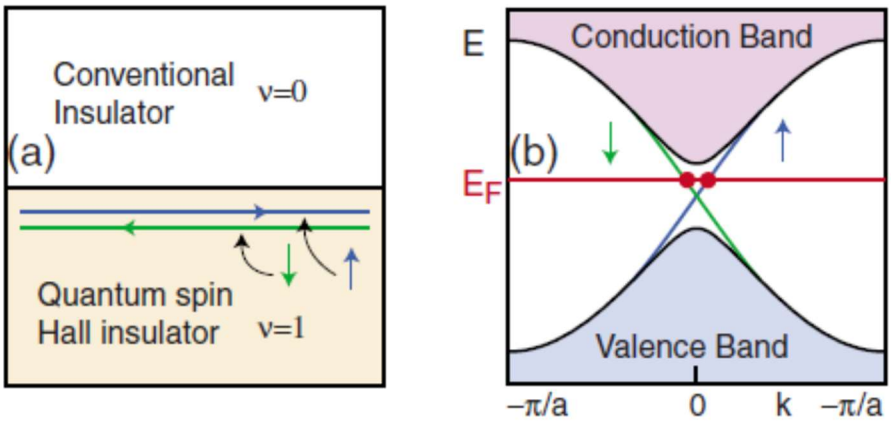

Figure 2.4. Edge states in the quantum spin Hall insulator (QSHI). (a) The interface between a QSHI and an ordinary insulator. (b) The edge state dispersion in the graphene model in which electrons with up and down spins propagate in opposite direction [7].

We can distinguish normal insulators from TIs by calculating the distinct topological invarient Z_2 which is analoguos to the TKNN invarient we discussed in section 2.1. The Z_2 class consists of spin $1/2$ particles. Under time reversal symmetry, each energy level is at least two-fold degenerate, which is known as the Kramer's degeneracy theorem. Due to this theorem, $Z_2(\upsilon_0)$ can equal either 0 or 1 in 2D. A 2D topological insulator is also called a quantum spin Hall insulator (QSHI) where a single Z_2 topological invarient governs the effect [12]. In 3D there are four $Z_2(\upsilon_0, \upsilon_1, \upsilon_2, \upsilon_3)$ invarients that distinguish 16 phases with two general classes, weak TIs (WTIs) and strong TIs (STIs). WTIs have an even number of Dirac points while STIs have an odd number of Dirac points (see Figure 2.5). A WTI has $\upsilon_0 = 0$ and is similar to a QSH state, but is destroyed by disorder. In contrast, a STI has $\upsilon_0 = 1$, is robust, and exhibits novel "topological metal" surface states.

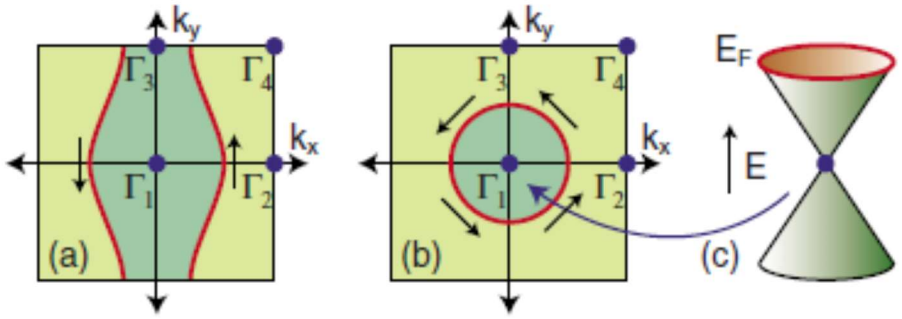

Figure 2.5. Fermi circles in the surface Brillouin zone for (a) a weak topological insulator and (b) a strong topological insulator. (c) In the simplest strong topological insulator, the Fermi circle encloses a single Dirac point [7].

2.3 An Outline of the Experimental Discoveries of TIs

In general, materials composed of elements which have strong spin orbit coupling like Bi, Sb, Te and Hg enable topological surface states. 2D TI states were first experimentally observed in the CdTe/HgTe material system [3]. In a sufficiently-thick HgTe quantum well with CdTe barriers, the inversion of bulk bands leads to a Dirac like dispersion of surface bands, which results in QSH states. A plateau of $2e^2/h$ in the conductance was observed for quantum wells of thickness > 6.3 nm in the nominally insulating regime. The effect was observed irrespective of the sample width, implying that the electron transport is through the edge states (see Figure 2.6) [3]. With an applied magnetic field, the residual conductance vanished in accordance with the theory. An applied magnetic field breaks time reveral symmetry, and hence the quantized conductance vanishes.

A 3D TI was first predicted by L. Fu and C.L. Kane [13] for $Bi_{(1-x)}Sb_x$ with a composition of $0.09 < x < 0.18$ and subsequently experimentally observed [4]. Topological surface states have been mapped using angle resolved photo emission spectroscopy, ARPES, as shown in Figure 2.7. A Kramer's doublet point was observed

at ~ $15 \pm 5\ meV$ below the Fermi level, E_F at $k = \bar{M}$. The Fermi level in the bulk band gap crosses the surface states at five points, predicting the observed STI. 3D TI states were later reported for Bi_2Se_3 [14] and Bi_2Te_3 [15], and a ternary alloy of $(Bi_xSb_{1-x})_2Te_3$ [16] with a tuned Sb composition. Unfortunately, all these materials have a major drawback. Although they are expected to be good insulators in their bulk, in reality, significant bulk conduction has been observed due to unintentional doping or crystalline defects. Because of this, transport measurements have been unable to isolate the surface conduction due to TI states from the bulk conduction. By gating and doping, efforts have been made to overcome this issue. In the ternary alloy $(Bi_xSb_{1-x})_2Te_3$, the bulk conduction was two orders of magnitude smaller than in other TI materials [14].

In 2012, Zhang et al. theoretically predicted that semimetallic Sb can undergo topoelectronic phase transitions as the thickness of the Sb film is reduced. A thick layer of Sb is a semimetal in the bulk, but has topological surface states. The calculated band structure in Figure 2.8 (b) shows that when the Sb film thickness is less than 7.8 nm, quantum confinement will open a bulk gap and 3D TI behavior is expected. Below 2.7 nm, a 2D QSH state is predicted. A film with a thickness less than 1 nm, is predicted to be a trivial semiconductor [5]. Bian et al. reported a mapping of 3D topological surface states from ARPES measurements of Sb grown on a Si(111) substrate [17]. The ARPES map of the band structure for a 4 BL (1.5 nm) Sb film (Figure 2.9 (a)) is in fairly good agreement with the calculated band structure shown in Figure 2.9 (b). Yet no transport measurements were reported. In this dissertation, our goal was to investigate the transport properties of 3D topological insulator states in an Sb quantum well. The major advantage of an elemental TI is that the simple stoichiometry may reduce unintentional

doping and defects. Hence it may be possible to discriminate the conductivity due to surface states from the conductivity of the bulk.

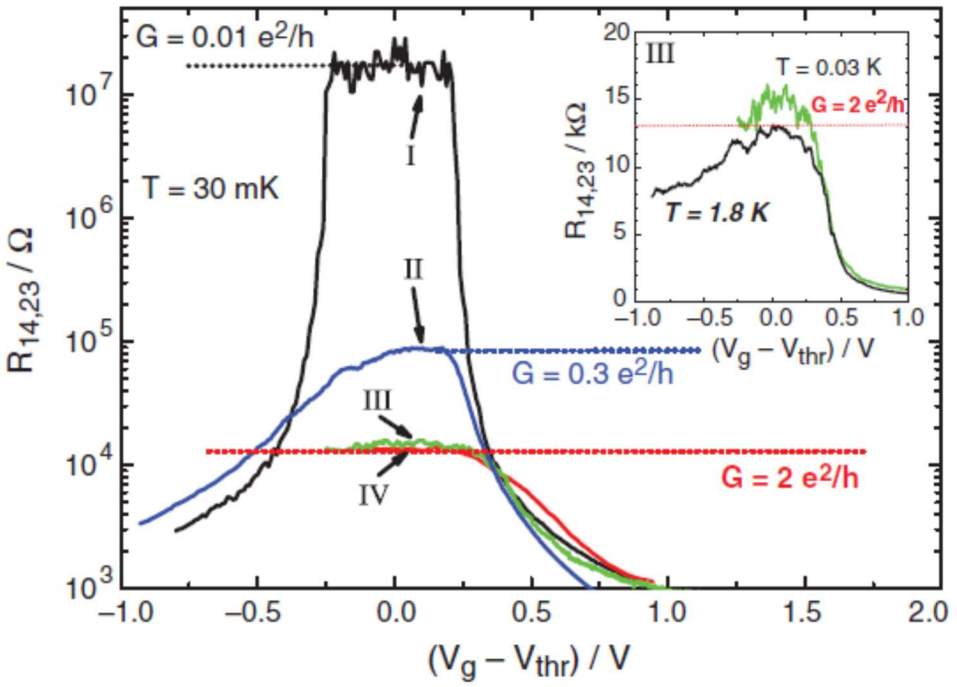

Figure 2.6. At 30 mK, there is a conductance plateau of $2e^2/h$ for a QSH state [3].

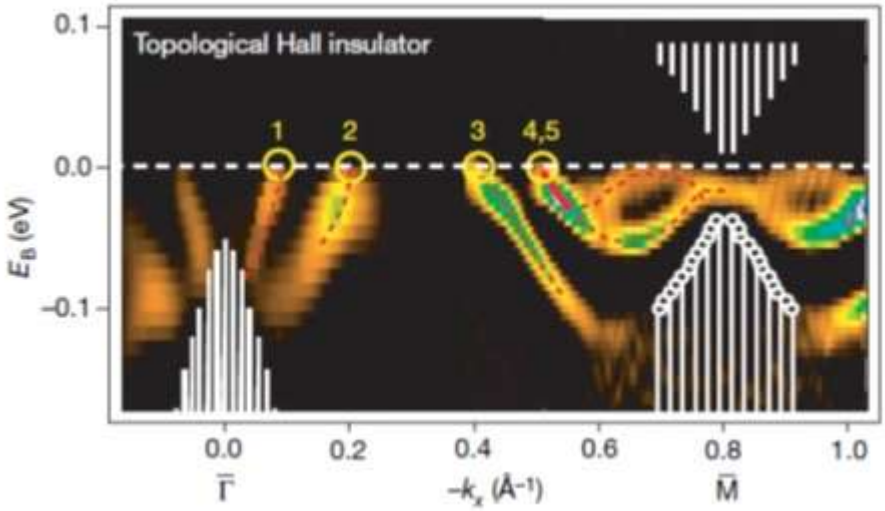

Figure 2.7. ARPES mapping of topological gapless surface states of Bi0.9Sb0.1. A Kramer's degeneracy is observed and labeled as 4, 5 [18].

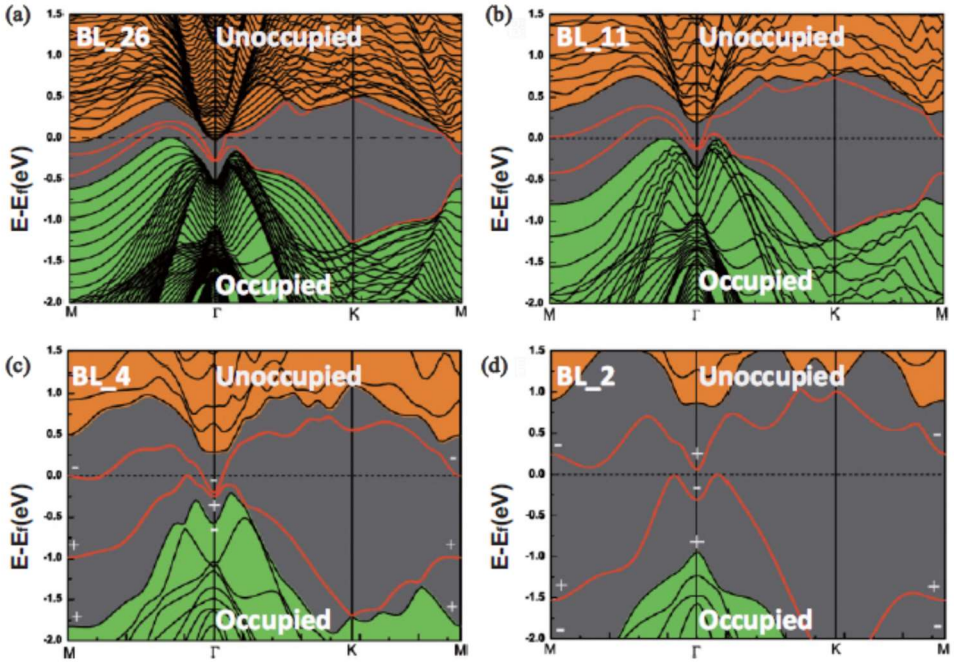

Figure 2.8. Band structure calculations for thin Sb layers undergoing topoelectronic phase transitions. (a) Sb in a semimetallic state, (b) 3D topological insulator state for 11 BLs, (c) 2D QSH state for 4 BLs , and (d) trivial insulator [5].

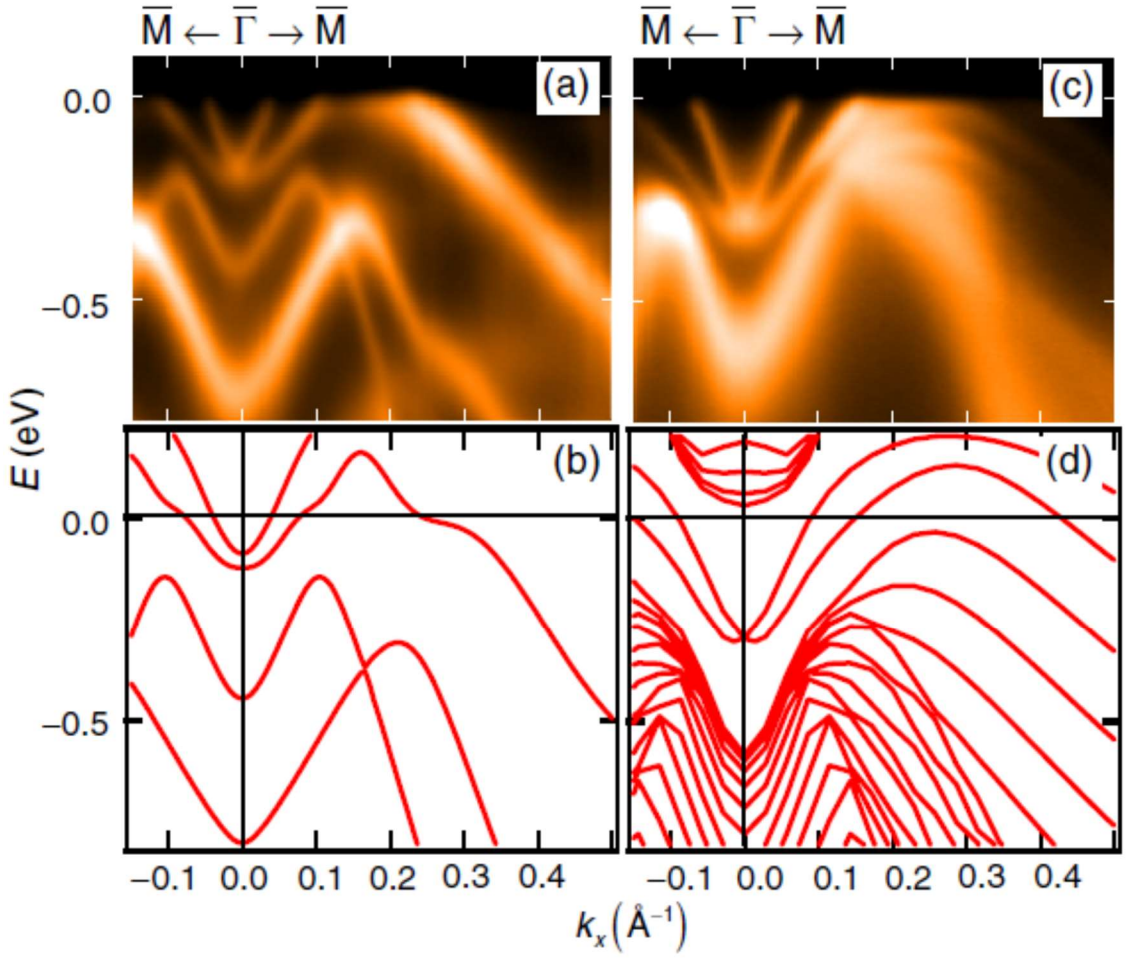

Figure 2.9. (a) ARPES map for 4 BL Sb film taken along $\bar{\Gamma}$-$\bar{M}$ direction. (b) Calculated band structure for 4 BL free standing film. (c) ARPES map for a 20 BL Sb film taken along $\bar{\Gamma}$-$\bar{M}$. (d) Calculated band structure for a 20 BL free standing film. Figure taken from [17].

Chapter 3: Techniques of Epitaxial Growth and Structural Characterization

3.0 Introduction

Molecular beam epitaxy (MBE) was first developed in the 1960s and 1970s to grow layers of single crystals made of compound semiconductor material. This is particularly a prominent method to realize ultra-thin layers of precise thickness. The concentration of unintentional impurities is very low due to an ultra-high-vacuum (UHV) growth environment and high-purity source materials. MBE can produce complex structures with exotic properties like topological insulators and superconductors. Thus, this method is well suited for our studies of Sb quantum-well structures. Structural characterization plays an important role in optimizing procedures for producing high quality materials. In this chapter, we briefly discuss the main components and operation of the MBE systems and describe two ex-situ material characterization techniques, field emission scanning electron microscopy (FESEM) and atomic force microscopy (AFM).

3.1 Molecular Beam Epitaxy

MBE is a technique to grow a crystalline material layer by layer (that is epitaxially) using a molecular beam produced by thermally evaporating an elemental source which is then deposited onto a heated crystalline substrate to form the crystalline material. To grow a layer with high-purity we use extremely pure material sources, a purity of 99.9999999% for group III materials (In, Ga and Al) and 99.99999% purity

for group V materials (As and Sb). Also, the full MBE system is operated under ultra-high vacuum conditions of ~ 10^{-10} - 10^{-11} Torr.

Two standalone MBE systems, a 1993 Intevac modular Gen II and a 2013 beta version of the Veeco GENxplor are installed in the Physics and Astronomy department. Figure 3.1 shows a schematic diagram of a typical MBE growth chamber [19] and Figure 3.2 shows photographs of the two MBE systems installed in our laboratory at the University of Oklahoma. Both MBE systems consist of three main chambers; an entry-exit or load-lock chamber, a buffer chamber and a growth chamber. All three chambers are isolated from each other via a gate valve. The wafers are transferred between the chambers using a trolley. We discuss the individual chambers in detail below.

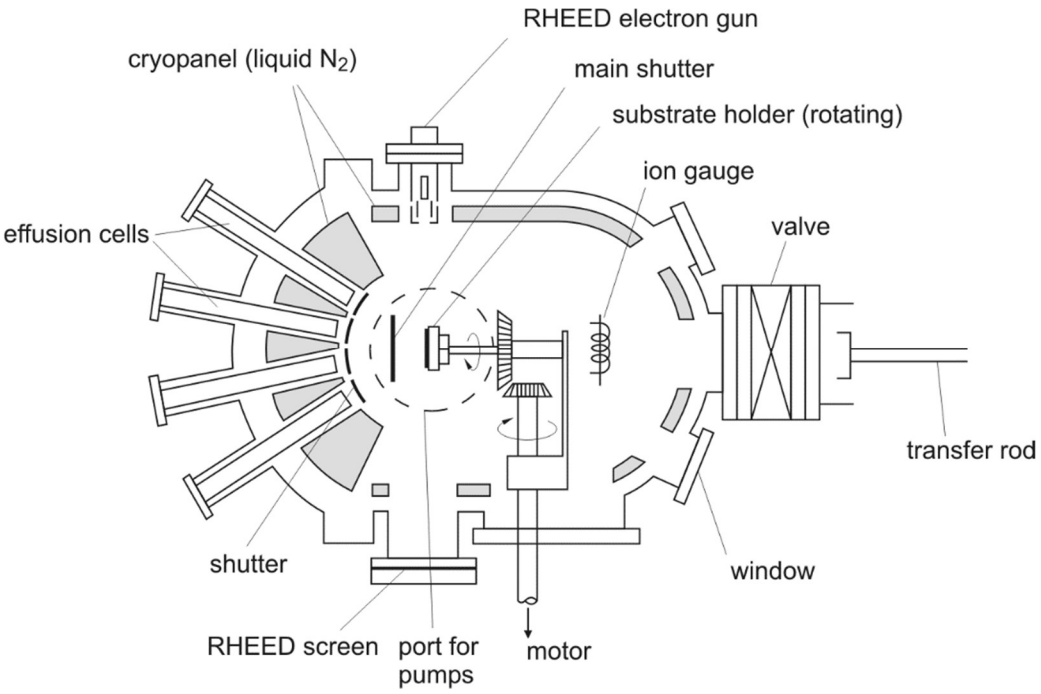

Figure 3.1. Schematic of a Molecular Beam Epitaxy (MBE) growth chamber [19].

(a)

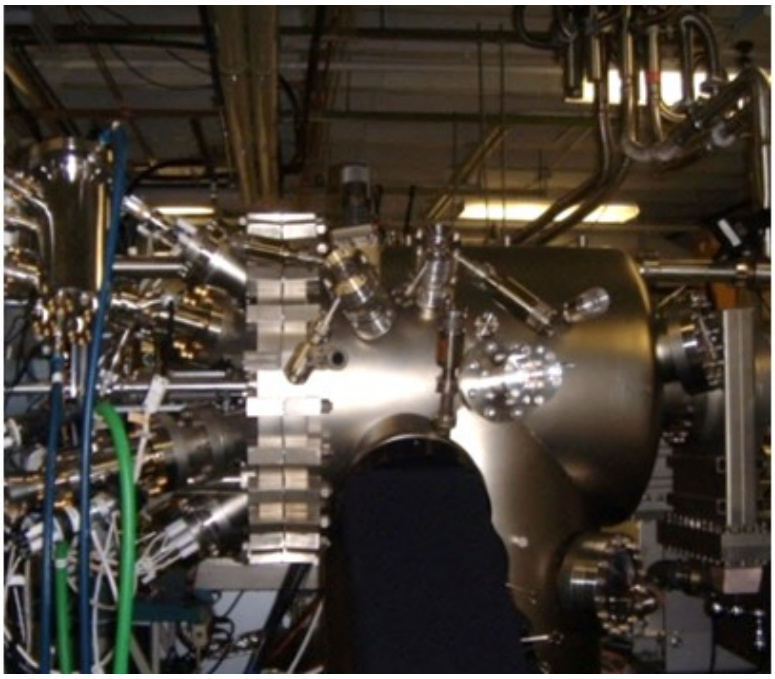

(b)

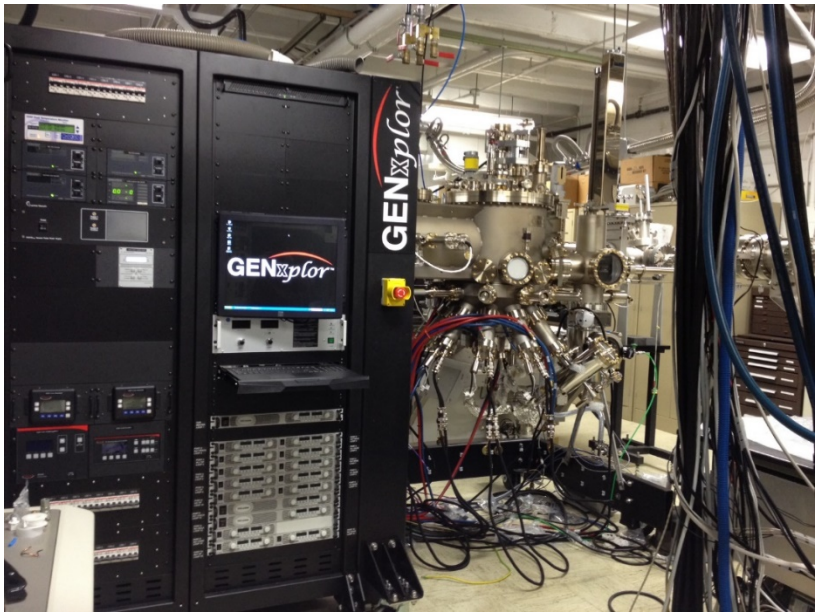

Figure 3.2. Two standalone molecular beam epitaxy systems at the University of Oklahoma. (a) Growth chamber of the Intevac Modular Gen II system. (b) The beta MBE version of the Veeco GENxplor.

3.1.1 Entry-Exit Chamber (Load-Lock)

The entry-exit chamber is used to load the substrates into the system and bring the grown wafers out of the system without exposing the other chambers to atmospheric pressure. We use dry nitrogen gas to vent this chamber and let the nitrogen gas flow throughout the time the chamber is open to prevent gas molecules outside the chamber from entering the system. Once the wafer exchange is completed in the Gen II, we use a combination of two pumps, a molecular drag pump and a scroll pump, to pump the entry-exit chamber from atmosphere to ~ 10 mTorr. After the chamber reaches this value, we switch to a small cryopump. When the vacuum is down to ~5×10^{-7} Torr, the entry-exit chamber is baked at 200 °C for at least 2 hours to outgas the substrates and the holders. The ion gauge mounted in the entry-exit chamber reads a vacuum of the order ~ 10^{-9} Torr after baking is completed. For the GENxplor, we use only a scroll pump for the initial rough pumping and then a turbo pump for reaching ultra-high vacuum.

3.1.2 Buffer Chamber

This is the intermediate chamber connected directly to the growth chamber and the entry-exit chamber. It is maintained at a vacuum of ~ 10^{-10} Torr by an ion pump for both the Gen II and GENxplor. The buffer chamber serves the purpose of isolating the growth chamber from the entry-exit chamber and thus helps to maintain the high purity environment in the growth chamber. Further, we have installed a heated station to degas the substrates before growth in the Gen II. This chamber also provides a space to temporarily store wafers before and after growth.

3.1.3 Growth Chamber

A schematic diagram of a typical MBE growth chamber is shown in Figure 3.1. The major components of the growth chamber include the following:

a) Liquid nitrogen cooled cryoshrouds enclosing much of the volume around the substrate holder

b) Effusion cells to produce the atomic or molecular beams

c) Shutters to mechanically switch the beam fluxes on and off

d) Rotatable substrate holder and heater

e) Ion gauges to monitor the vacuum and the beam flux

f) RHEED set-up

g) A mass spectrometer to analyze residual gases and for leak detection

The feasibility of growing high-quality epilayers in the chamber is due to the cleanliness in the growth environment. To achieve this, two conditions are necessary:

1) Use high purity source materials in the effusion cells

2) Use a strong vacuum pumping system: a combination of a cryopump, ion pump or turbo pump.

Since UHV is a result of the steady state between the rate of gas evolution and the pumping rate, these are not sufficient conditions. Hence, two more conditions are applied in constructing an MBE system.

1) MBE components made of materials that outgas negligibly at higher temperatures, like molybdenum and tantalum. The crucibles are made of high purity pyrolytic boron nitride, which has low outgassing up to a temperature of ~1500 °C.

2) Minimize the molecules and atoms escaping from the walls of the chamber and heated components of the apparatus reaching the substrate. This is achieved by the liquid nitrogen cooled cryoshrouds enclosing the volume around the substrate holder [20].

There are beam sources for group-III mono-atomic elements, namely indium (In), Gallium (Ga), and aluminum (Al), and group-V tetra-atomic elements, namely arsenic (As_4) and antimony (Sb_4), and three dopant elements, beryllium (Be), Silicon (Si) and tellurium (GaTe source material). The group-V cells have two heating zones, the bulk zone and the cracking zone. The cracking zone dissociate tetramers into dimers (As_2 and Sb_2). In the GENxplor, the group-V sources have needle valves to adjust the group-V fluxes. In the Gen II, the As cell has a needle valve but the Sb cell does not.

Effusion cells are operated at high temperatures in the range of 500 – 1500 °C to produce sufficient beam fluxes. The crucible material is pyrolytic boron nitride (PBN) because of their weak chemical activity even at these high temperatures. A cell temperature is measured using a thermocouple in contact with either a side wall or the bottom of the crucible. The cells are thermally isolated from each other by a chilled-alcohol shroud in the Gen II or a liquid-nitrogen shroud in the GENxplor. In addition, cooling water is used for cooling some of the cells. To grow high quality crystals, materials of high purity are used as source materials, with the majority having a purity of > 99.99999%.

The shape and dimensions of the crucible and the distance between the substrate and the source cells determine the homogeneity of the growth rates [21]. The fluxes incident on the substrate are controlled by the cell temperatures, which are regulated

through proportional (P), integral (I), and derivative (D) controllers. Because of the UHV condition in the system, growth takes place in the molecular regime (i.e the mean free path of the atom or the molecule is larger than the geometrical size of the growth system). The very short operation times of the shutters, typically <0.1 s, allow the growth of heterostructures with abrupt interfaces. A concentration gradient across the wafer which may occur due to converging beam angles, is eliminated by rotating the substrate using a CAR (continuous azimuthal rotation) assembly. The typical rotation speed is 25 rpm.

The growth chambers are equipped with two ion gauges. The one far from the beams is used to measure the vacuum in the growth chamber. The second one can be placed in the substrate position to measure the flux incident on the wafer surface in terms of pressure. This is called the beam equivalent pressure (BEP).

3.1.4 Comparison of Intevac Gen II module and Veeco GENxplor

BE system	Intevac Modular Gen II	Beta Version of Veeco GENxplor
Orientation	• Horizontal	• Vertical
Entry-exit chamber	• Cylindrical tube of ~1m length • Uses a cryopump • Takes ~2 hr to pump down to 10^{-7} Torr • Pressure is low 10^{-9} Torr	• Cube of ~ 1ft ×1ft ×1ft • Uses a turbo pump • Takes <10 minutes to down to 10^{-7} Torr • Pressure is low 10^{-9} Torr
Buffer chamber	• Cylindrical tube, >1m long • Uses an ion pump and a Titanium sublimation pump • Pressure is low 10^{-10} Torr • 2 horizontal trolleys which each can hold 16 wafers • Has a heated station • Transfer rods are magnetically coupled	• Cylindrical tube, ~0.5m long • Uses only an ion pump • Pressure is low 10^{-10} Torr • 1 vertical trolley which can hold 7 wafers • No heated station • A different mechanism than in Gen II
Growth chamber	• Uses a cryopump and an ion pump • Liquid nitrogen cryoshroud • All cells are thermally isolated with a chilled alcohol (-37 °C) shroud • Group V cells also use chilled water for cooling • Pressure is low 10^{-10} Torr • 8 ports with effusion cells, no more ports available	• Uses a cryopump and an ion pump • Liquid nitrogen cryoshroud • All cells are thermally isolated with a liquid nitrogen shroud and chilled water shrouds • Pressure is low 10^{-10} Torr • 8 ports with effusion cells, 2 more ports available

	• 1 indium cell • As cell has a valve • Installed an Sb cell with a valve in 2016 • Single dopant cells of 5cc • No Te dopant source • No interlocks in use	• 2 indium cells • As cell has a valve • Sb has a valve • Dual dopant cell, 1.5 cc/each • Te dopant source • Interlock system in use

Table 3.1. Comparison of Intevac Gen II module and Veeco GENxplor

3.1.5 Reflection High Energy Electron Diffraction (RHEED)

Each growth chamber contains a reflection high energy electron diffraction (RHEED) unit to monitor the surface quality during the growth and determine the growth rates [21, 22]. A RHEED unit consists of an electron gun and a phosphorous screen as shown in the Figure 3.3 [23]. In the Gen II, electrons of energy 9.5 keV are used and in the GENxplor, electron energy of 14 keV are used for RHEED. The electron beam is directed at the wafer surface with a small grazing angle of 1 – 3°, which minimizes the penetration depth of electrons into the material. The electrons are diffracted from the substrate onto the phosphorus screen, where the pattern is recorded and analyzed with a charge-coupled device (CCD) camera and KSA 4000 software. Because of the small incident angle of the electron beam, diffraction pattern is only due to the first few monolayers, which makes RHEED a very surface sensitive technique.

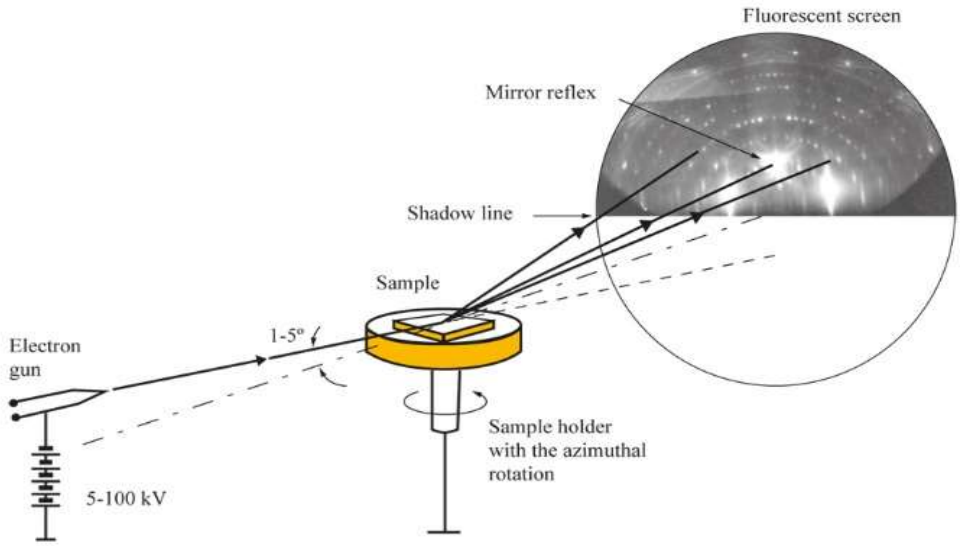

Figure 3.3. Schematic diagram of reflection high energy diffraction set-up (RHEED) [23].

During a 2D film growth, different RHEED features can be observed including Kikuchi lines, Laue circles and streak lines [24]. When the topography changes from a smooth to a rough surface, the RHEED pattern changes from (a) intense, short and well defined streaks to (b) long, diffuse and spotty and finally (c) to a fully spotty pattern [25]. These features in RHEED are of great advantage for in-situ monitoring of changes in the topography of surfaces.

When high-energy electrons are incident on the sample surface, they are diffracted because the distance between the atoms in the lattice is comparable to the incident wavelength of the high-energy electrons. The Laue equation sets the conditions for the incident wave to be strongly diffracted by the crystal. If $\boldsymbol{k_0}$ and $\boldsymbol{k}$ are the wavevectors for the incident and diffracted beams, respectively, the Laue condition (Figure 3.4) is;

$$\boldsymbol{k} - \boldsymbol{k_0} = \boldsymbol{G} \tag{3.1}$$

where $\boldsymbol{G}$ is any reciprocal lattice vector.

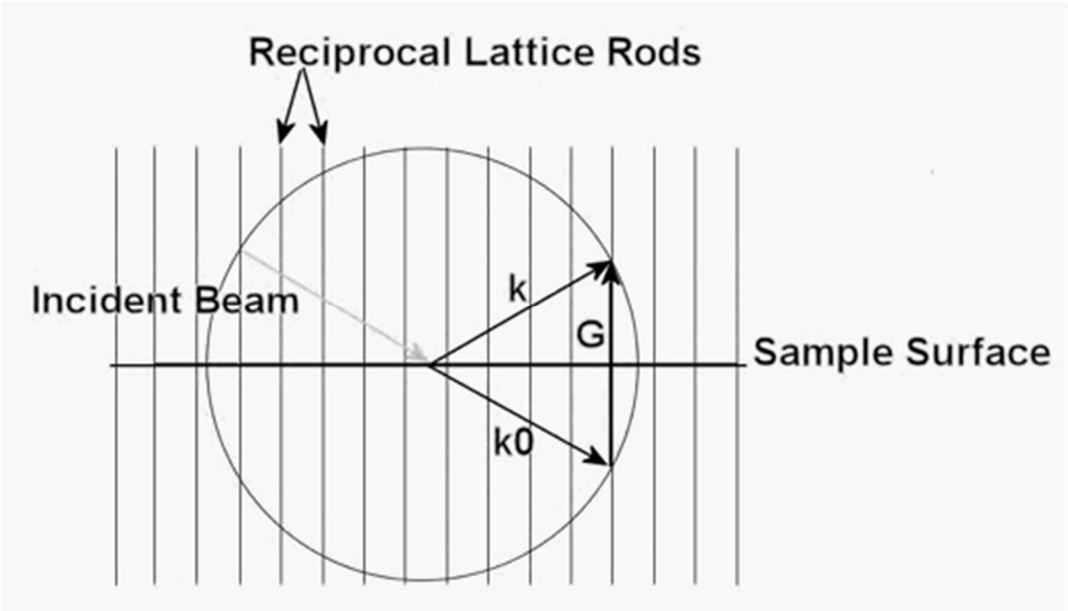

Figure 3.4. Construction of the Ewald's sphere at the sample surface. A cross-sectional view of a single row of reciprocal lattice rods is shown [26].

We construct Ewald's sphere in reciprocal space [27] to visually determine when the Laue condition is satisfied. Since the high-energy electrons only penetrate a few monolayers into the sample, we consider the crystal to be a 2D lattice. The reciprocal lattice of a 2D crystal is a set of infinite rods extending perpendicular to the lattice surface. Because elastic scattering is assumed, $\boldsymbol{k_0}$ and $\boldsymbol{k}$ have the same magnitude. The vector $\boldsymbol{k_0}$ is placed such that its head is on a reciprocal lattice point. The Ewald's sphere is centered at the tail of $\boldsymbol{k_0}$ and has a radius equal to the wavevector magnitude. The Laue condition is satisfied for $\boldsymbol{k}$ vectors drawn from the center of the sphere to points where the rods of the reciprocal lattice intersect the sphere.

When high-energy electrons are diffracted from a slightly disordered 2D lattice, streaks are observed in the RHEED pattern due to broadening of the reciprocal lattice rods. The number and intensity of the streaks is determined by the reconstruction of the atoms on the surface. Surface reconstruction occurs when at least one bond per atom is unsatisfied, creating unstable dangling bonds with unpaired electrons [28]. This instability causes the surface atoms to seek new coordinates that minimize the free energy of the surface. The periodicity of the surface reconstruction depends on how the atoms seek new coordinates. For an example, while growing GaSb on a GaSb (111)A surface, with Sb_2 rich conditions and at a substrate temperature of ~428 °C, a 2×6 RHEED pattern appears as shown in Figure 3.5. The strong intense lines are due to diffraction from the first few layers of bulk atoms which have a 1×1 unit cell. The weak intensity lines are due to the $2\sqrt{3}\times2\sqrt{3}$ unit cell created by the reconstructed surface atoms [29].

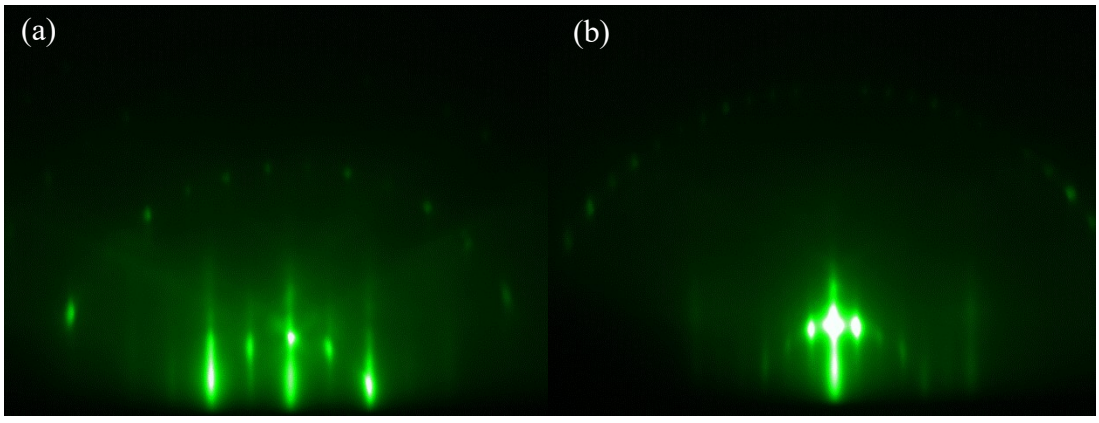

Figure 3.5. RHEED pattern of reconstructed surface while growing GaSb on GaSb 111)A surface at a substrate temperature of ~428 °C with Sb rich conditions. (a). 2× pattern created when the electron beam is incident along [-110] direction. (b) 6× pattern when the electron beam is incident along [-1-12] direction.

RHEED intensity oscillations are used as a direct measure of the growth rates. For example, consider a growth of GaAs epilayer on a GaAs substrate. When GaAs starts growing on a smooth GaAs surface, the intensity of the RHEED pattern, especially the specular reflection, starts to oscillate. The oscillation frequency corresponds to the monolayer growth rate. A single monolayer (ML) corresponds to a thickness of one complete layer of Ga atoms and one complete layer of As atoms. We can explain the oscillations using a layer by layer growth mode as illustrated in Figure 3.6. Initially when a layer starts growing, the surface is smooth and the specular spot is bright. However, as the layer nucleates, islands form on the surface, and the intensity of the specular spot drops. As the layer completes, the islands coalesce into a flat layer, and the specular spot becomes bright again. Typical RHEED intensity oscillations during GaAs growth on a GaAs substrate are shown in Figure 3.7 [30].

A smooth starting surface give rise to more oscillations in one shutter opening. In our system, Ga (as GaAs) and Al (as AlAs) are calibrated on GaAs (100) substrates at a substrate temperature ~ 580 °C. In (as InSb) is also calibrated on GaAs (001) substrates. Prior to In calibration, a ~1 μm thick buffer layer of InSb is grown to obtain a relaxed and smooth InSb surface. An InSb buffer layer is grown at 380 °C and the substrate temperature is lowered by ~25 °C below the pseudo (1×3) to c(4×4) transition temperature.

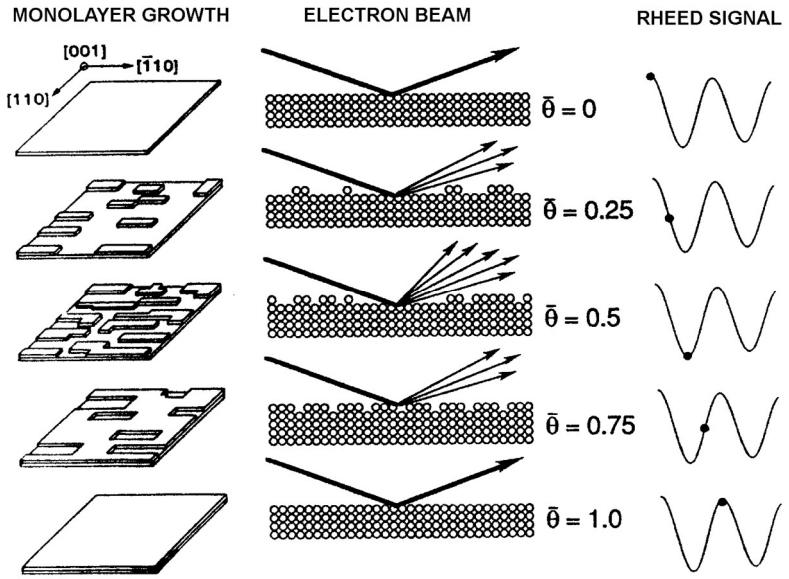

Figure 3.6. Explanation of specular beam oscillations with the monolayer growth [30].

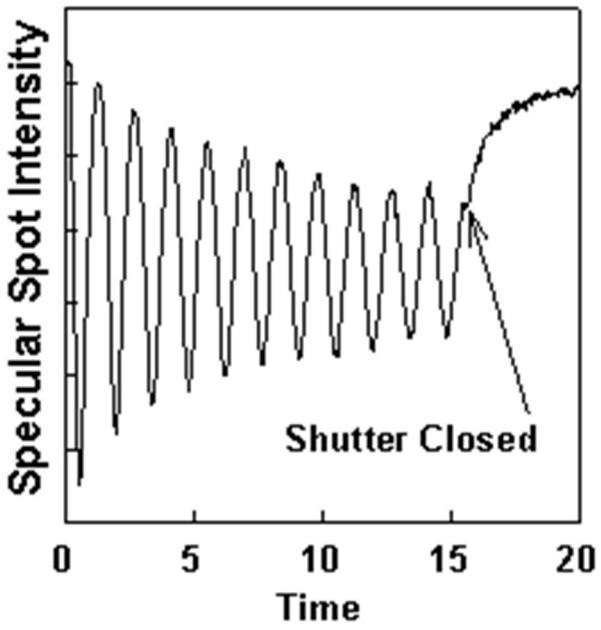

Figure 3.7. Example of intensity oscillation of the specular beam spot during GaAs growth on a GaAs substrate [30].

3.2 Scanning Electron Microscopy (SEM)

Scanning electron microscopy (SEM) is one of the most widely used nondestructive imaging technique. It uses a focused high-energy electron beam that interacts with the specimen surface to generate a variety of signals. Depending on the type of interaction, we can obtain information on the surface topography, composition, crystal orientation, strain and conductivity. We used field emission scanning electron microscopy (FESEM) to produce clearer and less electrostatically distorted images with a special resolution down to 1.5 nm; three to six times better than conventional SEM. FESEM also provides topographical and elemental information at magnifications of 10× to 300,000× with virtually unlimited depth of field [31]. In this dissertation, we used FESEM mainly to study the topography of the Sb and GaSb surfaces. A brief discussion on the FESEM/SEM subsystems and their functions are given below [32-35].

3.2.1 Subsystems of SEM and their Functions

There are two major components of the FESEM; the electron column and the control console. The control console consists of a cathode ray tube (CRT) viewing screen and controls for the electron beam. The base of the column is occupied by vacuum pumps that produce a vacuum in the range 10^{-4} – 10^{-13} Torr depending on the electron source used in the machine. Figure 3.8 shows a schematic of the electron column.

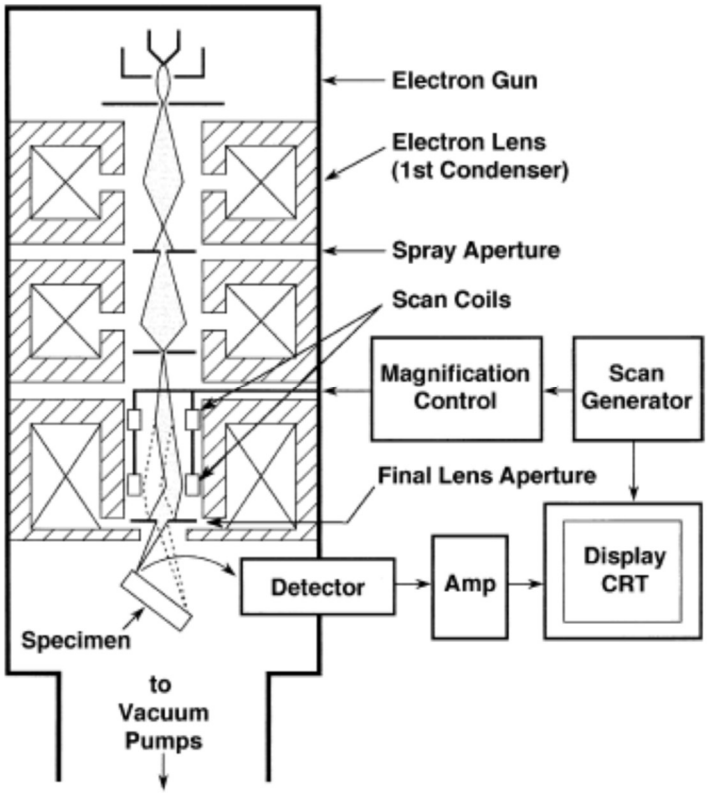

Figure 3. 8. Schematic of the electron column in SEM/FESEM, which includes an electron gun, electron lenses, a deflection system and a detector [32].

(a) Electron Gun: An electron beam is generated by two available mechanisms: thermionic emission or field emission (FE). Thermionic emission is produced using either a Tungsten filament (W) or a Lanthanum hexaboride filament (LaB_6). The process for field emission can be thermally assisted field emission (Schottky field emission, SE) or cold cathode field emission (CCFE). The electrons generated in either method are then accelerated towards the anode connected to ground potential (0V). In the field emission gun, the voltage between the tip and the first anode determines the field strength available to extract electrons; this is typically 3-5 kV to produce 10 μA of emission. The

voltage between the tip and the second grounded anode determines the accelerating voltage of the gun; this is typically in the range 0.1 – 30 keV.

(b) Condenser lenses: Usually one to three electromagnetic lenses are used to converge the beam in SEM. These lenses are capable of demagnifying an initial beam size of ~ 50 - 100 μm down to a ~10 nm (or less) spot size on the specimen by adjusting the current through a set of coils that change the magnetic field accordingly.

(c) Apertures: The apertures limit the convergence angle of the beam to control the aberration of the final lens.

(d) Scanning system: The function of the scanning system is to deflect the beam across the sample in a grid type scanning pattern.

(e) Objective lens (Final): This lens focuses the electron probe onto the specimen surface and contributes additional demagnification.

(f) Detector: When the electron beam interacts with the specimen, a variety of signals are generated. The electronics of the detector system convert the signals to point by point intensity changes on the viewing screen to produce an image. Secondary electrons (SE) and backscattered electrons (BSE) are the most commonly used signals to produce SEM images and the standard Everhart-Thornley (E-T) detector is used to detect both types of signals.

3.2.2 Electron-Specimen Interaction

When the high-energy electrons collide with the specimen, the electrons are scattered by atoms of the specimen. This results in a change of direction for the electrons that travel beyond the specimen surface. The interactions between the electrons and the specimen atoms occur within a certain volume under the specimen surface as shown in Figure 3.9. As a result of the interactions, secondary electrons (SE), backscattered electrons (BSE) and characteristic X-rays are generated from different zones. SE and BSE are used to produce an image whereas characteristic X-rays are used to identify elements in the specimen.

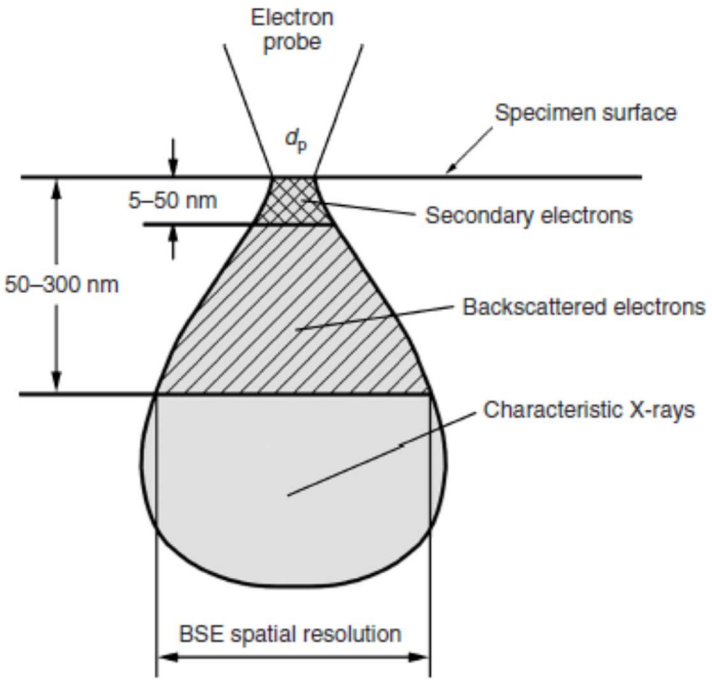

Figure 3.9. The zone of interaction for electrons and specimen atoms under the specimen surface [34].

3.2.3 Specification of the SEM Used in the Dissertation

We used a Zeiss Neon 40 EsB high-resolution SEM to study the topography of the samples discussed in the dissertation. It has the imaging and analytical capabilities of a high resolution FESEM with proven GEMINI technology that uses a novel electron optical design. The electron source is a Schottky emitter with an accelerating voltage of 0.1-30 kV which achieves a magnification of 20× to 900,000× with a resolution down to 1.1 nm. The microscope has the capability to perform energy dispersive X-ray spectroscopy (EDS) analysis, and produce an image using the backscattered electron detector (EBSD) and inlens secondary electron detector (inlens SE) [36]. Also, it has a focused ion beam (FIB) milling unit with a 5 gas injection system for etching and deposition [37]. When analyzing the topography of the samples, we used the EBSD to take plan view images whereas to measure the cross-sections, the inlens SE detector was used.

3.3 Atomic Force Microscopy (AFM)

Atomic force microscopy (AFM) is a surface analysis technique that belongs to the scanning probe microscopy family, which is capable of demonstrating a resolution on the order of fractions of a nanometer. In AFM, information is collected by either "feeling" or "touching" the surface with a mechanical probe. Very precise scanning is enabled via minute but precise movements of the piezoelectric elements that are connected to the probe.

An AFM instrument uses a cantilever with a sharp tip attached to its end, to scan the specimen surface. When the tip is brought in proximity of a surface, the force between the atoms on the tip and the atoms on the surface lead to deflection of the cantilever according to Hooke's Law. Forces of interaction between the tip and the surface can be van der Waals forces, capillary forces, chemical bonding, electrostatic forces, etc. AFM has three major capabilities; force measurements, imaging and manipulation. These are summarized below [38].

(a) Force measurements: AFM is used to measure the forces between the probe and the sample surface as a function of their mutual separation.

(b) Imaging: The deflection of the probe according to the force it experiences is used to generate a 3D image.

(c) Manipulation of the surface: The force between the tip and the interacting surface can be used to change properties of the surface in a controlled fashion. Scanning probe lithography is an example of this capability.

3.3.1 Microscope Architecture

A schematic of an AFM is shown in Figure 3.10. It consists of a light source that is either a laser or a LED (a superluminescent diode, SLD, in our instrument) which provides columnized light onto the rear side of a sharp tip attached to the end of a cantilever. Incident light is deflected off the rear side of the cantilever and the signals are collected by a position sensitive sensor/diode (PSD). The tip position changes according to the changes on the surface structure, so the deflection or the amplitude signal from the position sensitive detector also changes. Then this signal is digitized,

recorded and fed back into the digital feedback system which tries to maintain a user defined set point. This user defined set point can be either deflection or the amplitude from the PSD, depending on the mode employed (AC or contact mode). The Z stage responds to the feedback and moves up or down to keep the signal at the the user defined set point. The Z distance motion is recorded per X, Y point and thus a 3D image is produced.

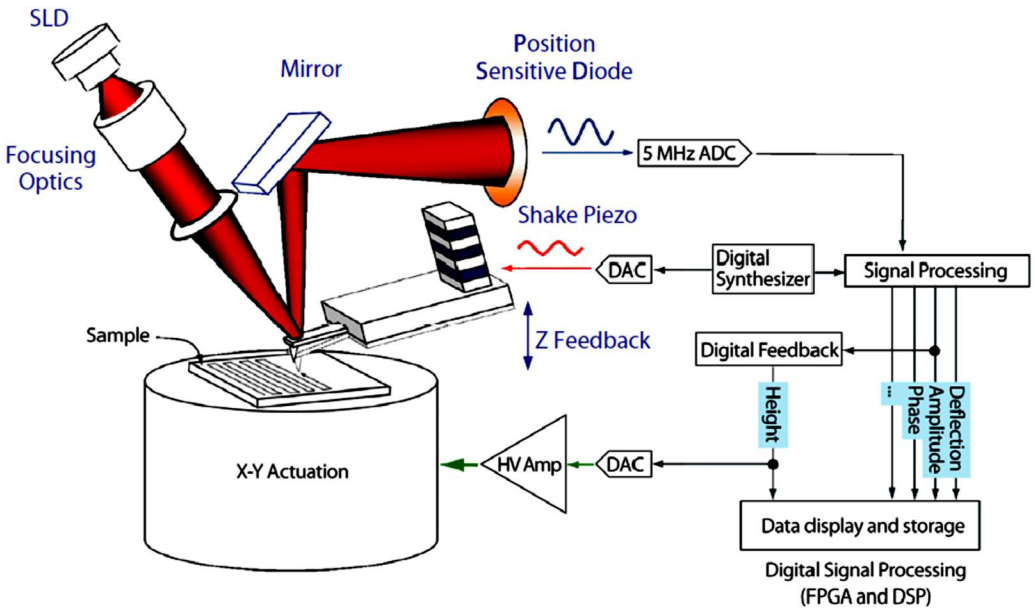

Figure 3.10. Schematic of Atomic Force Microscope MFP-3D system [39].

3.3.2 Imaging Modes

There are three major imaging modes: contact mode, non-contact mode and AC mode. These are summarized below. The interaction force depends on the distance between the tip and the surface, and the scanning modes are categorized accordingly. Figure 3.11 shows the operation regimes as a function of the tip to sample distance.

(a) Contact mode: The tip is in full contact (also called hard contact) with the sample surface so the interaction force between the tip and the surface atoms is repulsive. During the scan, the tip is held static. This mode is good for hard surfaces, but it may cause damage to surfaces made of soft matter.

(b) Non-contact mode: The tip is close to the surface but not touching and the interaction force is the attractive van der Waals force. In this mode, the tip is made to oscillate at or slightly above its resonant frequency with a small oscillation amplitude (typically < 10 nm). The tip to sample distance is held constant during the scan. This method may cause little or no damage to the sample surface.

(c) AC scan mode: This is also called the intermittent contact mode or the tapping mode. Tapping mode is an advanced method for imaging which can achieve high resolution without leading to a destructive force of interaction with the surface. The tip is made to oscillate at a slightly off-resonance frequency but it has a higher oscillation amplitude (typically ~ 100 nm) than during non-contact mode. Because of the high oscillation amplitude, the interaction force varies between attractive and repulsive regimes.

In this dissertation, we used an Asylum Research MFP-3D AFM system to study the surface morphology of Sb and GaSb surfaces. It has an infrared superluminescent diode (SLD) as the focused light source with a wavelength of 860 nm and a focused spot size of 10-50 μm that is incident on the rear side of the cantilever. The SLD directs the light at an angle of 22° to the cantilever which helps to eliminate optical interference from stray reflections off the sample that could convolute the PSD

signal [39, 40]. The cantilever used for scanning is made of silicon (Asylum Research AC160TS-R3) and has a resonance frequency of 300 (200-400) kHz and a spring constant of ~26 (11-54) N/m. The radius of the tip is 9±2 nm. The top of the cantilever is coated with Al to improve the reflectance of the laser light.

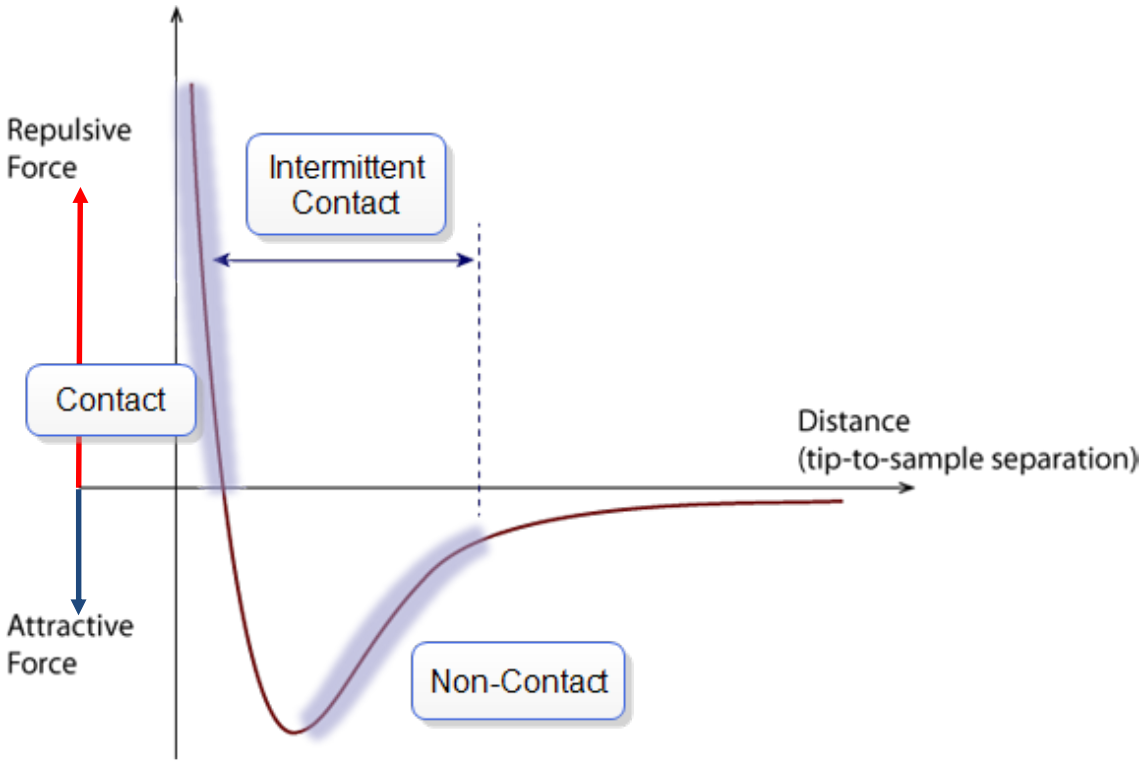

Figure 3.11. The force of interaction between the sample and the surface as a function of the tip to sample distance [41].

Chapter 4: Epitaxial Growth and Structural and Characterization of Sb Quantum Wells

4.0 Introduction

Sb has a rhombohedral crystalline structure with ABC stacking along the (111) direction (Figure 4.1) [5]. To grow quantum wells with high quality (fewer defects), we need to choose the barrier material and the substrates carefully. For our study, we used GaSb (111) substrates for several reasons:

a) Both GaSb and Sb have a hexagonal (111) surface net; therefore, the growth of Sb is feasible on GaSb (111).

b) Zincblende GaSb has a lattice constant of 4.310 Å for the hexagonal surface. Sb has a lattice constant of 4.308 Å for the hexagonal surface. Therefore, the lattice mismatch between these two materials in the <111> directions is less than 0.1%. Hence, we can grow Sb with very low defect density.

It is very important to have fewer defects because unintentional doping by defects may contribute much more to the conduction than the electrons TI states. Because of our choice of barrier material, we expect high quality Sb layers.

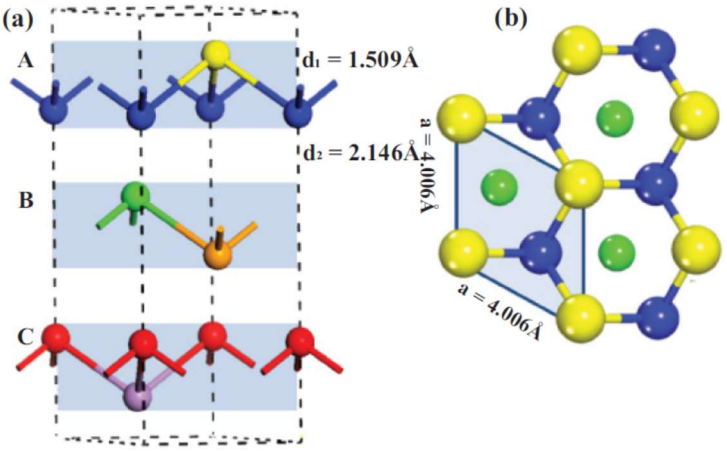

Figure 4.1. Unit cell of Sb with ABC stacking [5].

4.1 Experimental Procedures

4.1.1 Substrate Preparation

We used GaSb (111) wafers from two different manufacturers, Wafer Tech and Galaxy. These were 2" in diameter and n type doped with Tellurium (Te). The Wafer Tech was polished only on side A and had a thickness of 1mm. The Galaxy wafers were 500 µm thick and double side polished, but with side A is smoother than side B. The Wafer Tech substrates were trial grade whereas Galaxy substrates were epi-ready. For all Sb growths, we used surface A which is Ga terminated with a single dangling bond per atom. The wafer were cleaved into ~ 1×1 cm^2 pieces by scribing on the backside (side B) before cleaving and blew dry N_2 to clean the surface from dust. For the structures grown in Intevac Gen II, we degassed each 1×1 cm^2 substrate at 250 °C for 12 hours at the heated station prior to growth. We skipped this step prior to growth for the structures grown in the Veeco GENxplor after realizing that neither the oxide desorption nor the crystalline quality of the structures were not that benefitted by degassing the substrates. The native oxide layer was desorbed at a thermocouple

temperature of ~ 520 – 530 °C for a Wafer Tech substrate and ~ 560 – 575 ° C for a Galaxy substrate. The substrate was then annealed for ~ 10 minutes and 5 minutes at a temperature of 10 °C and 20 °C higher than the oxide desorption temperature, respectively.

4.1.2 Epitaxial growth and post growth characterization

We performed the growths in two different MBE systems, the Intevac Modular Gen II and a Veeco GENxplor. An EPI Sb cracker (1997) was used with a cracking zone temperature of 900 °C was used in Intevac Gen II whereas a 200cc Sb valved cracker (2013) with the same cracking zone temperature was used in the GENxplor. Beam fluxes were measured using an ion gauge that can be moved into the sample position. Substrate temperatures above 400 °C were measured using both an optical pyrometer and a thermocouple mounted behind the substrate holder, and were in very good agreement with each other. On the other hand, below 400 °C substrate temperatures were measured only using the thermocouple mounted behind the substrate holder. The growth was monitored *in situ* using reflection high energy electron diffraction (RHEED).

Scanning electron microscopy (SEM), field-emission scanning electron microscopy (FE-SEM), field-emission transmission electron microscopy (TEM) and atomic force microscopy (AFM) were employed for the structural characterization of the structures. During the growth of Sb, RHEED intensity oscillations were not observed. Hence the growth rate was determined from cross-sectional SEM measurements of thick Sb films with deposition times of 30 and 60 minutes. The

thickness of a representative ultra-thin Sb layer was determined by cross-sectional TEM measurements.

4.2 Epitaxial Growth of Sb

4.2.1 Epitaxial growth procedure

A series of Sb/GaSb quantum well (QW) structures were grown on n-type GaSb (111)A substrates with the layer sequence of the samples is shown in Figure 4.2. For the carriers in the Sb QW, the GaSb buffer layer and the GaSb cap layer are expected to act as energy barriers. Following the growth procedure, we reported in [42] first a 0.5 μm-thick GaSb buffer layer was grown on the GaSb (111)A substrate at a temperature ~65 - 100 °C below the oxide desorption temperature (560 °C). The GaSb growth rate calibrated using RHEED oscillations was 0.45 monolayers (ML) per second with an Sb_2:Ga beam flux ratio of ~4.1. A 2×6 RHEED pattern was maintained during the entire growth of the GaSb buffer layer as shown in Figure 4.3(a). After growing the GaSb homo epitaxial layer, the substrate was annealed for ~5 minutes at a temperature of ~10 °C higher than the growth temperature under an Sb flux. The substrate temperature was lowered under an Sb flux with the RHEED pattern transitions from 2×6 to 5×1. The Sb shutter was closed at a substrate temperature of ~350 °C (~65 °C below this transition). Then the substrate temperature was reduced further by ~10-20 °C and annealed at this temperature with no Sb flux until the RHEED pattern changed from 5×1 to 2×6. In order to obtain a smooth GaSb surface, slow out-diffusion of excess Sb on the surface is necessary.

The substrate temperature was further lowered by ~220 °C without an Sb flux. The RHEED pattern remained 2×6 during the additional temperature reduction and just before the Sb QW growth [Figure 4.3(b)]. The Sb shutter was reopened at a substrate temperature of ~160 °C to grow an epitaxial thin Sb layer at this fixed temperature with a constant flux. A well-defined streaky 1x1 RHEED pattern was observed after the Sb growth [Figure 4.3(c)]. In order to obtain a smooth 2D crystal growth of Sb on a GaSb(111)A substrate the surface reconstruction of the GaSb surface needed to remain 2x6 prior to the Sb QW growth. Attempts to grow Sb on a 5×1 reconstructed surface on GaSb (111)A gave rise to 1D wires instead of a 2D epitaxial layer, as indicated by a spotty RHEED pattern. After depositing the Sb layer, a GaSb cap layer was grown using migration enhanced epitaxy (MEE) technique to prevent the Sb surface from getting oxidized. For the GaSb cap layer, the shutters were cycled multiple times through a three-step sequence where only the Ga shutter is open for 1ML, both shutters are closed for 1 second and Sb shutter is opened for 1ML.

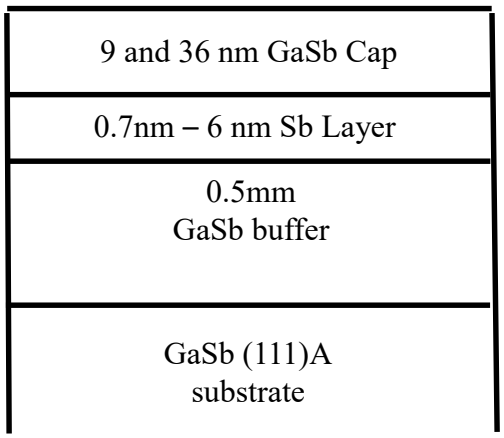

Figure 4.2. Layer sequence of the Sb QW structures

After growing a ~9 nm GaSb cap, a 1×1 RHEED pattern was observed [Figure 4.3(d)] whereas for a ~36 nm cap, a weak 1×2 RHEED pattern was observed [Figure 4.3(e)]. Uncapped QW structures were also grown for the purpose of investigating the surface morphology of the Sb layer.

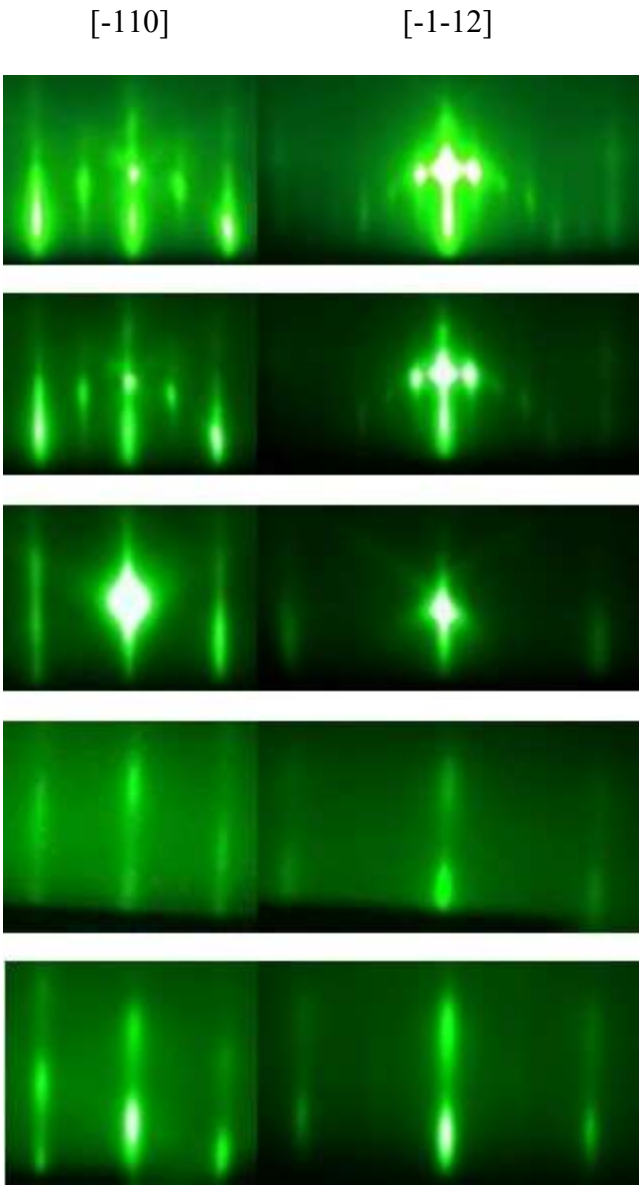

Figure 4.3. RHEED pattern along the [-110] and [-1-12] directions for the GaSb(111)A surface (a) at a 428 °C, after the GaSb buffer layer growth under an Sb flux, (b) 185 °C, just before Sb QW growth, (c) 185 °C, after Sb QW growth, (d) 185 °C, after a 9 nm thick GaSb cap layer, and (e) 185 °C, after a 36 nm thick GaSb cap layer growth.

4.2.2 Growth rate calibration of Sb

Figures 4.4(a) and 4.4(b) show the cross-sectional SEM images of uncapped thick Sb epilayers with deposition times of 30 minutes and 60 minutes. For a fixed Sb flux (5.7E-7), a deposition time of 30 minutes at a substrate temperature of 145 °C resulted in an Sb layer that is almost half as thick (336 nm) as the one deposited for 60 minutes (658 nm) at 160 °C. Using these data, we calculated the growth rate of Sb at 145 °C and 160 °C was calculated to be 0.19 nm/s. Further, we found a similar growth rate for temperatures of 180 °C and 170 °C, indicating that Sb has a well-controlled growth rate with the newly developed growth procedure described above. In the growth of Sb on GaAs (111)A substrates Sb nucleates below 330 °C, but on GaSb(111)A substrates Sb nucleates below 230 °C.

A high resolution cross-sectional TEM image of an ultrathin Sb QW grown at 180 °C is shown in Figure 4.5. As expected from growth rate calibrations, Sb deposition time of 20 s resulted in a thickness of 4.1 – 3.4 nm for which the calculated average thickness was 3.8 nm, indicating good control over the growth rate even for ultrathin layers. Within the experimental resolution, both GaSb and Sb have expected crystalline structures and the expected interatomic distances (3.52 Å for GaSb and 3.76 Å for Sb) along the growth direction [111].

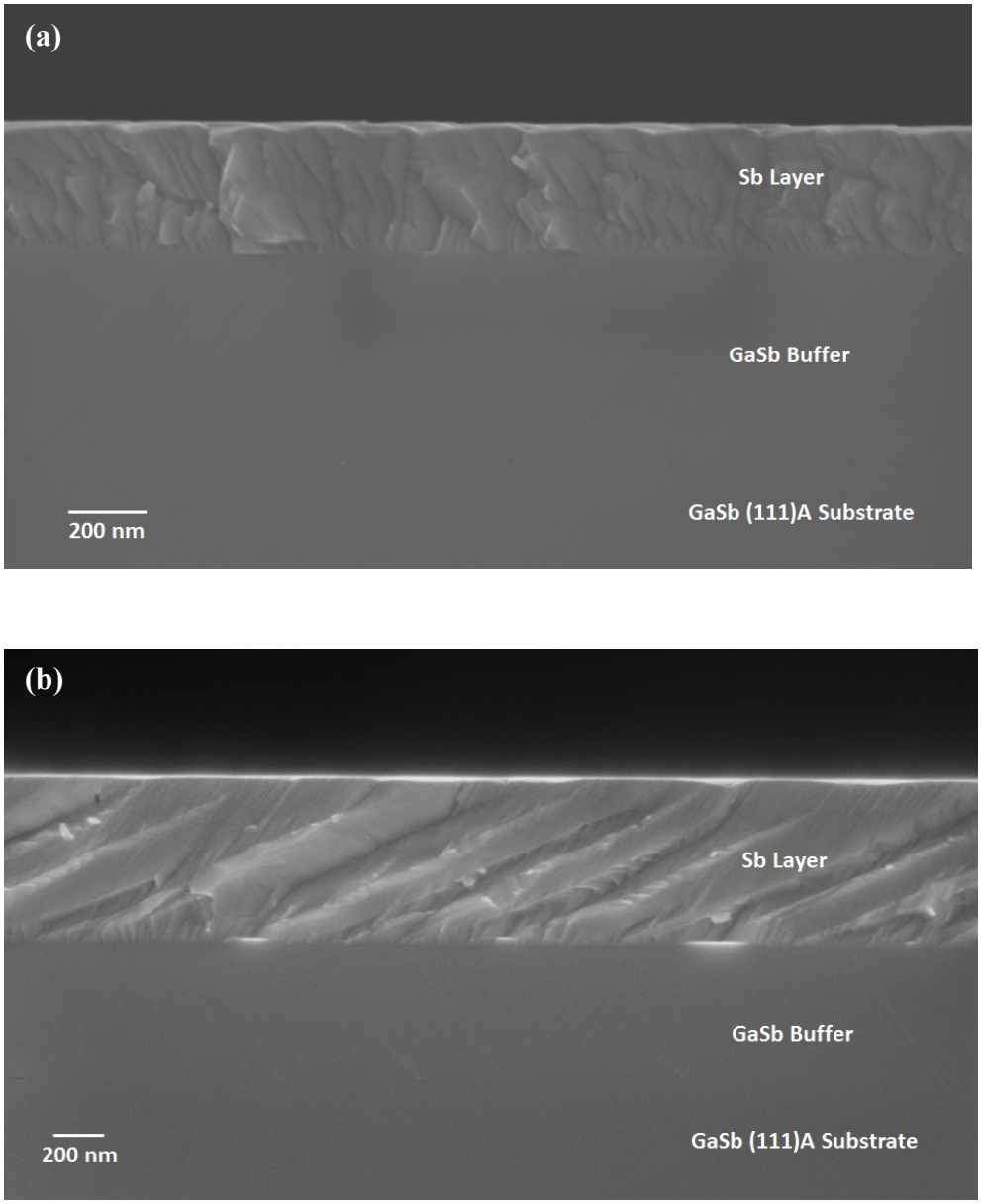

Figure 4.4. Cross-sectional SEM images of uncapped thick Sb layers grown at (a) 145 °C with a deposition time of 30 minutes resulting in a thickness of 336 nm and (b) 160 °C with a deposition time of 60 minutes resulting in a thickness of 658 nm. Roughness can be seen in the images which is due to cleaving.

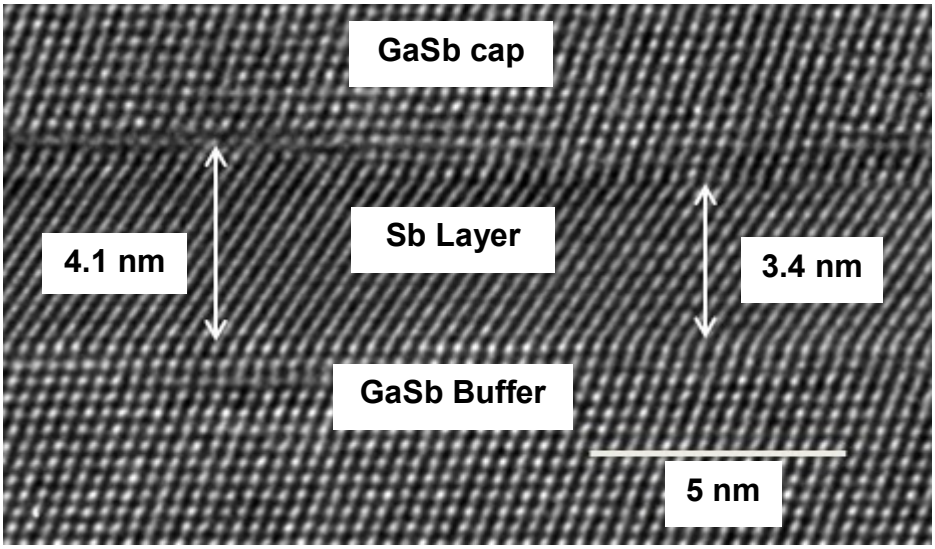

Figure 4.5. High resolution cross-sectional TEM image of an Sb QW with an average layer thickness of 3.8 nm.

4.3. AFM, FESEM and TEM Study of Thin Film Sb Structures

4.3.1 Structural properties and surface morphology

Figure 4.6 (a), (b) and (c) show AFM images of three different uncapped Sb layers with thickness 2.9 nm, 3.8 nm and 2.2 nm respectively. These three structures were grown on Wafer Tech substrates at a substrate temperature of 185 °C in the Gen II. Sb starts nucleating in triangular islands that eventually coalesce. Thus, we see incomplete surface layers as bright triangular shapes and uncovered portions of complete layers as dark triangular shapes aligned in the opposite direction to that of the bright triangles. Atomic steps of the top most layers are clearly visible in Figure 4.6 (c) This surface is not completely covered by Sb as observed from large area AFM images, though we have not shown them here. Root mean square roughness (rms) of the 2.9 nm and 3.8 nm thick Sb epilayer is 0.45 nm, which is much less than the thickness than the layer thickness. Also, we can see that the number of dark triangular areas have

decreased with increasing thickness indicating that we were able to grow ultra-thin Sb layers with a good uniformity and a high surface coverage. Black dots and bright white dots present in these images are dust particles or artifacts, not real features of the Sb structure.

Figure 4.6 (d) shows an AFM image of an uncapped 2.8 nm Sb layers grown on a wafer bought from Galaxy at a substrate temperature of 200 °C in the GENxplor. There is complete surface coverage of Sb but the roughness is ~ 1.25 nm which is high. The dark line in this figure is a defect propagating through the Sb layer and the height profile across the defect shows a sudden dip (profile 1 and 3 in Figure 4.6 (e)). The defect free area has no such feature as shown in line profile 2 in Figure 4.6 (e). The appearance of defects is surprising because Sb is lattice matched to GaSb (111)A substrates. A high density of defects was observed for Sb grown on GaAs(111)A substrates due to the 7.8% lattice mismatch [42].

Figure 4.7 (a) shows plan view FESEM images of the same 3.8 nm thick uncapped Sb sample analyzed using AFM in Figure 4.6. Like in AFM images, triangular features are observed in Figure 4.7 (a) and (b), which are electron backscattering diffraction (EBSD) images of the surface. The appearance of the triangular shape is due to the three-fold symmetry of the hexagonal arrangement of atoms on the Sb surface. In addition to that there are four key features we in the images, haziness, continuous dark line contrast, closed loop dark line contrast, and dark point-like features.

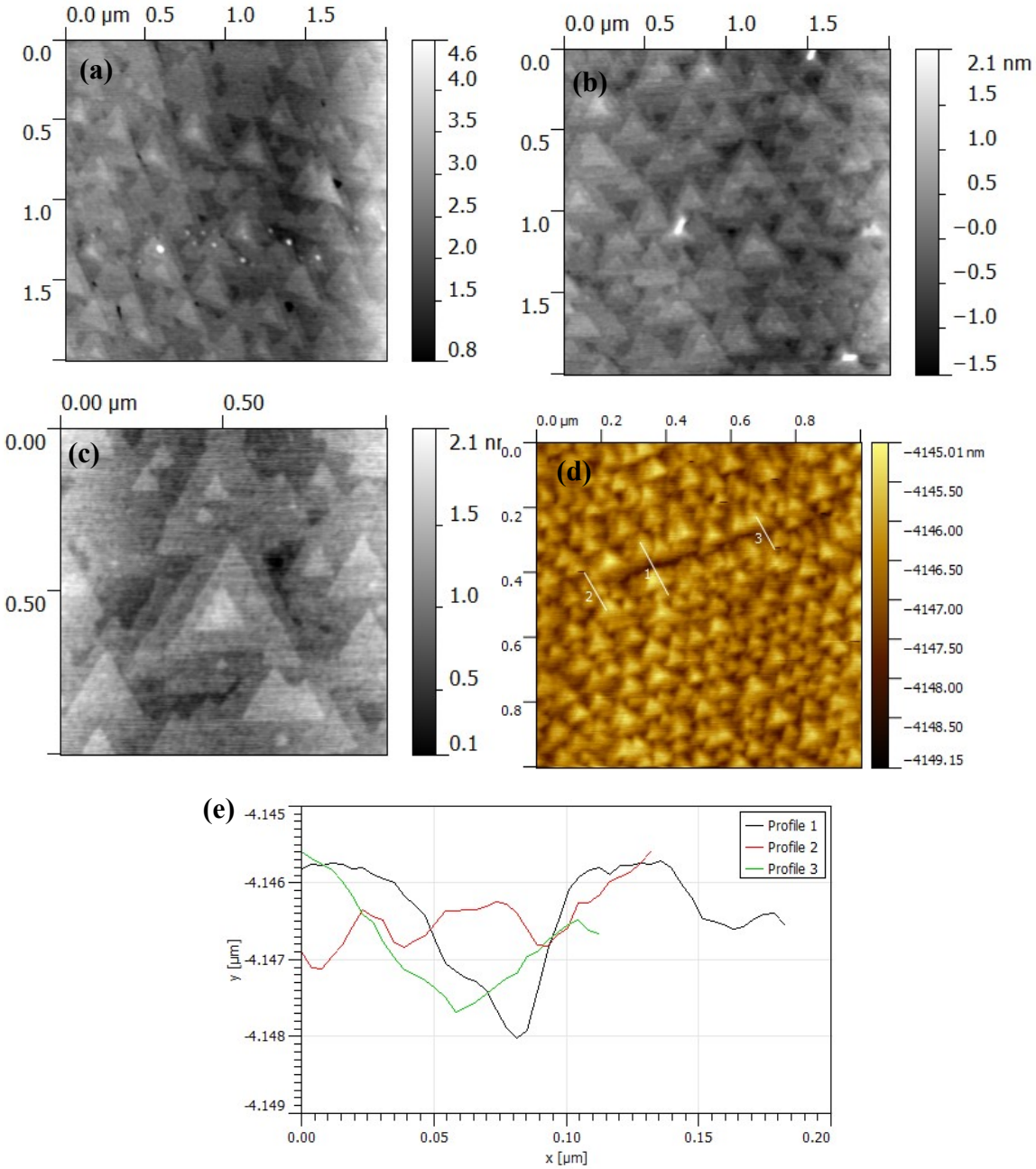

Figure 4.6. (a) and (b) are AFM images of (a) 2.9 nm and (b) 3.8 nm uncapped Sb layers. (c) 1×1 µm scanned area shows atomic steps in uncapped 2.2 nm Sb layer showing atomic steps. All three structures were grown in the Gen II at a substrate temperature of 185 °C. Black dots and bright white dots in these images are some dust particles, not the real features of the Sb structure. Thus, color scale ranges do not reflect the true surface smoothness. (d) 2.8 nm thick Sb QW with no cap grown on the wafers bought from Galaxy at a substrate temperature of 200 °C in the GENxplor. (e) Line profile showing the height variation across a defect and across a no defect area of the surface shown in (d).

(a)

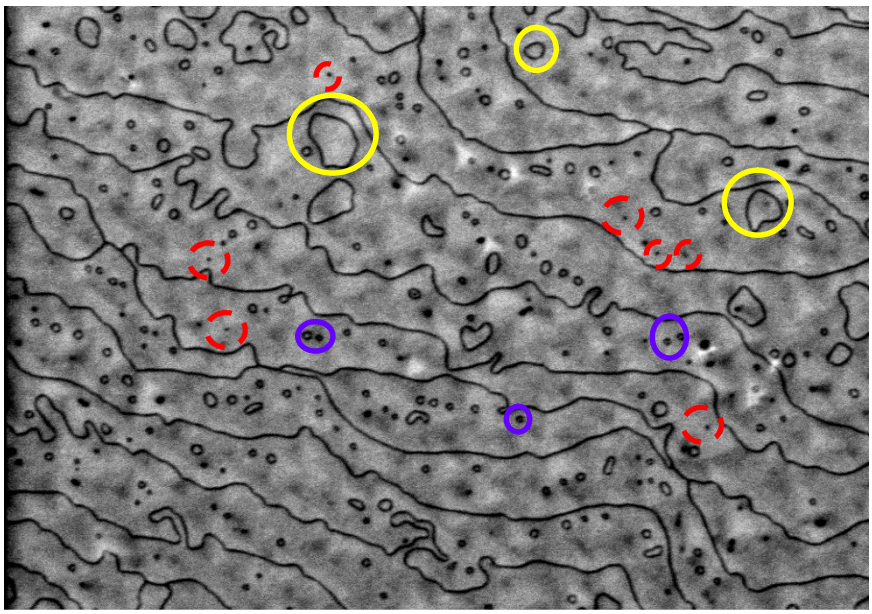

(b)

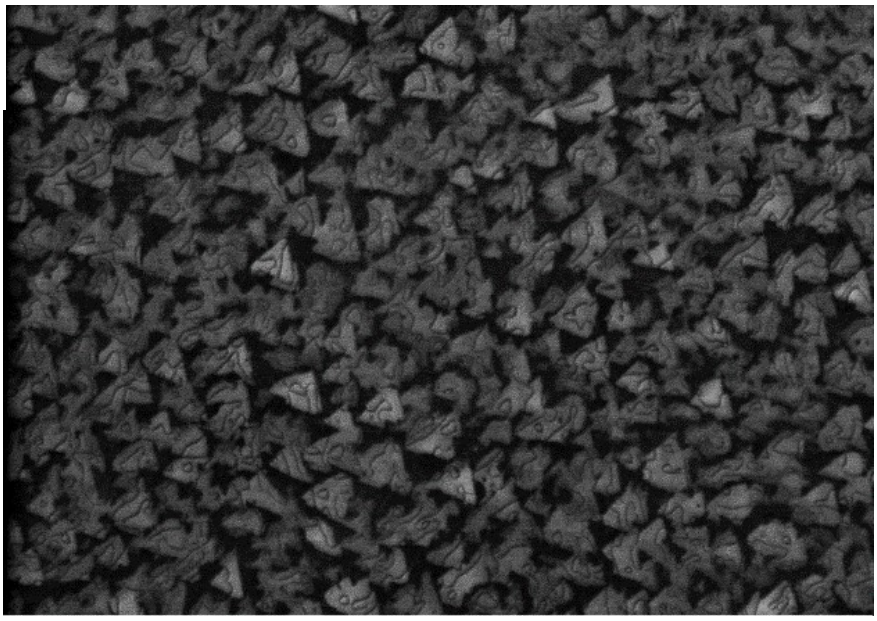

Figure 4.7. Plan view FESEM images of (a) 3.8 nm uncapped Sb structure which is has a full coverage of Sb layer and (b) 1.5 nm uncapped Sb structure which has an incomplete coverage of Sb.

The Sb surface oxidizes when exposed to atmosphere and thus we observe haziness, possibly caused by the (strain in the oxide layer) which is detected by the FESEM only when a high-energy electron beam (10 keV) is used. Due to the existence of the oxide layer, triangular features and steps that are observed in AFM image are washed away in the FESEM images.

In order to study the dark line contrast, we performed AFM and FESEM imaging of the same area of a chosen sample. Since we first observed this feature on the Sb structures grown on GaAs (111)A substrates [42], this comparison of Sb surface was done using Sb grown on GaAs(111)A substrates. Figure 4.8 (a) shows a plan view AFM image of 3.7 nm thick uncapped Sb grown on 0.5 μm thick GaSb epilayer on a GaAs (111)A substrate. Triangular Sb islands and Sb step edges are clearly visible in this image. We marked this specific area and the crystallographic direction using the tiny dark triangular feature shown in the yellow circle and imaged the same area using high energy backscattering electrons of 10 keV in FESEM (Figure 4.8 (b)). In Figure 4.8 (b), we can see the dark line contrasts on Sb triangular islands but these do not correlate with the Sb step edges observed in the AFM image. Further, the same area was scanned using a low energy electron beam in FESEM (Figure 4.8 (c)) and we observed only the Sb islands and the step edges but no dark line contrasts. This specific scanning mode in FESEM is sensitive only to the surface. Therefore, we concluded that dark line contrasts do not correlate to Sb step edges and these are not on the Sb surface. Figure 4.8 (d) is a high energy backscattering FESEM image of the same area but taken by tilting the sample at the Brag tilt. Under this condition, the dark line contrasts changed to bright

line contrasts which is an indication that these line contrasts are due to crystalline defect.

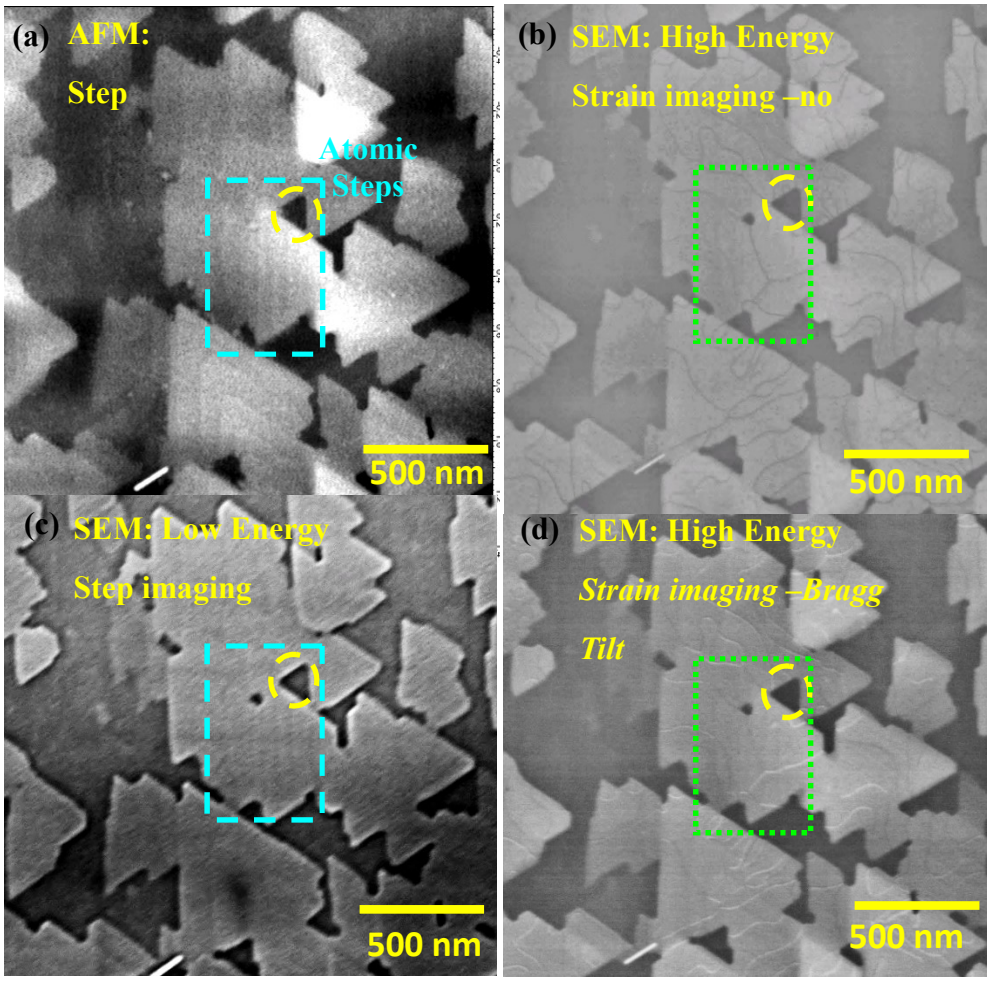

Figure 4.8. (a) Plan-view AFM image of Sb grown on GaAs substrate showing atomic steps. (b) Plan-view FESEM image of Sb grown on GaAs substrate imaged using high energy backscattered electrons, showing dark loop lines. (c) Plan-view FESEM image of (b) imaged using low energy electrons, shows no dark loop lines. (d) Plan-view FESEM image of the same area imaged using high energy backscattered electrons at Bragg tilt. Dark lines appear as bright lines, implying that this feature is due to crystal strain.

Then we compared the GaSb epilayer and the dark line contrasts using plan-view FESEM. For this part of the study we used Sb grown on both substrates, GaSb(111)A and GaAs(111)A, we obtained the same results which we discuss below.

Figure 4.9 (a) and (b) shows plan-view FESEM and AFM image of a GaSb epilayer grown on GaAs (111)A substrate. When we compare this image with Figure 4.9 (c), dark line contrasts appear to follow the step edges of the GaSb epilayer. This relation is very clear when we compare the GaSb epilayer grown on the GaSb (111)A wafers bought from Galaxy (Figure 4.9 d and e).

Figure 4.10 (a) shows large area plan-view FESEM image of a GaSb epilayer grown on GaSb (111)A substrate bought from Wafer Tech. When we compare this image with Figure 4.7 (a), dark line contrasts appear to follow the step edges of the GaSb epilayer. This is clearly observed when we compare the GaSb epilayer grown on the GaSb (111)A wafers bought from Galaxy (Figure 4.11.(b)) and the uncapped Sb grown on those wafers shown in the Figure 4.10 (b). GaSb epilayers grown on wafers bought from Galaxy had lots of atomic steps (Figure 4.14) compared to those bought from Wafer Tech (Figure 4.13) which allowed us to correlate the dark line contrasts with the GaSb step edges. Shape of the dark line contrasts appearing on figure 4.10 (b) is overlapping with the steps of the truncated triangular islands on GaSb epilayer observed in Figure 4.11 (b). Thus, we concluded that this feature is related to GaSb step edges.

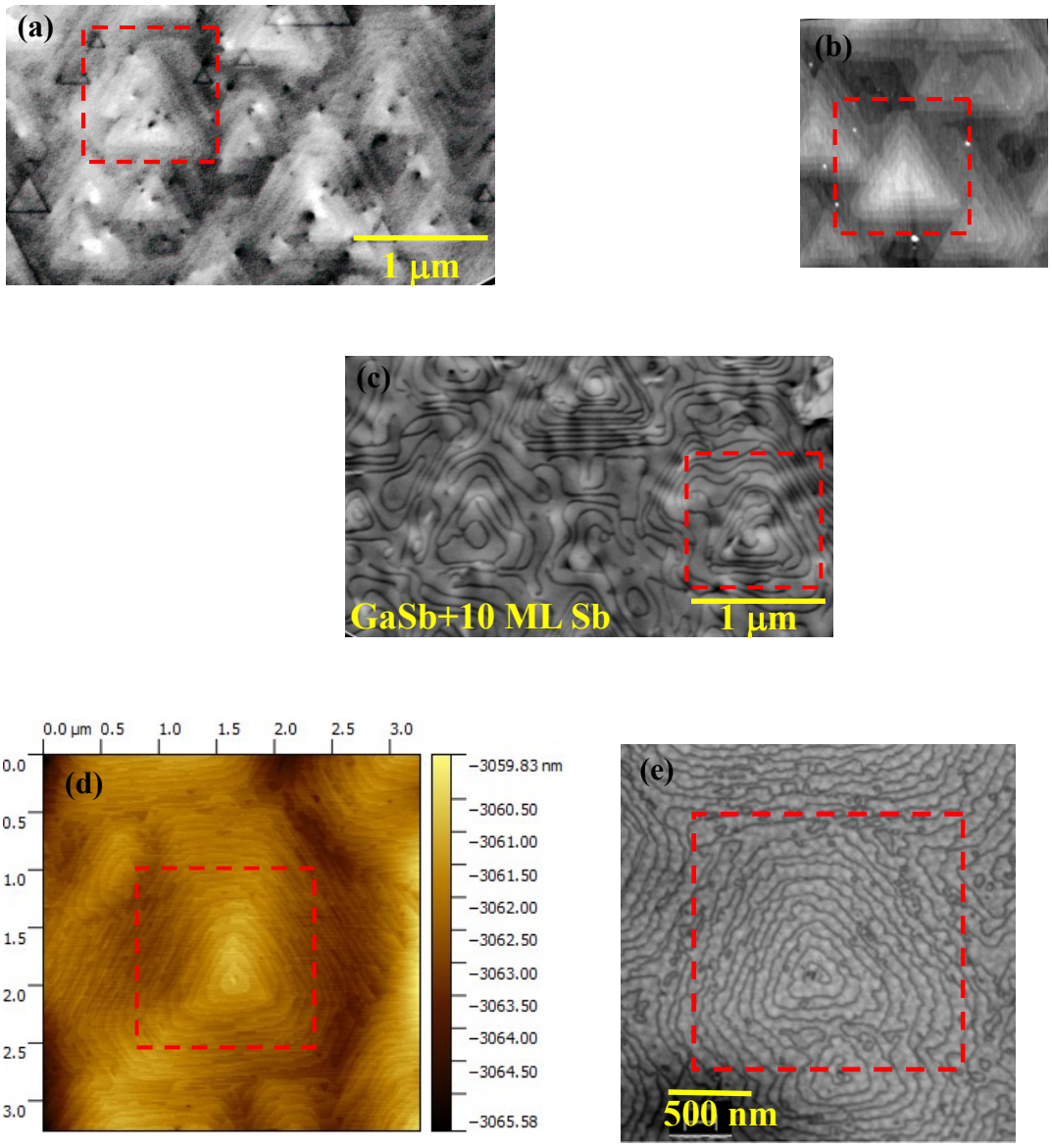

Figure 4.9. (a) Plan view FESEM image of 500 nm GaSb epilayer grown on GaAs (111)A substrate showing triangular shape islands. (b) Plan view AFM image of (a). (c) Large area plan view FESEM image of 3.8 nm thick Sb grown on GaSb epilayer as shown in (a). (d) Plan view AFM image of GaSb epilayer grown on GaSb (111)A substrate bought from Galaxy. (e) Plan view FESEM image of 3.8 nm Sb grown on an epilayer similar to the one shown in (d).

(a)

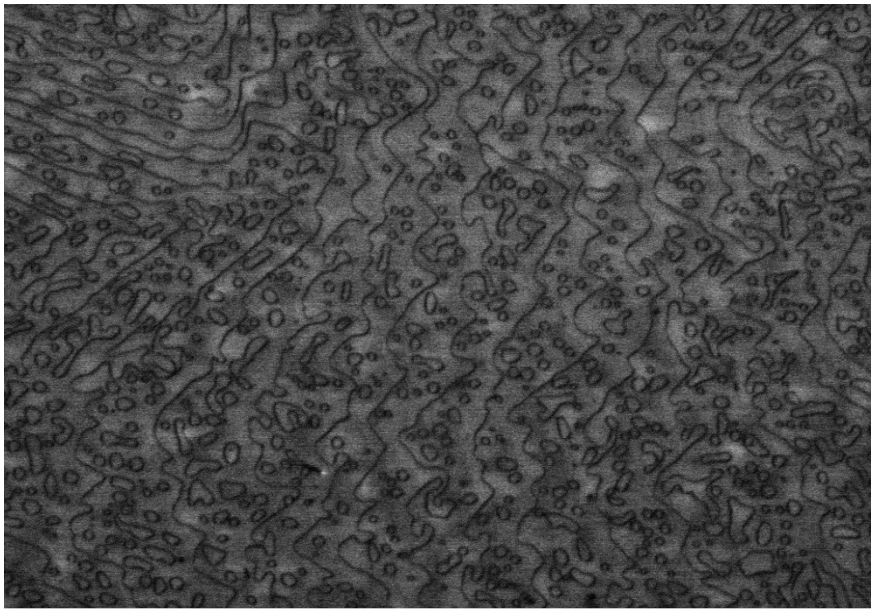

(b)

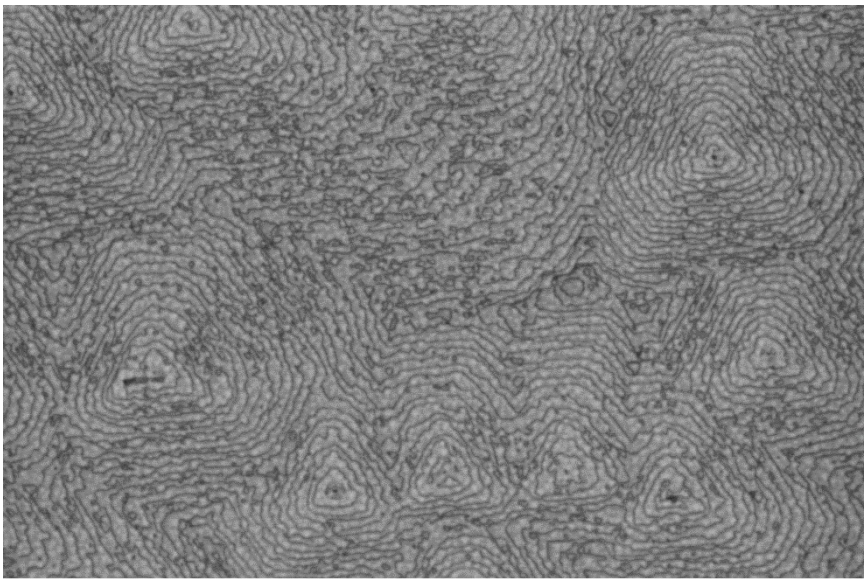

Figure 4.10. (a) Plan view image of uncapped Sb sample of 2.9 nm thick grown on GaSb (111)A substrate bought from Wafer Tech. (b) Plan view image of uncapped Sb sample of 2.9 nm thick grown on GaSb (111)A substrate bought from Galaxy.

(a)

(b)

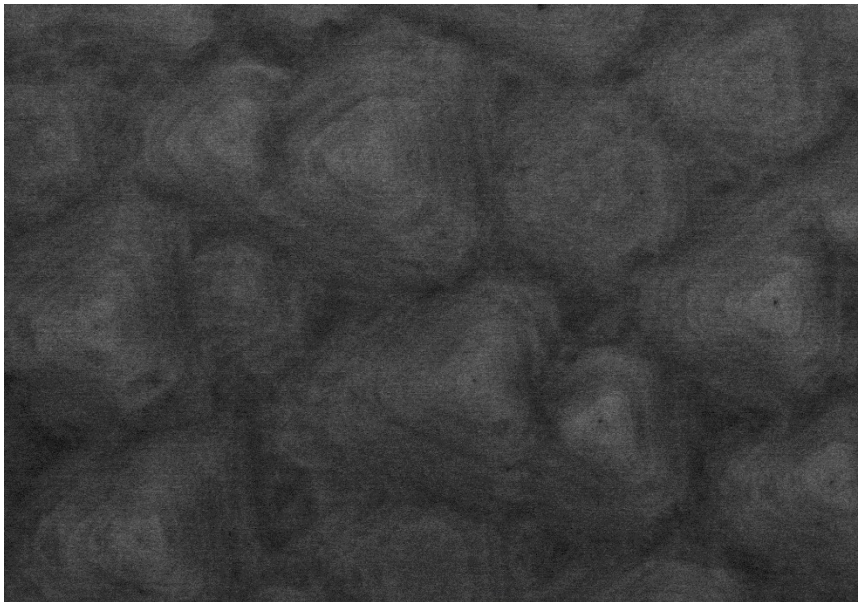

Figure 4.11. GaSb epilayer on (a) T544 Wafer Tech substrates (b) T726-Galaxy substrates.

We further studied the Sb layer and the GaSb/Sb interface at the step edges using cross-sectional TEM and found that the atomic arrangement of the GaSb/Sb interface at the step edges is different from the atomic arrangement of the GaSb/Sb interface on a flat GaSb surface (i.e. when there is no step) [43]. Also, this different atomic arrangement does not continue into the Sb layer, thus these bonds are strictly constrained only to the GaSb/Sb interface at the step edges. Therefore, this is a local strain which is created only at the GaSb step edges where Sb makes a strained bond with GaSb surface atom to preserve the Sb structure with no defects. High energy backscattering electrons in FESEM is detecting this strain as a dark-line contrast which is buried under the Sb layer. A ball and stick model as an example for the structure that could exist at the interface of GaSb/Sb step edges is shown in Figure 4.12. A schematically represented GaSb/Sb interface of Sb is shown in Figure 4.12 (a). It does not have an atomic step, so we will not see any dark line contrast if observed by FESEM. Figure 4.12 (b) shows a possible model of the structure where local strain is created at the step edge.

Continuous dark line contrasts appear when the GaSb steps are continuous and long range as shown in Figure 4.13 (a), a plan-view AFM image of GaSb epilayer grown on wafers bought from Wafer Tech. Additionally, the Sb layer should be complete to see continuous dark line contrasts unless we observe very short and broken dark line contrasts as shown in Figure 4.7 (b) which is a FESEM plan-view image of an incomplete Sb layer with a nominal thickness of 1.5 nm. Small closed dark loop line contrasts highlighted by yellow circles in Figure 4.7 (a) appear when Sb grows around

very small GaSb islands formed during the GaSb epilayer growth as shown in Figure 4.12 (a), highlighted by red circles.

Circular dark line contrasts with diameters in the range of 30 nm to 80 nm are shown in the Figure 4.6 (a) (examples of these shown in purple circles). They are due to the Sb growth inside the similar size pores found on the GaSb epilayers. Figure 4.12 (c), a plan-view AFM images of a GaSb epilayer shows the pores and Figure 4.12 (d) shows the height profile across these pores. Using the height profile, we found that these pores are very shallow with a height range of ~ 0.2 nm – 0.4 nm. When Sb fill these pores strain bonds are created with the GaSb walls which FESEM images as dark line contrasts. These pores have unstrained Sb bonds which we observe as white contrast in the middle of these loops in Figure 4.7 (a).

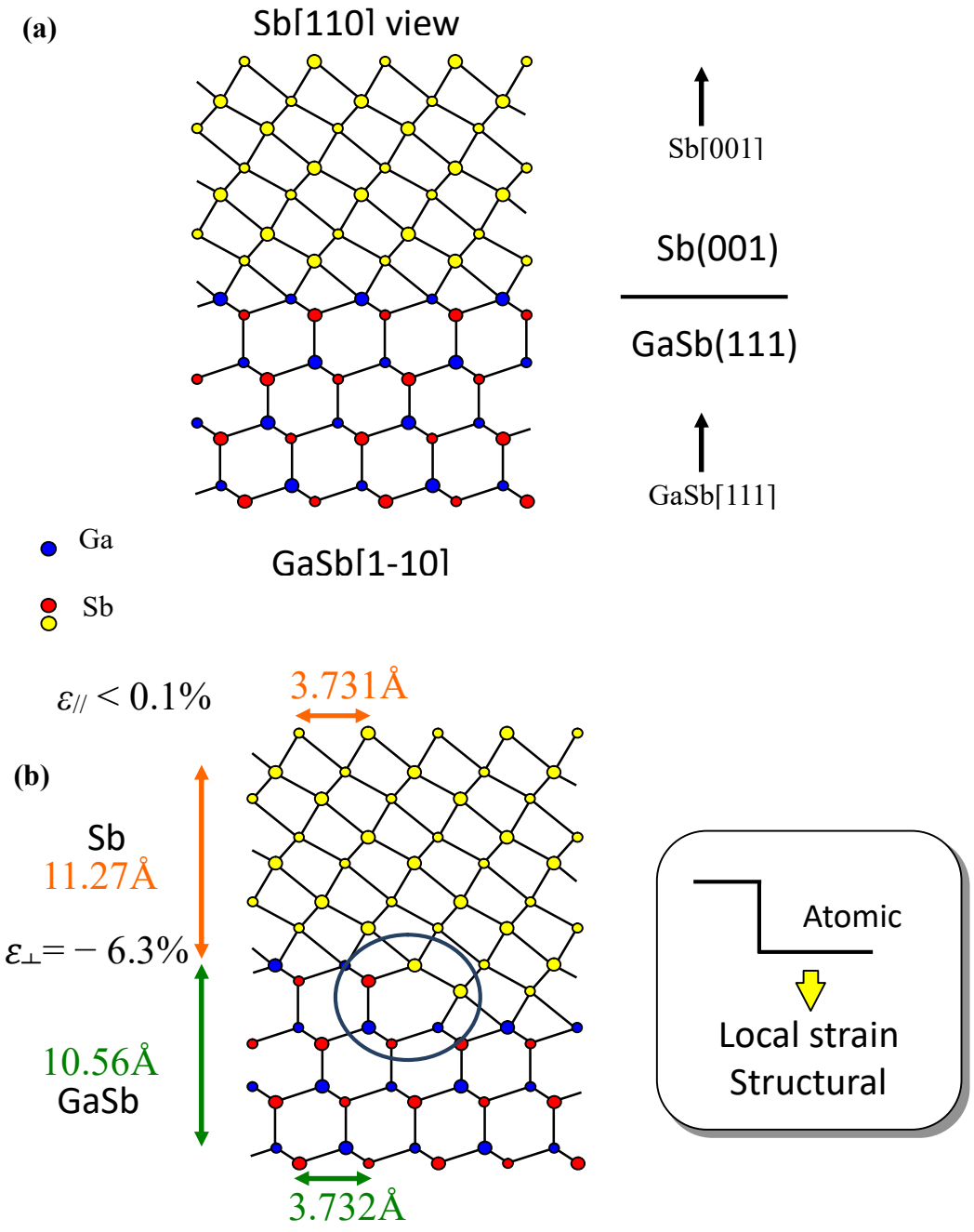

Figure 4.12. (a) An example of an interface structure of Sb/GaSb with no step edge and (b) Sb/GaSb structure with step edge.

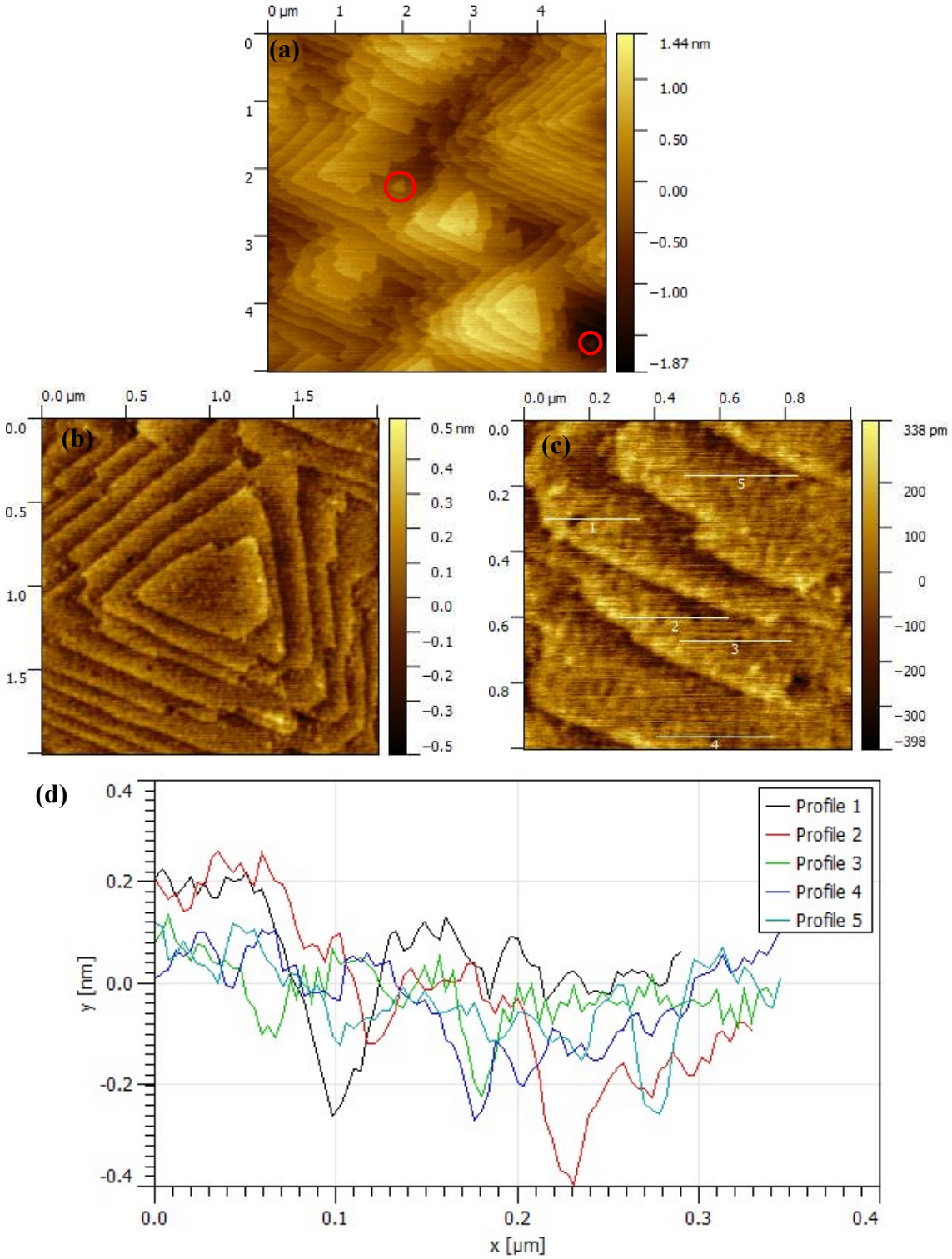

Figure 4.13. GaSb epilayer on a Wafer Tech substrate. AFM images of the scan size (a) 5×5µm, (b) 2×2µm and (c) 1×1µm. (d) Height profile across the pores of the AFM image (c).

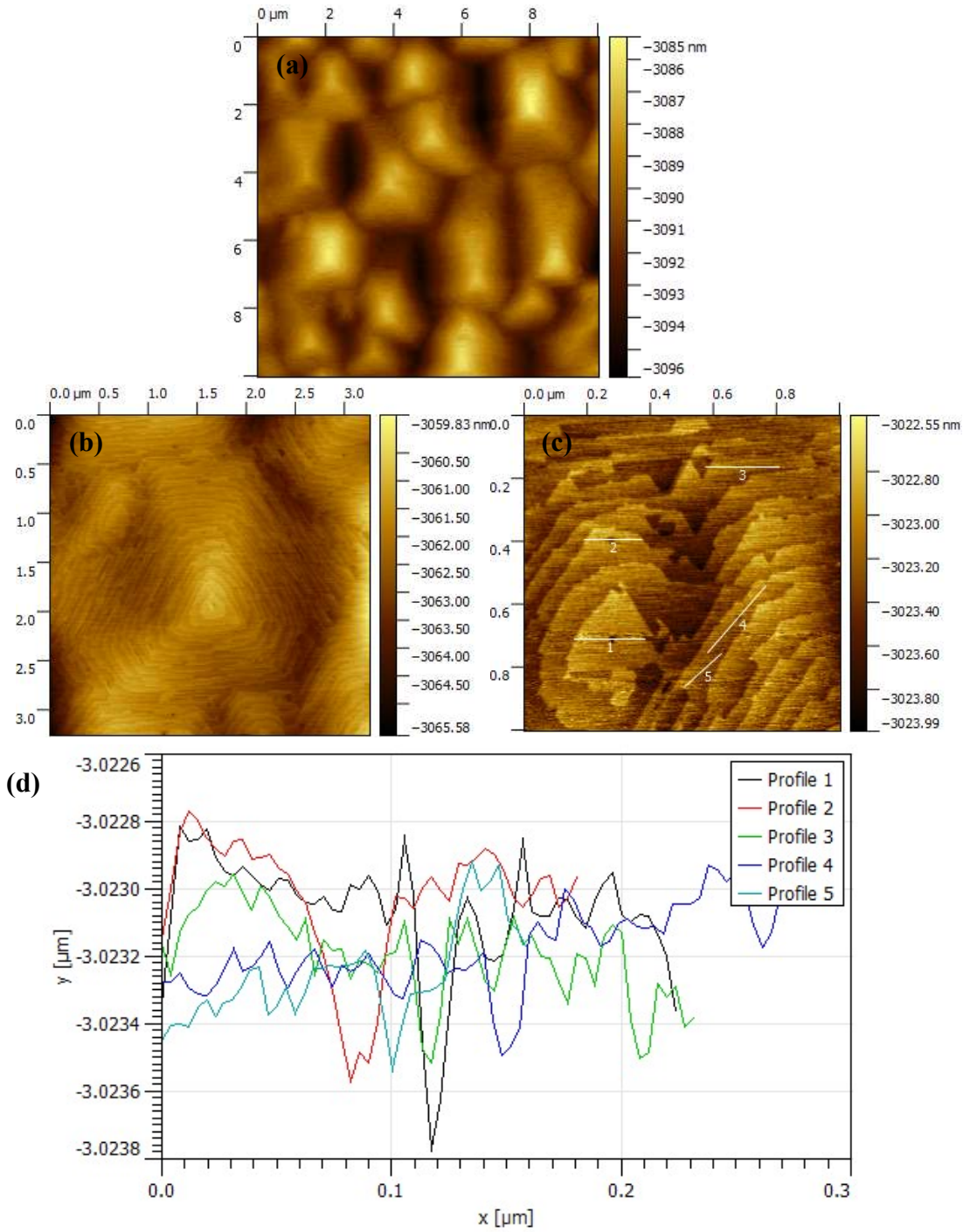

Figure 4.14. GaSb epilayer on grown on Galaxy substrates. (a), (b), and (c) are AFM images with scan areas of 10 ×10 µm, 5×5 µm and 1 ×1 µm. (d) Height profile across the pores of the AFM image (c).

A plan-view AFM image of a 3.8 nm thick Sb QW with a 36 nm GaSb cap is shown in Fig. 4.15. This is the same structure analyzed using TEM in Fig 4.4. The root mean square roughness is 1.1 nm and peak to valley height is ~ 7.9 nm. Since the cap thickness found using cross-section TEM was 36 nm, the underlying Sb layer is completely covered so that Sb is not oxidized. The incomplete top GaSb layers appears as truncated triangular shape islands. We observe that almost all of the islands have a dent-like defect at the peak with a depth from ~0.1 nm (Fig (c), profile 8) to ~2.2 nm (Fig (c), profile 1). Measured depth can be limited by the AFM tip capabilities, deepest dent may be deeper than we observed. Because, GaSb was grown on GaSb (111)A substrates, the appearance of these defect is not expected. Threading dislocations were observed for the Sb structures grown on GaAs (111)A substrates due to the 7.8% lattice mismatch with GaSb [42]. We speculate that these defects may have been generated via strain due to a low surface mobility that prevented atoms from forming a smooth surface before the next layer started growing.

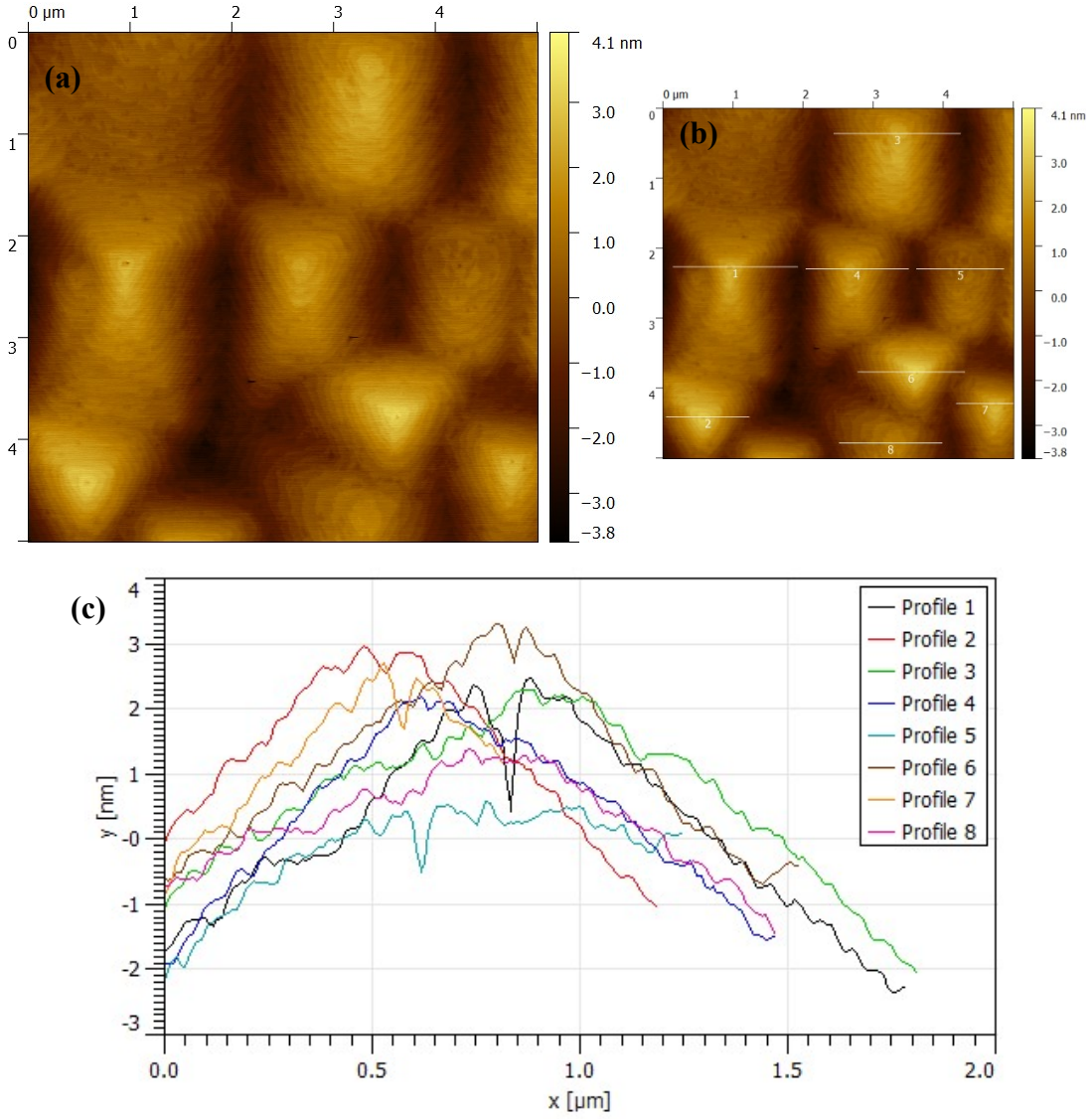

Figure 4.15. (a) 3.8 nm thick Sb layer capped with 36 nm GaSb cap layer. (b) and (c) Height profiles across the peaks showing the depths of the dents on top of the peaks.

4.4 Summary

We successfully developed a non-conventional method to grow ultra-thin Sb layers with control over thickness down to a few angstroms. Using FESEM and AFM, we analyzed the structural properties of Sb layers. We observed good crystalline quality with an Sb surface roughness (root mean square roughness) of ~ 0.45 nm for the samples gown on WaferTech substrates. Sb grown on Galaxy wafers had a roughness of ~1.25 nm. Oxide desorption on Galaxy substrates is always partial (see Figure A1) which promoted the GaSb epilayer to grow in 3D rather than in 2D. This provided a rough surface for Sb to grow. Hence the roughness Sb layer is high for those grown on Galaxy substrates. Further, we investigated all the features that appeared on FESEM images, most importantly the dark-line contrasts and pores that exist at the Sb/GaSb interface and which likely affect the TI behavior of the surface electrons. Because of these features, the mobility of the surface carriers are expected to have a lower value than the theoretically calculated values.

Chapter 5: Transport Properties Via Hall Effect and Magnetotransport Measurements

5.0 Introduction

A wide variety of methods are available to measure the physical properties of novel materials. Magneto-transport (MT) measurements probe the electronic behavior as a function of applied magnetic field. Using this method, we can determine electrical properties such as resistivity, conductivity, carrier density and carrier mobility. This chapter covers the basics of the methodology employed in MT measurements.

5.1 The Drude Model of Electrical Conduction

The Drude model is a classical description proposed by Paul Drude to explain the transport properties of electrons in a material. For a conduction electron moving through a solid in response to a uniform applied electric field $\boldsymbol{E}$, the equation of motion is [44]

$$\boldsymbol{F} = m^* \frac{d\boldsymbol{v}}{dt} = q\boldsymbol{E} \tag{5.1}$$

where $\boldsymbol{F}$ is the external force acting on the electron and m^*, $\boldsymbol{v}$, and q, are the effective mass, velocity, and charge of the electron, respectively. In the model, scattering by a perfect crystal results in an effective mass that is different from the free electron mass. Scattering from crystal defects, surfaces, phonons, or other deviations from perfect crystallinity limit the velocity. Electrons reach a steady-state velocity, called the drift velocity, of

$$\boldsymbol{v_d} = \frac{q\tau_e}{m^*}\boldsymbol{E} \tag{5.2}$$

where τ_e, called the scattering time, is the average time between the elastic scattering events due to phonons, defects, impurities, etc. For n electrons per unit volume, the electron current density $\boldsymbol{J}$ is

$$\boldsymbol{J} = nq\boldsymbol{v_d} = \frac{nq^2\tau_e}{m^*}\boldsymbol{E} \tag{5.3}$$

This is Ohm's Law where the electrical conductivity σ is defined as

$$\boldsymbol{J} = \sigma\boldsymbol{E} \tag{5.4}$$

Therefore, the electrical conductivity according to the Drude model is

$$\sigma_o = \frac{nq^2\tau_e}{m^*} \tag{5.5}$$

At zero magnetic field, the resistivity ρ_o and mobility μ are

$$\rho_o = \frac{1}{\sigma_o} \tag{5.6}$$

$$\sigma_o = \frac{nq^2\tau_e}{m^*} = nq\mu \tag{5.7}$$

$$\mu = \frac{q\tau_e}{m^*} \tag{5.8}$$

In the presence of a uniform electric field in the x-y plane and a magnetic field in the z direction, the equation of motion for a conduction electron is

$$\boldsymbol{F} = m^*\frac{d\boldsymbol{v}}{dt} = q(\boldsymbol{E} + \boldsymbol{v}\times\boldsymbol{B}) \tag{5.9}$$

When the velocity reaches a steady state, equation 5.9 in component format becomes

$$\frac{m^*v_x}{\tau_e} = q(E_x + v_yB) \tag{5.10}$$

$$\frac{m^*v_y}{\tau_e} = q(E_y - v_xB) \tag{5.11}$$

Rearranging the equations 5.10 and 5.11 for $\boldsymbol{E}$ and writing electron velocities, v_x and v_y in terms of current densities, J_x and J_y, the matrix form gives

$$\begin{pmatrix} E_x \\ E_y \end{pmatrix} = \frac{1}{\sigma_o}\begin{pmatrix} 1 & -\mu B \\ \mu B & 1 \end{pmatrix}\begin{pmatrix} J_x \\ J_y \end{pmatrix} \tag{5.12}$$

Equation 5.12 is the inverse of Ohm's Law and can also be written as

$$\begin{pmatrix} E_x \\ E_y \end{pmatrix} = \begin{pmatrix} \rho_{xx} & \rho_{yx} \\ \rho_{xy} & \rho_{yy} \end{pmatrix}\begin{pmatrix} J_x \\ J_y \end{pmatrix} \tag{5.13}$$

where,

$$\rho_{xx} = \rho_{yy} = \frac{1}{\sigma_o} = \frac{1}{nq\mu} \tag{5.14}$$

$$-\rho_{xy} = \rho_{yx} = \frac{B}{nq} \tag{5.15}$$

If the conducting layer is quasi-two-dimensional, a 2D density (n_{2D}) is substituted for n. Then ρ_{xx} and ρ_{xy} are also known as longitudinal resistivity and transverse or Hall resistivity, respectively. $1/n_{2D}q$ is the Hall coefficient (R_H); negative for electrons and positive for holes. Inverting 5.13 gives

$$\begin{pmatrix} J_x \\ J_y \end{pmatrix} = \frac{\sigma_o}{(1+\mu^2B^2)}\begin{pmatrix} 1 & \mu B \\ -\mu B & 1 \end{pmatrix}\begin{pmatrix} E_x \\ E_y \end{pmatrix} \tag{5.16}$$

which is the matrix form of Ohm's Law in an external magnetic field. This also can be written as

$$\begin{pmatrix} J_x \\ J_y \end{pmatrix} = \begin{pmatrix} \sigma_{xx} & \sigma_{xy} \\ \sigma_{yx} & \sigma_{yy} \end{pmatrix}\begin{pmatrix} E_x \\ E_y \end{pmatrix} \tag{5.17}$$

where the conductivity tensor gives

$$\sigma_{xx} = \sigma_{yy} = \frac{\sigma_o}{(1+\mu^2B^2)} \tag{5.18}$$

$$\sigma_{xy} = -\sigma_{yx} = \frac{\sigma_o\mu B}{(1+\mu^2B^2)} \tag{5.19}$$

5.2 Measurements of Transverse Resistivity and Longitudinal Resistivity

The van der Pauw method is a widely-used technique to measure the resistivity and Hall effect of a conducting sample. This can be used for any flat sample of arbitrary shape with some conditions: contacts should be sufficiently small and located at the perimeter of the sample. The influence of the contact size is eliminated by using a clover shaped sample as shown in Figure 5.1 (a). Since fabricating a clover shaped sample would require additional processing steps, we instead make a square sample by cleaving. As shown in Figure 5.1 (b), this is acceptable if the contact material is placed at the corners and reaches the circumference. Also, the conducting layers should be homogeneous and simply connected (i.e. sample should not have any holes) [45].

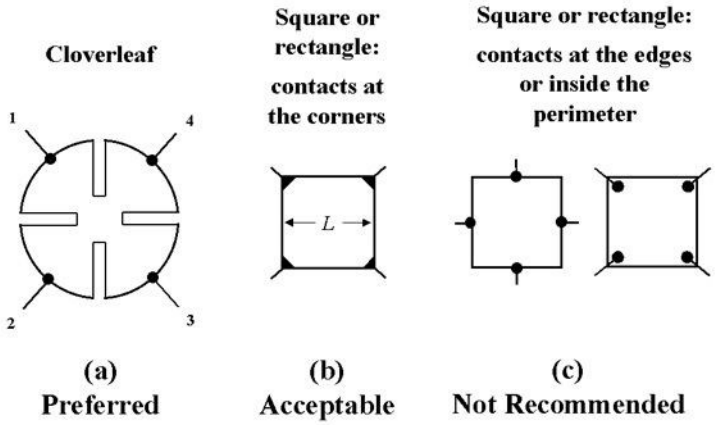

Figure 5.1. Different geometries for the van der Pauw method. (a) The cloverleaf is preferred because its shape reduces the effect of contacts considerably [3]. (b) Square geometry with contacts completely covering the corners; most commonly used geometry. (c) Square geometry with contacts at the edge or inside the perimeter, which is not recommended. Images are taken from NIST web page [46].

To study electron transport properties, we used 5 ×5 mm square pieces cleaved from the wafers grown in MBE. We used a diamond scriber to cleave the samples and used pressurized dry nitrogen gas to blow the wafer dust away from the surface. Electrical contact was made at each corner of the square sample by soldering 99.99% pure gold wire with an indium (In) dot as shown in Figure 5.2. Indium dots which are pressed onto the samples surface are shown as black triangles at each corner. The soldering iron was heated to ~ 280 °C to melt the indium.

The indium contacts were not annealed in order to prevent parallel conduction through the underlying GaSb epilayer, which would obscure the Sb QW's contribution to the conductivity. Caution was taken to prevent the direct contact of the tip of the soldering iron with the sample to avoid unintentional annealing of indium dots. However, for undoped Sb samples, we applied an indium dot directly on to the sample surface at the corner and then pressed the gold wire onto the In dot. This procedure may have caused some annealing of In, which helps the In atoms to diffuse through the sample to some unknown depth. For all remotely n-doped Sb samples, we made the contact by applying Indium onto the gold wire and then pressing the wire onto the surface using a fine tweezer to minimize unintentional annealing of In.

We used a closed cycle helium cryostat to cool down the samples from 300 to 20 K. This system is equipped with an electromagnet capable of generating a magnetic field only up to 0.15 T. For very low temperature measurements in the range 15 to 50 mK and high magnetic fields up to 18 T, we used the facilities at the National High Magnetic Field Laboratory (NHMFL) in Tallahassee, Florida. Ohmic behavior was

checked through observation of linear current-voltage characteristics in two-point measurements.

Hall-effect measurements in the van der Pauw geometry were made to determine the carrier density, resistivity and mobility in the structures grown by MBE. It is easier to explain Hall effect using the rectangular sample geometry shown in Figure 5.3. When a current I is passed through a rectangular piece of conducting material in the direction x, and placed in a weak magnetic field B in the z direction (see Figure 5.1), electrons experience a Lorentz force that deviates their path from the x direction and drives them in a curved path toward an edge with a normal component in the y direction. As electrons accumulate at the edge, an electric field is built in the y direction. A steady state is reached when that electric field cancels the y-component of the Lorentz force. At steady state, the current flows in the x direction and a potential is created at the edge. The Hall voltage V_H is measured between a point on that edge and the point directly across on the opposite edge. The quantity V_H/I is called the Hall resistance.

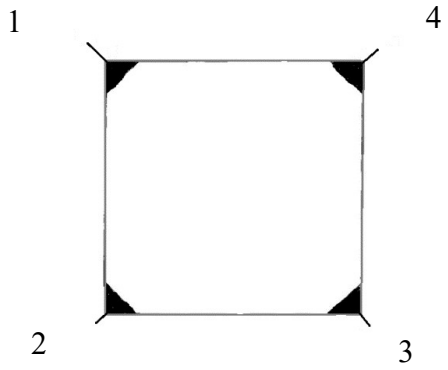

Figure 5.2. Square sample with four contacts made with indium and 99.99% pure gold wires.

Recall equations 5.13 to 5.15 where $q = -e$ for an electron and $q = e$ for a hole. Since the current I flows only in the x direction, $I = J_x wd$, $V_H = E_y$w, and therefore the Hall resistance (transverse resistance) can be written as

$$\frac{V_H}{I} = \frac{E_y}{J_x w} = \frac{B}{nwq} = \frac{\rho_{yx}}{w} = \frac{V_{24}}{I_{13}} \tag{5.20}$$

V_{24} is the Hall voltage measured between terminals 2 and 4 while I_{13} is the current passed through terminals 1 and 3, as shown in the van der Pauw geometry in Figure 5.4 (b). If the conducting layer is quasi-two-dimensional, n_{2D} is substituted for n w and the Hall voltage equals ρ_{yx}, the 2D transverse resistivity.

The sheet carrier density or the 2D carrier density, n_{2D}, is found from the slope of the plot of Hall voltage versus the magnetic field, R_H (Hall coefficient);

$$R_H = -\frac{1}{n_{2D} e} \tag{5.21}$$

Sheet carrier density relates to 3D carrier density n,

$$n = \frac{n_{2D}}{d} \tag{5.22}$$

where d is the thickness of the conducting layer. For a 2D layer, the mobility can be calculated using the longitudinal resistivity at $B = 0$ (equation 5.14),

$$\mu = \frac{1}{e\rho_{xx} n2_D} \tag{5.23}$$

In this case the longitudinal resistivity is the 2D resistivity, and at $B = 0$ it can be written as,

$$\rho_{xx} = \frac{V_x}{I_x} \tag{5.24}$$

For a square sample in the van der Pauw geometry, the 2D resistivity is calculated using the four-point resistances as,

$$\rho_{xx} = \frac{\pi}{ln2}\left[\frac{R_{12,43} + R_{23,41} + R_{34,12} + R_{41,23}}{4}\right] \tag{5.25}$$

where $R_{12,43}$ is the four-point resistance given by,

$$R_{12,43} = \frac{V_{12}}{I_{34}} \tag{5.26}$$

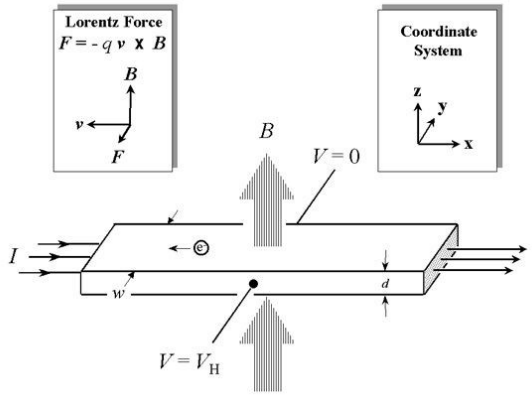

Figure 5.3. Schematic of the Hall effect in a long rectangular piece of conducting material with current passed along the long dimension, with a width of *w* and a thickness of *d*. Current flows in the x-direction and a weak magnetic field is applied in z-direction. The Hall voltage is detected along the y-direction [46].

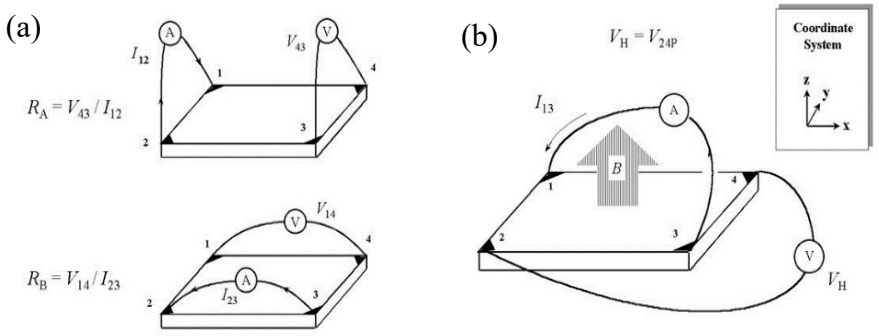

Figure 5.4. The van-der Pauw geometry for a square piece of conducting material with contacts at the corners. A magnetic field *B* is applied in the *z* direction. (a) Current is passed through adjacent contacts to determine the 2D resistivity. (b) Current is passed between contacts at diagonal corners to determine the Hall voltage [46].

In this equation V_{12} is the voltage measured between terminals 1 and 2 and I_{34} is the current measured through the terminals 3 and 4. $R_{23,41}$, $R_{34,12}$, and $R_{41,23}$ are defined similarly. If the sample is perfectly square and the ohmic contacts are small, the four resistance values in in Equation 5.25 will be equal.

Equation 5.21 is derived for a single carrier type. If two carrier types are present, electrons and holes, the Hall coefficient at low magnetic field is

$$R_H = \frac{n\mu_n^2 - p\mu_p^2}{e(n\mu_n + p\mu_p)^2} \tag{5.27}$$

where n, p, μ_n, and μ_p, are 2D electron density, 2D hole density, electron mobility and hole mobility respectively. When four different conducting channels are present in a single structure, with electron carrier density n_1, n_2 and hole density p_1, p_2 and electron mobility μ_{n1}, μ_{n2} and hole mobility μ_{p1} μ_{p2}, the Hall coefficient is

$$R_H = \frac{n_1\mu_{n1}^2 + n_2\mu_{n2}^2 - p_1\mu_{p1}^2 - p_2\mu_{p2}^2}{e(n_1\mu_{n1} + n_2\mu_{n2} + p_1\mu_{p1}p_2\mu_{p2})^2} \tag{5.28}$$

We will return to this equation in chapter 7.

5.3 Landau Levels and Shubnikov-de Haas Effect

The behavior of electrons in a weak magnetic field is explained by the Drude model. But in a strong magnetic field, the behavior is somewhat different. When a magnetic field $\boldsymbol{B}$ is applied (in the z direction) to an electron moving in x direction, it executes a spiral motion (while in a cyclotron motion on the xy plane it moves forward) with an angular frequency ω_c given by

$$\omega_c = \left|\frac{eB}{m^*}\right| \tag{5.29}$$

where m^* is the effective mass of the electron.

At most temperatures and with low magnetic fields, this ordered movement is fragmented by collisions. With strong magnetic fields and at very low temperatures (a few degrees above absolute zero), the effect of collisions is suppressed because many of the electrons complete a cyclotron orbit before scattering. Under these extreme conditions the classical theory becomes less applicable and the effects of *quantization* become apparent, as an electron's energy can only assume certain definite values. These energy values are called Landau levels [47].

5.3.1 Landau gauge for quantum mechanical behavior of electron's Hall resistivity

We can write the Hamiltonian equation for an electron in crossed electric and magnetic field as

$$H = \frac{1}{2m}(\boldsymbol{P} + e\boldsymbol{A}(\boldsymbol{R}, t))^2 + eV(\boldsymbol{R}, t) \tag{5.30}$$

Consider a vector potential $\boldsymbol{A} = (0, Bx, 0)$ in the Landau gauge. This allows us to choose a wave function described by a plane wave propagating in the y direction multiplied by a function of x, which can be written as

$$\Psi(x, y) = \Phi(x)e^{-ik_y y} \tag{5.31}$$

Then the Schrödinger equation becomes,

$$\left[-\frac{\hbar^2}{2m}\frac{d^2}{dx^2} + \frac{1}{2}m\omega_c{}^2\left(x + \frac{\hbar k_x}{eB}\right)^2\right]\Phi(x) = \mathrm{E}\Phi(x) \tag{5.32}$$

This is similar to the harmonic oscillator case with a cyclotron frequency ω_c and the vertex of the parabolic potential at $x_k = -\hbar k_x/eB$. The length scale is known as the magnetic length and is given by

$$l_B = \sqrt{\frac{\hbar}{m\omega_c}} = \sqrt{\frac{\hbar}{eB}} \tag{5.33}$$

From the solutions of the Schrödinger equation in a magnetic field, the most important aspect is the energy spectrum. The energy is given by

$$\varepsilon_{nk} = (N - \tfrac{1}{2})\hbar\omega_c \tag{5.34}$$

where, $N = 1,2,3..$ These discrete states are called Landau levels. The energy depends only on N, so the states with same N and different k values are degenerate.

For 2D systems, the degeneracy of a Landau level can be found by assuming a rectangle of dimensions $L_x \times L_y$ and using the Landau gauge. Periodic boundary conditions along y and the restrictions from L_x for x_k to lie inside the sample give the limits [48],

$$-L_x < \frac{2\pi\hbar j}{eBL_y} < 0, \ \frac{eBL_xL_y}{h} < j < 0 \tag{5.35}$$

where j is an integer. Therefore, the number of states in each Landau level per unit area a is given by

$$n_B = \frac{eB}{h} \tag{5.36}$$

This also can be written in terms of the effective mass m^* and cyclotron frequency ω_c as

$$2n_B = \frac{m^*}{\pi\hbar^2}\hbar\omega_c \tag{5.37}$$

This relation tells us that each Landau level (counting both spins) holds the same number of carriers as the original band over a range of $\hbar\omega_c$. Because this is also the separation between the Landau levels, this points out an important result that the density of states averaged over many Landau levels does not change due the applied magnetic

field. Instead, each block of width $\hbar\omega_c$ has collapsed into a δ-function at its center as shown in Figure 5.5 (a).

The density of states of a Landau level is a sharp δ function only in the absence of any kind of scattering of electrons. In the realistic case, each Landau level has a finite width of Γ and overlaps if $\hbar\omega_c < \Gamma$. The Landau levels are distinct when $\hbar\omega_c > \Gamma$ (see Figure 5.5 (b) and (c)).

As we raise the magnetic field from zero, the separation between the Landau levels grow linearly and the number of states that each level holds also grows linearly (see Figure 5.6).

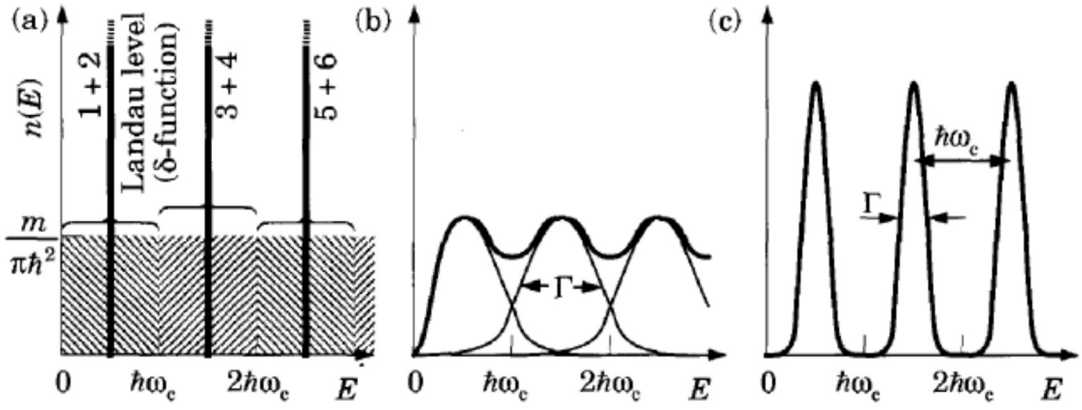

Figure 5.5. Density of states in a magnetic field, neglecting spin slitting. (a) The ideal case where each block of $\hbar\omega_c$ collapses into a δ-function Landau level. (b). Realistic case where the Landau levels having a non-zero width of Γ and overlap for $\hbar\omega_c < \Gamma$. (c) Distinct Landau levels when $\hbar\omega_c > \Gamma$ [48].

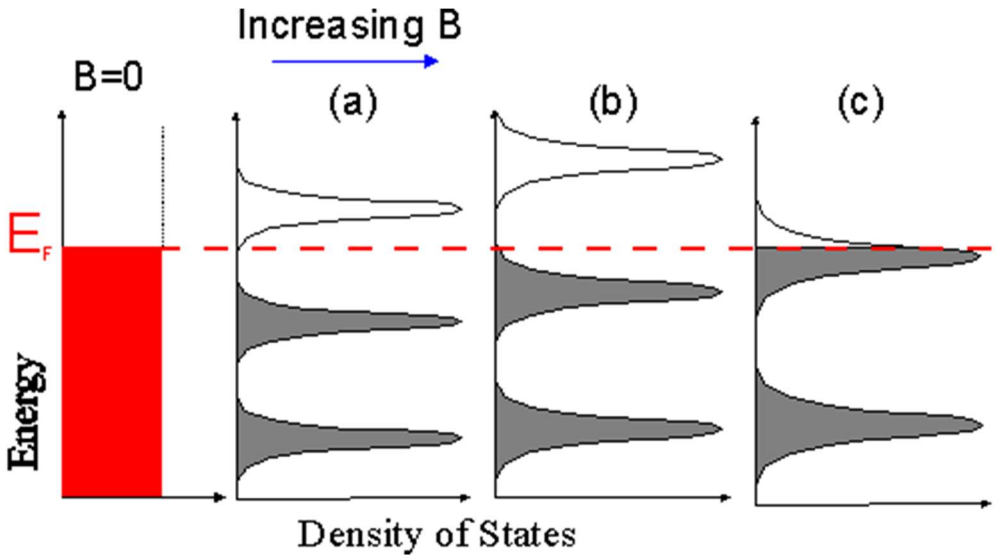

Figure 5.6. Density of states at the Fermi level changing with magnetic field. 2D electron density is held constant. Image taken from the web page http://www.twinkletoesengineering.info/quantum_hall.htm.

.

If the 2D electron density is held constant, the number of Landau levels must change. The number of occupied Landau levels or filling factor υ can be written as

$$\upsilon = \frac{n_{2D}}{n_B} = \frac{hn_{2D}}{eB} \tag{5.38}$$

In this definition, we count the two spins as separate levels. The filling factor is not always an integer. At zero temperature, suppose there are N Landau levels that are full and the $N + 1$ level is partially filled. When B is raised further, the Landau levels move up in energy and number of states in each level grows. So fewer electrons occupy the top level and the top level becomes empty when υ =N, at a field B_n;

$$B_n = \frac{hn_{2D}}{en} = \frac{hn_{2D}}{e\upsilon} \tag{5.39}$$

where there are exactly n full Landau levels.

5.3.2 Shubnikov-de Haas Oscillations (SDH)

The density of states at the Fermi level changes as a function of applied magnetic field (see Figure 5.6). When υ =N, this drops to zero. This is manifested in several physical quantities, including the longitudinal resistivity ρ_{xx}. A representative of this measurement is shown in Figure 5.7. At low field, ρ_{xx} is constant but develops strong oscillations with increasing magnetic field, which are called Shubnikov-de Haas oscillations (SdH). Minima occur at the fields B_N when υ =N because the density of states at the Fermi level vanishes. In other words, there is an energy gap between the filled and empty states. Since this minimizes scattering, ρ_{xx} is minimized and the values for B_N are easily identified from the experimental data. The slope of the plot of υ against $1/B_n$ is a straight line through the origin (equation 5.39) with the slope, S;

$$S = \frac{hn_{2D}}{e} \tag{5.40}$$

We use this relation in chapter 7 to calculate the 2D electron density n_{2D}.

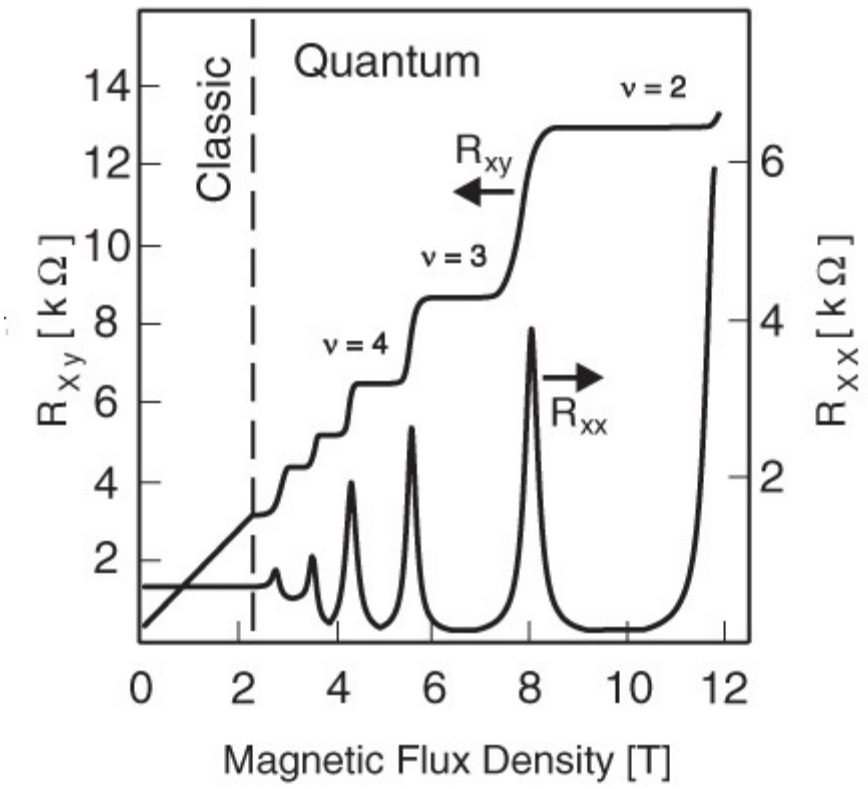

Figure 5.7. Transverse (ρ_{xy}) and longitudinal resistivity (ρ_{xx})for a 2D electron system in GaAs [49].

Chapter 6: Electrical Characterization of Undoped Sb Quantum Wells

6.0 Introduction

In this chapter, we discuss the electrical properties of ultra-thin Sb quantum wells (QW) grown on both substrates, GaAs (111)A and GaSb (111)A. In our initial experiments, we used GaAs substrates even though there is a large lattice mismatch with GaSb (~7%). The cost of GaAs substrates is much less and it is easier to thermally desorb the oxide layer from a GaAs substrate. A 3" GaAs substrate costs $85, while a 2" GaSb substrate costs $500. After establishing procedures for good Sb growth, we switched to GaSb substrates to reduce the defect densities. In this chapter, we discuss electrical resistivity of un-doped Sb thin films measured in the van der Pauw geometry using four wire measurements.

6.1 Analysis of the Surface Contribution for the Transport Measurements Using Zero Magnetic Field and High Magnetic Field Measurements

6.1.1 Sb QWs grown on GaAs (111)A substrates

The temperature dependence of the longitudinal resistance for a series of capped and uncapped Sb layers and a 500 nm thick GaSb epilayer are shown in Figure 6.1. Sb was deposited at a substrate temperature of 280°C with a nominal thickness ranging from 1 to 4 nm. There was a possibility that the GaSb cap layer could affect the measurements either by providing an alternate conduction path. In order to investigate this possibility, we measured the resistance of a 500 nm thick GaSb epilayer (sample T530 in Figure 6.1) grown on a semi-insulating GaAs (111)A substrate. From the measured two-dimensional resistivity, which is also known as a sheet resistance, of

8×10^3 Ω/□ at 20 K (4×10^3 Ω/□ at 300 K) for the GaSb epilayer, we calculated a resistivity of 6.7×10^5 Ω/□ at 20 K (3.3×10^5 Ω/□ at 300 K) for a 6 nm GaSb cap layer. This is a factor of 1600 to 3300 larger at 20 K (700 to 1700 larger at 300 K) than the measured resistance of the 2, 3 and 4 nm thick Sb structures shown in Figure 6.1, indicating that the conduction through the cap layer is negligible.

The measured resistivity of 1 nm and 1.5 nm capped Sb samples are comparable with the calculated resistivity of the GaSb cap layer, 6.7×10^5 Ω/□ at 20 K. In the most general case we expect all three layers, GaSb cap layer/Sb/GaSb epilayer to act as a three-parallel resistor network in which the resulting resistance should be lower than the resistance of each layer. Thus, even if the resistivity of the 1 nm or 1.5 nm Sb layer were higher than that of the GaSb epilayer, we expect the resultant resistivity to be less than the resistivity of the GaSb epilayer, 8×10^3 Ω/□ at 20 K. This explanation contradicts our experimental observations; therefore, we attribute the high resistance of these structures to a potential energy barrier, possibly a Schottky barrier between Sb and GaSb, that prevents the carriers from going into the GaSb epilayer. It is reasonable to assume that the GaSb cap layer acts as a potential barrier that confines carriers to the Sb layer.

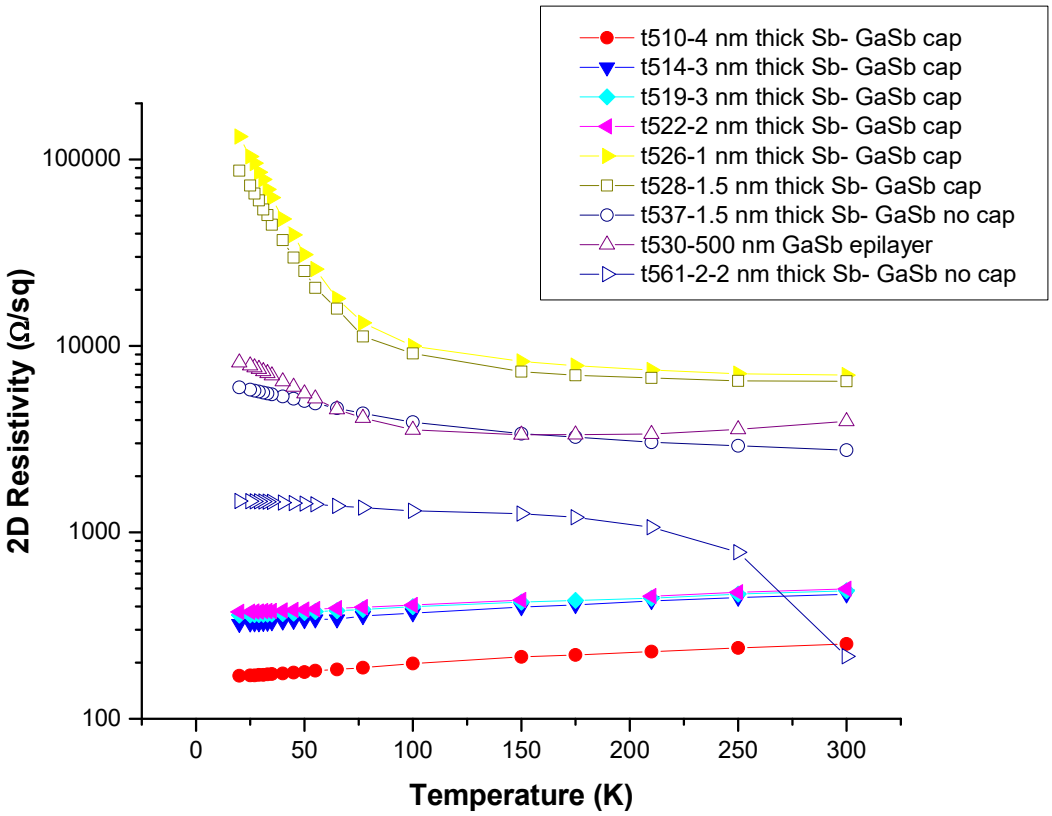

Figure 6.1. Temperature dependence of 2D electrical resistivity of ultra-thin Sb QWs with different thicknesses. All the structures were grown on GaAs (111)A substrates at a substrate temperature of 280°C for the QWs and ~570°C for the GaSb epilayer. The capped structures with an Sb layer thickness of 2 nm (T522), 3 nm (T514), and 4 nm (T510) behave as semi-metals. The structures with an Sb film thickness 1 nm and 1.5 nm are either insulating or semiconducting. The observed thickness dependence is consistent with the theoretical prediction by P. Zhang *et al.* [5]

The indium contacts made for van der Pauw measurements were deposited by hand using a soldering iron at ~180°C. Although the contacts were not subsequently annealed, heating by the soldering iron may be enough to diffuse a substantial fraction of Indium atoms into the 6 nm-thick GaSb cap layer. The formation of an InGaSb layer (which has a lower resistivity than GaSb) beneath the contacts would facilitate a path for electrons to the Sb layer. A similar explanation has been offered to explain Indium contacts to GaAs epilayers (Yano et al.). Hence, we predominantly measure the conduction through the Sb layer rather than through the GaSb barriers. Due to a limited supply of Sb QW material, we have not performed experiments to verify the effects of annealing on the measured resistivity.

It was observed that the 2 nm thick uncapped Sb structure (T561) was more resistive than the corresponding capped structure (T522). This we could expect because Sb oxidizes when exposed to air, which would decrease the Sb layer thickness and make it more resistive. On the other hand, the 1.5 nm thick uncapped Sb structure (T537) is less resistive than its corresponding capped structure (T528) and has almost the same resistivity as the GaSb epilayer (T530). We believe that for ultra-thin uncapped Sb structure, the indium contacts diffused into the GaSb epilayer, creating a parallel conduction path. The thickness of the GaSb cap layers (9 to 36 nm) prevented the indium from diffusing below the QW in the capped samples.

Since Sb oxidizes when exposed to air, it is important to completely cover the Sb layer with the GaSb cap layer. Otherwise interpretation of transport data would not be straightforward. FESEM analyses of all the structures included in Figure 6.1 show equally high Sb and GaSb coverage. Figure B1 of the appendix shows representative

FESEM images of all the structures included in Figure 6.1. In these images, the coverage of the Sb layer is ~96% [Figure B1.a] and the uncovered areas are not clustered together. Also, the GaSb cap layer [Figure B1.b] is complete. Therefore, it is fair to assume that the transport properties are for a complete Sb layer with a complete GaSb cap.

For all the Sb structures at a fixed temperature, the resistivity increases with decreasing film thickness. At low temperatures, the resistivity is approximately inversely proportional to the thickness of the films of thickness 2, 3, and 4 nm. This is a characteristic of a metal/semimetal. A semi-metallic character is further supported by the observation of relatively temperature independent behavior of the resistivity of these three Sb structures.

The resistivity of the 1 and 1.5 nm thick Sb structures increases with decreasing temperature and is much larger than the expected values obtained by extrapolating the thickness dependence of the 2, 3, and 4 nm thick Sb layers at any measured temperature from 300 to 20 K. This indicates that 1 nm and 1.5 nm Sb layers behave either like insulators or semiconductors.

Recent first-principles calculations by P. Zhang *et al*.[5] predict an opening of the band gap for bulk and surface states in an Sb layer with thickness ~ 1nm, thus predicting semiconductor behavior. Also, it was predicted for Sb layers with thickness ~ 1 nm to 2.7 nm, a conducting behavior through topological states but not through the bulk. Our observations in this experiment are consistent with the theoretical predictions but 2D transport measurements cannot discriminate between surface and bulk conduction. In the literature P. Fei *et al.*[50] found a similar qualitative semi-metal to

semiconductor transition for Bi films grown on Si (111) with film thickness of ~ 30 nm to 20 nm, and attributed the behavior to quantum confinement.

However, our experiments did not completely rule out that the possibility of the observed behavior as due to structural properties rather than quantum confinement. A more conclusive interpretation could be made with theoretical modeling that includes the effect of GaSb barrier layers and possible defects, and explicitly calculates the electrical resistance of the entire structure.

6.1.2 Sb QWs grown on n-type GaSb (111)A substrates

Figure 6.2 shows the temperature dependence of the resistivity of 16 different Sb QWs, capped (Figure 6.2.a) and uncapped (Figure 6.2.b) structures grown on GaSb (111)A substrates. We observe that the resistivity scales with Sb QW thickness, indicating that the major contributions for the transport measurements are from the carriers in the QW. This idea is supported by measurements of the resistivity of a GaSb epilayer grown on a Wafer Tech wafer (~ 9000 Ω/□ at 20 K) and a Galaxy wafer (~ 26,000 Ω/□ at 20 K) and calculating the resistance of the cap layers (see Figure 6.3 for the resistance of a GaSb epilayer). The calculated resistivity for the cap layers are in the range ~10^5-10^6 Ω/□ (for 36 nm – 9 nm) which are ~200× - 1400× greater than the resistivity of the QW.

The GaSb substrate is n-doped with tellurium and has a carrier concentration of 2×10^{17}cm^{-3}. Hall measurements of a 500 nm thick GaSb epilayer grown on n-doped GaSb substrate gives a negative Hall coefficient (~ 300 Ω/T), indicating p-type carrier conduction (see Figure B2). Assuming only one-carrier conduction through the epilayer,

the estimated hole concentration is ~4×10^{16} cm^{-3} and mobility is ~600 cm^2/V s. If there was a parallel path through the substrate, we would have seen clear n-type conduction. Since this was not observed, it is reasonable to assume that there is no parallel path through the substrate. Therefore, the assumption we made in the previous section that there is a Schottky barrier at the GaSb/Sb interface holds for the structures grown on GaSb (111)A substrates.

The temperature dependence is consistent with suppression of bulk conduction through quantum confinement and population of metallic surface states. As the temperature is reduced from room temperature, the resistivity increases, as expected if the Fermi level lies in a bandgap of bulk Sb. The resistivity saturates at low temperatures, as expected from metallic surface states. It is observed that there is a good repetition for resistance measurements for the samples with the same Sb thickness grown at different times, indicating that we have very good control over Sb layer thickness down to a few angstroms.

Similar to the structures grown on GaAs (111)A substrates, the uncapped Sb structures are more resistive than the capped ones due to oxidation reducing the thickness of the Sb layer. The resistivity of the uncapped structures with Sb thickness in the range of 3.8 nm - 5.5 nm is ~ 1.4 × greater than corresponding capped structures while for the 2.9 nm structure, the resistance is ~3.5 × greater than its corresponding capped structure. The plan view FESEM images and AFM images of all the uncapped structures included in Figure 6.2.b show complete coverage of Sb. Therefore, we attribute this behavior to oxidation rather than a percolation transition from incomplete coverage of Sb.

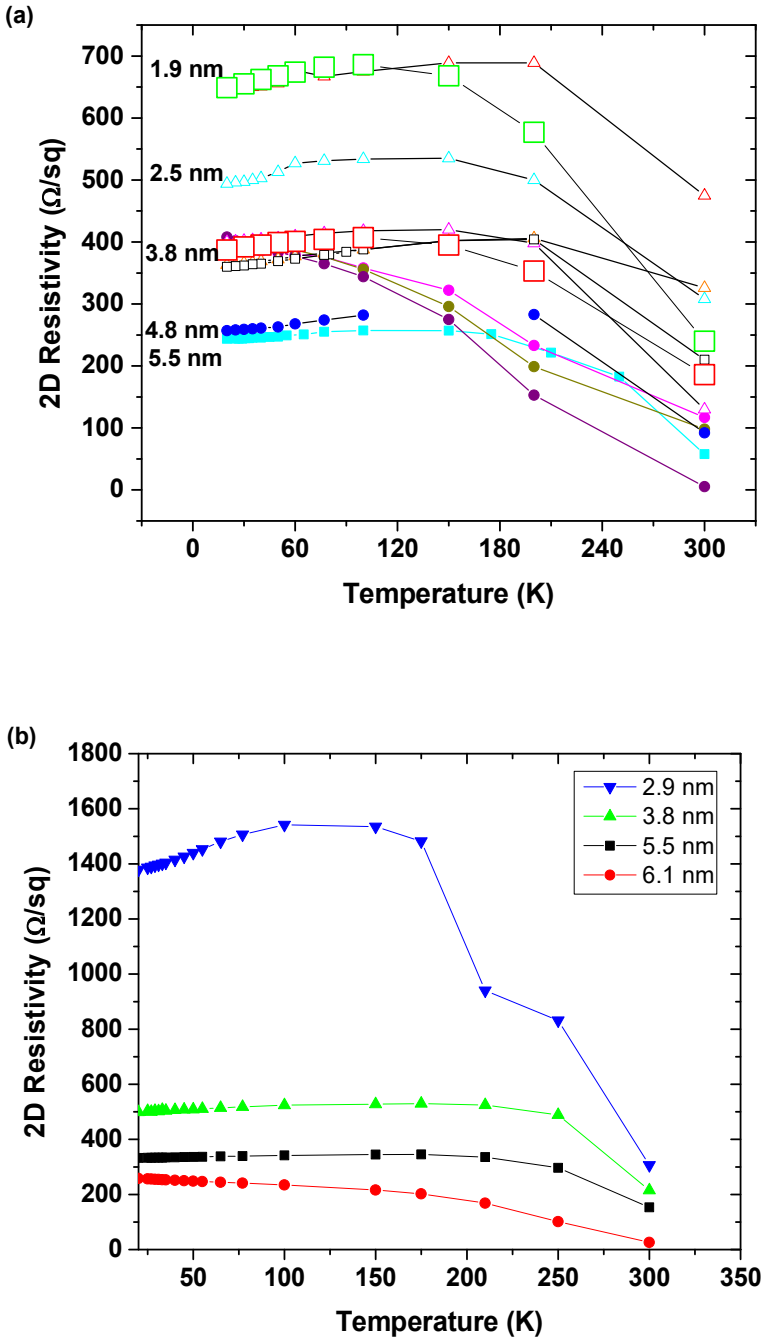

Figure 6.2. 2D electrical resistivity of ultra-thin Sb QWs as a function of temperature. All the structures were grown on GaSb (111)A substrates at a substrate temperature range of 160 - 180 °C for the QWs and ~570°C for the GaSb epilayer. AFM analysis of all structures shows complete coverage. (a) Structures with a GaSb cap in the thickness range 9 - 36 nm. (b) Sb structures with no GaSb cap. Since the Sb layer oxidizes, the resistivities are higher than for the capped structures due to the reduction in their effective thickness.

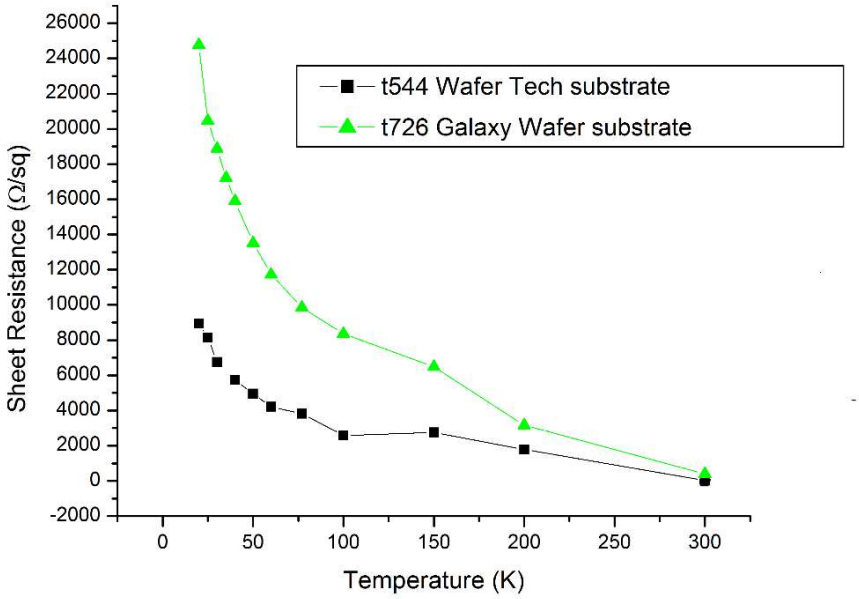

Figure 6.3. Temperature dependence of the resistivity of the GaSb epilayers grown on Wafer Tech substrate (T544) and Galaxy substrates (T726). The substrates are n-doped GaSb (111)A and the epilayers are grown at a temperature ~ 570 °C. The resistivities of the GaSb epilayers are 6× to 18× greater than the most resistive Sb structure, which has a 2.9 nm thick Sb layer with no GaSb cap.

Figure 6.4 shows the thickness dependence of the conductance for Sb quantum wells at 20 K. The solid blue line in this figure is the conductance we expect for a rectangular piece of bulk Sb, whose thickness is reduced by mechanical means to the values shown on the x-axis. Also, the conductance of the QWs are shown in open triangles (uncapped) and solid triangles (capped). We see that the conductance of the QWs are much less than the expected conductance of bulk-like films of equivalent thickness. This implies suppression of bulk conduction by quantum confinement. For comparison, we plotted the resistance of the GaSb epilayers in solid green squares, interpreting them as Sb QWs with zero thickness.

The 2D conductance of the QWs was modeled using equation 6.1;

$$G = G_s + \sigma_b t \tag{6.1}$$

where G_s, σ_b, and t are the 2D conductance due to surface states, the bulk conductivity, and the thickness of the QW, respectively. By fitting the experimental data to equation 6.1, we obtained the dashed line shown in Figure 6.4 which has a non-zero intercept, indicating finite conductance for zero film thickness, as expected for a topological insulator. Taking the conductance at zero film thickness as the contribution from the surface states to the total conductance of 3.8 nm thick Sb QW, we obtain a ~20% contribution from surface states.

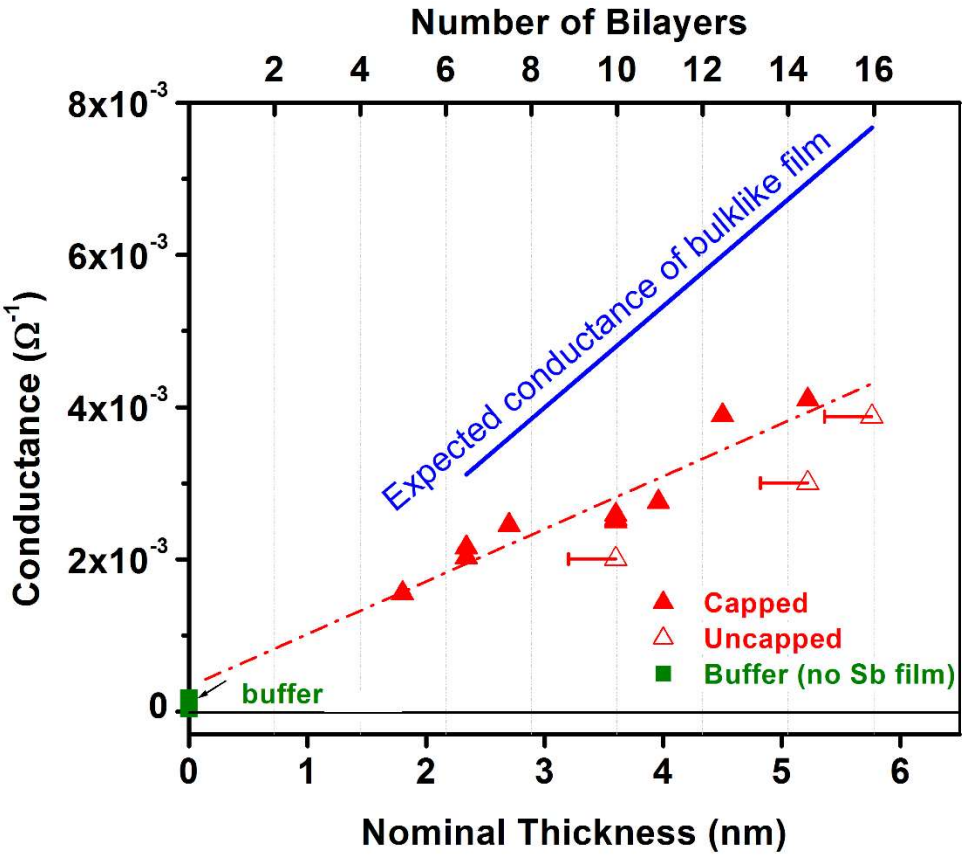

Figure 6.4. Conductance of Sb as a function of film thickness measured at 20 K [51]. The solid blue line is the expected conductance for a rectangular piece of bulk Sb, thinned to the values shown on the x-axis. It extrapolates through the origin of the plot. The curve fitted to the capped structures shows much less conductance compared to the bulk-like line indicating suppression of bulk conduction. Conductances of the buffer layers are shown in solid green squares, which are significantly smaller than for the Sb structures. This implies that the carriers in the QW are responsible for the observed conduction. When extrapolated, the fitted curve for the data intercept the y-axis at a non-zero value indicating the contribution from the surface states.

We conducted high-field magneto-transport measurements in tilted fields to find further evidence for 2D transport. Figure 6.5 shows tilt-dependent measurements for a GaSb-capped 5.5 nm-thick Sb QW, which is representative of all the QW structures. As we discussed in the paper by S. Cairns *et al.* [51], all the magnetoresistance data (R_{xx}, also called the longitudinal resistance) at different tilt angles for a given film, collapse onto a common curve when plotted as a function of perpendicular field. In other words, the parallel magnetic field has no effect.

The parallel magnetic field is expected to increase the confinement of the electrons and holes in the QW. The magnetic length, $l_B = \sqrt{h/eB}$, is the classical turning point for an electron or hole confined by the parabolic potential created by the parallel magnetic field. The electrons and holes in the QW are already confined by the barrier materials. For stronger confinement due to both effects, the bulk gap would increase and therefore R_{xx} would increase. The magnetic field's contribution to the confinement would have a noticeable effect at higher B as the magnetic length approached 2.25 nm, half the QW thickness of 5.5 nm. Unfortunately, the magnetic length is too large (6 nm) to be able to probe a confinement effect even for the maximum field available for our experiments (18 T). Therefore, we cannot discriminate between a surface state and bulk 2D subbands.

However, we can rule out conduction through the ~500 nm-thick GaSb epilayer because it is much thicker than the magnetic length of 6 nm at 18 T.

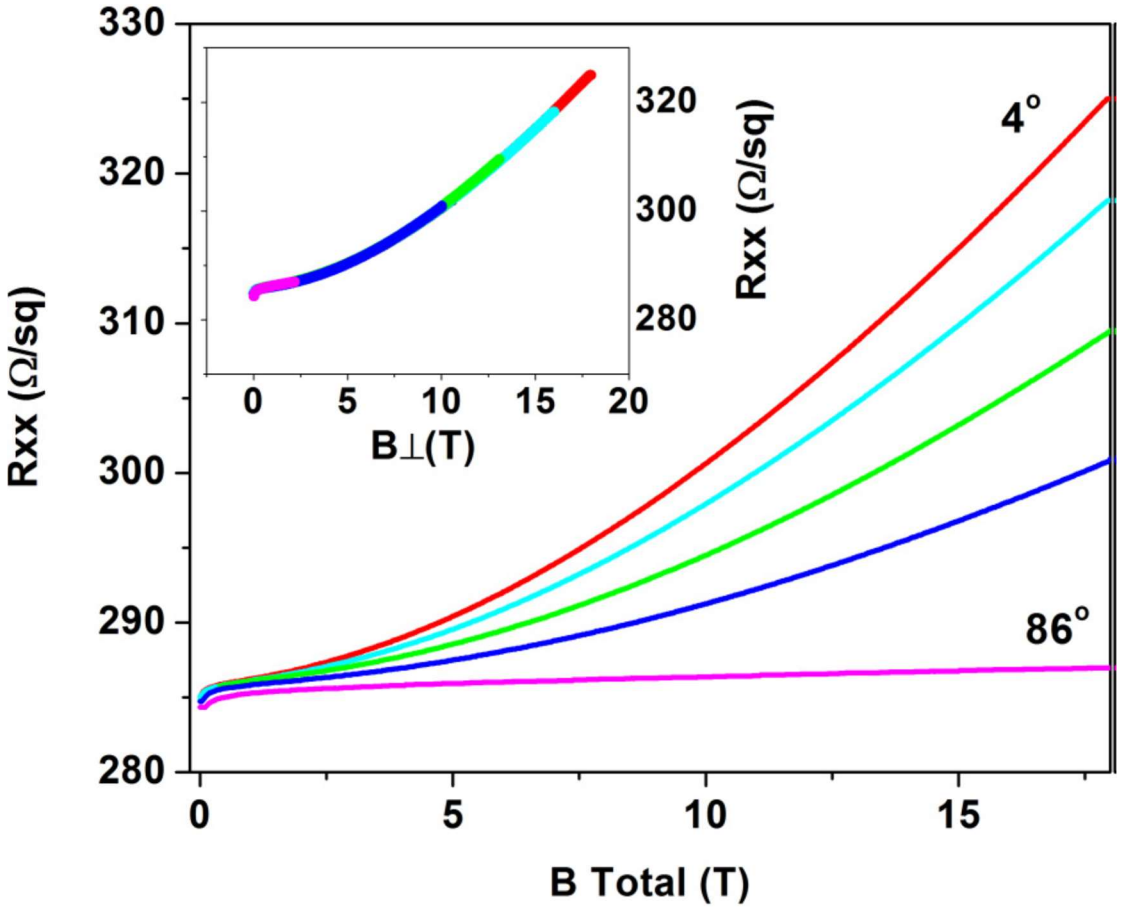

Figure 6.5. Magnetic field dependence of the longitudinal resistance, R_{xx}, in the tilted field geometry for 5.8 nm thick Sb QW with a GaSb cap [51]. The measurements were taken at 25 mK. The inset shows the behavior of the longitudinal resistance when plotted against the perpendicular magnetic field; all the curves collapse onto a common curve indicating the 2D nature of the carriers. This shows no evidence of 3D carriers participating in the conduction implying that there is no parallel path via the GaSb epilayer: carriers are confined to the QW.

We attempted to discriminate between surface and bulk carriers using Hall-effect measurements in both low and high magnetic fields. We fit a linear curve for the Hall resistance in low magnetic field (<0.15 T) as well as up to 18 T, for temperatures from 300 K down to 300 mK (see Figure B3 and C1 in the appendix). Assuming a single carrier model [equation 5.21], the estimated hole density was found to be ~5×10^{14} cm^{-2}, according to both low- and high-field data.

Spin resolved ARPES measurements reported by Takayama et al. for an undoped 6.8 nm-thick Sb QW showed an electron-like Fermi surface (FS1) enclosing the $\bar{\Gamma}$ point which is purely due to surface states. Whereas elongated hole-like Fermi surface (FS2) along the $\bar{\Gamma}\bar{M}$ line is a combination of bulk holes and surface holes (see Figure 6.6.a) [52]. Therefore, the appropriate model for our experiments should include multiple carrier types. In that model, the Hall voltage depends on the densities and mobilities of the holes and electrons. Therefore, 10^{14} cm^{-2} is an over estimate of the hole density for our structure. Attempts we made to fit multi-carrier model to the data using both Hall and magneto-resistance failed due to lack of constrains on the parameters.

A slightly negative Hall coefficient is consistent with the band structure mapped by ARPES measurements [52]. From the band structure calculated by Zhang et al. [5] , we estimated the surface carrier density to be between $(2 – 5) \times 10^{12}$ cm^{-2} and the mobility to be between 800 – 2000 cm^2/V s. Semi-metallic bulk Sb has equal electron and hole densities of $(3.74 – 5.05) \times 10^{19}$ cm^{-3} [53-55] but the electron mobility is five times larger than hole mobility [55]. Multiplying this 3D concentration by the QW thickness gives a 2D density of electrons and holes in the range $(1 – 2) \times 10^{13}$ cm^{-2}. By comparing the calculated band structures of bulk Sb [56] and ultra-thin Sb [5], it

appears that the Fermi level crosses the bulk hole band in almost the same place, despite the opening of a band gap. We conclude that the undoped 5.5 nm-thick QW has conductivity contributions from holes in the bulk, holes in the surface states, and electrons in the surface states, which combine to give a negative Hall voltage (p-type conduction). In a later chapter, we use the estimate of the bulk hole concentration for the starting point of experiments to n-dope Sb QWs.

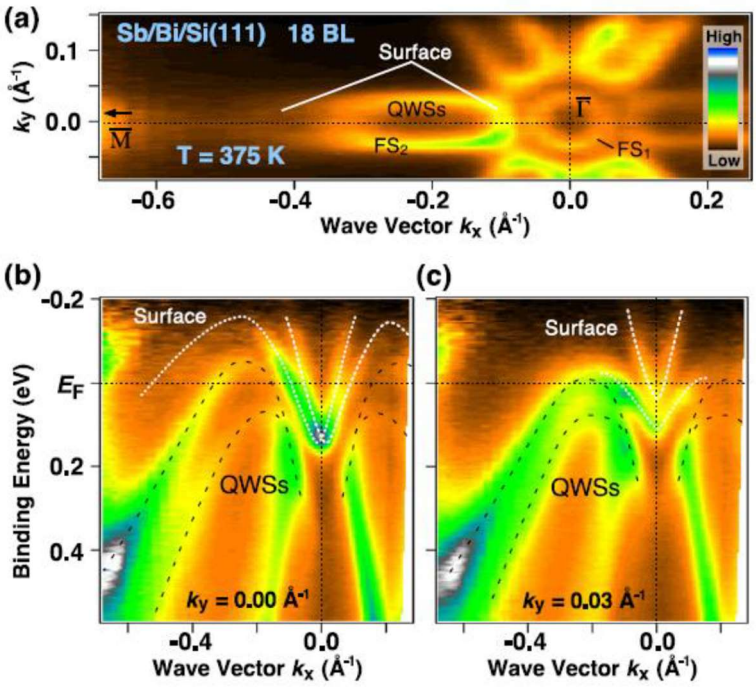

Figure 6.6. ARPES intensity map of a thin Sb film with a thickness of 18 BLs measured around the $\bar{\Gamma}\,\bar{M}$ line at 375 K. The Fermi level is crossing through the bulk hole band and both surface states, electron and hole. FS1 and FS2 are two Fermi surfaces which are filled with surface electron and surface holes respectively [52].

6.2 Summary

We studied the electrical properties of ultra-thin Sb QWs in the thickness range of 1 to 6 nm. In these structures, there was a GaSb cap layer and no undoping. Due to the presence of Schottky barriers at the Sb/GaSb interfaces, carriers are confined to the Sb layer. Thus, we predominately measure the transport properties of the Sb layer. FESEM and AFM images reveal a 100% to 96% coverage of Sb and a full coverage of the GaSb cap. Therefore, the behavior of longitudinal resistance and Hall measurements are due to their electronic structure rather than percolation through an incomplete Sb layer.

The longitudinal resistance of Sb QWs with thickness between 2 to 5.5 nm are ~ (1.5 – 1.7) times greater than the corresponding resistance of a bulk Sb piece thinned to the same thickness, implying suppression of bulk conduction due to quantum confinement [5]. Sb films with thickness 1.5 nm and below, have a significantly larger resistance, which is at least 90× larger than the resistance of the Sb films with thickness greater than 1.5 nm. This is attributed to the opening up of a gap for surface states as predicted from first-principles calculations [5].

The contribution of the surface states to the total conduction was deduced from the dependence of the low-temperature conductivity as a function of thickness. We found that for a thickness approaching zero, there would be a non-zero conductivity for the ultra-thin Sb film, which is attributed to the surface states. We deduced that the surface contribution for the total conduction of a 3.8 nm thick Sb film is approximately ~20%. Thus, we were successful in suppressing the bulk conduction via quantum confinement, yet unable to completely remove the bulk contribution.

We attempted to discriminate between surface states and bulk states by modeling data for longitudinal resistance and Hall data. Unfortunately, we failed to obtain a satisfactory result due to the lack of constraints on the parameters. Instead, using the band structure for ultra-thin Sb films, we estimated the electron and hole carrier density to be ~ (2-5) $\times 10^{12}$ cm^{-2} and mobility ~ (800-2000) cm^2/V s.

A very small and negative Hall coefficient was observed in both low (<0.15 T) and high (up to 18 T) magnetic fields which indicates that sum of multiple carrier contributions is slightly p-doped. We expect that the mobility of the electrons in surface states would be less than the theoretical value. This is due to the local strain present at the Sb/GaSb interface which makes the surface rough as we have discussed in chapter 4. Therefore, the low electron mobility in the surface states may be partially responsible for a small Hall coefficient. From the transport data we deduced that there is a bulk gap but the Fermi level crosses only the bulk hole band, which is consistent with ARPES band structure measurements [52]. Further, we predict that the residual bulk hole density lies in the range (1 – 2) $10^{13} cm^{-2}$ for the 5.5 nm-thick Sb QW.

Chapter 7: Electrical Characterization of Remotely n-Doped Sb Quantum Wells

7.0 Remotely Doped Sb Quantum Wells

As discussed in the previous chapter, since the conductivity measurements of un-doped ultra-thin Sb QWs show major hole contribution, we cannot clearly observe the quantized Hall conductance ($2e^2$ /h), though we have confirmed that there is surface contribution to conductivity. To enhance the conductivity of the surface states, we remotely n-doped the Sb QW at the Γ point. In this experiment, topological electron states are populated by doping the GaSb barrier with Tellurium (Te) atoms, creating donor states at the Γ point. Figure 7.1 shows the theoretically calculated band structure of an Sb film which has 3D TI states. At the Γ point of the QW, the topological electron states have a lower energy than any of the bulk conduction band minima and the energy of the surface state at the M point. Therefore, we expect the electrons to populate only the Sb surface states at the Γ point not the bulk states.

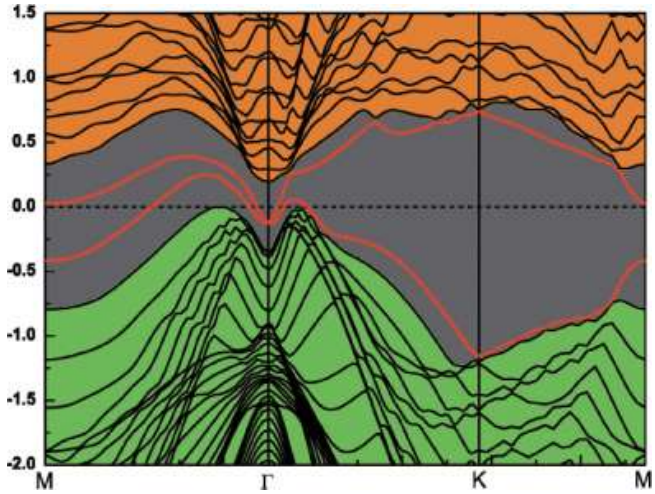

Figure 7.1. Theoretically calculated band structure of 11 BL thick Sb thin film taken from [5].

Since we predicted that the hole density in the bulk would be ~ (1 - 2) $\times 10^{13} cm^{-2}$ [53], Te doping density was targeted to be in the same order ($10^{13} cm^{-2}$). GaTe is used as the dopant source for Te because it has a melting point of ~790 °C, we limited the highest GaTe cell temperature to 600 °C to leave room for a difference between the thermocouple measured temperature and the real temperature. We used GaAs (111)A substrates for this study.

In this experiment, first we did a uniform Te doping calibration using the structure shown in Figure 7.2 (a) by fixing the dopant cell temperature at 600 °C and varying the thickness of the doping layer. The same substrate temperature was used for Te doped and Undoped GaSb epilayers. The same RHEED pattern (i.e. 2×6) was maintained during the doping and the surface looked shiny after the growth.

7.1 Remotely Doped Sb QWs in Low Magnetic Fields

For the preliminary study, we determined the carrier density using Hall effect measurements in a magnetic field of 0 - 0.15 T. The resistivity of the structures were determined from van der Pauw measurements at 300K to 20K. Electrical contact was made at each corner of a 5mm x 5mm square piece by pressing pure Indium dots which were not annealed. It was found that for a GaSb doping layer thickness of ~165 nm, the electron density is 3.5×10^{13} cm^{-2} which is in the required range if we assume that the doping density is equal to the electron density. Prior to uniform Te doping calibrations, we attempted for Te delta-doping with Ga_2Te_3 cell temperature of 600 °C, but we were unable to observe n-type carrier density possibly due to the p-type background doping.

We fixed the doping density at this value and the Sb QW thickness at 3.8 nm. Two different series of structures were grown as shown in Figure 7.2 (b) and (c) with varying GaSb spacer thickness. For the structures with a Sb QW more carriers are expected to transfer into the QW as the GaSb spacer is reduced. Structures with no Sb QW (Figure 7.2 (b)) were grown for comparison.

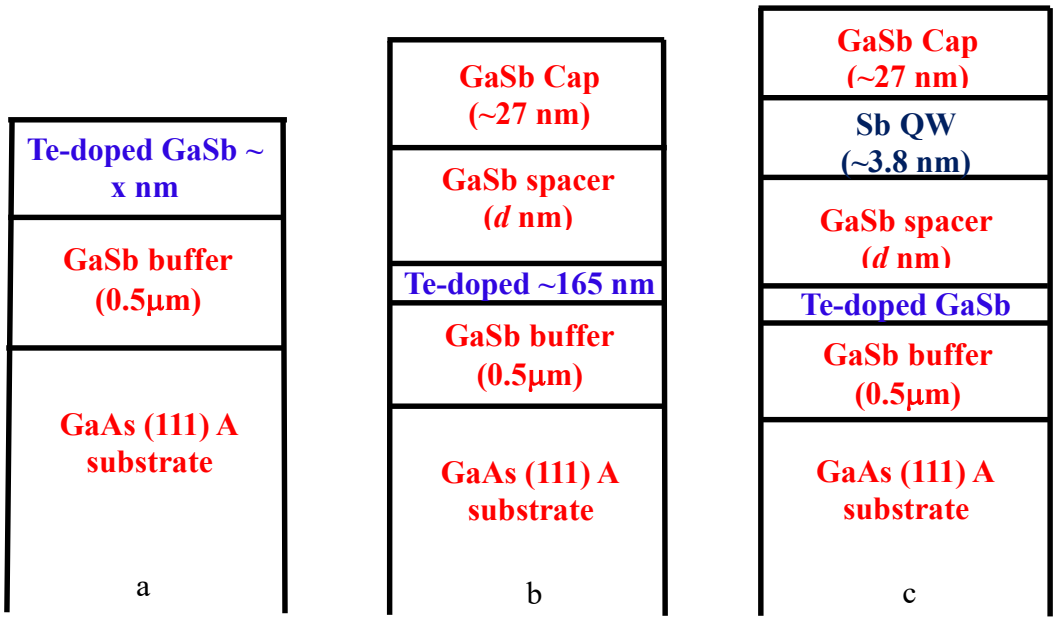

Figure 7.2. Layer sequence for the structures used for the study of remotely n-doped Sb QWs. (a) Structure used for Tellurium doping calibrations, (b) Comparison structure used for studying the GaSb spacer dependence. (c) Structure used for studying the electrical properties of the surface states of ultra-thin Sb layers.

7.1.1 Temperature dependence of the Hall Coefficient for Different GaSb Spacer Thicknesses

Figure 7.3 shows the temperature dependence of the Hall coefficient for remotely doped Sb QWs. We observe the following features in Figure A.

(a) For a given spacer, $1/R_H$ increases with decreasing temperature for structures with remotely doped Sb QW.

(b) As the spacer thickness is reduced, the change in $1/R_H$ is reduced and for 30 nm and 20 nm GaSb spacers, this change is very small.

(c) At room temperature, all the remotely-doped QW structures have the same value for $1/R_H$.

(d) For the doped structures with no Sb QW, $1/R_H$ has almost a constant value for the temperature range from 300K down to 20K.

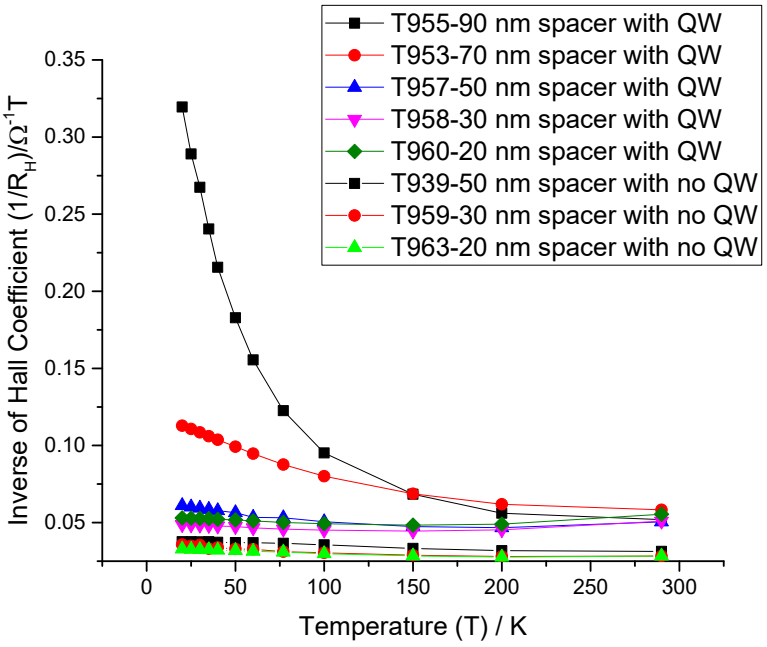

Figure 7.3. Temperature dependence of the Hall coefficient for remotely-doped Sb QW structures and uniformly-doped GaSb epilayers.

To explain the behavior of the curves, let's first recall the four types of carriers in an undoped Sb QW:

- n_1 = surface electrons (~20% contribution)
- p_1 = surface holes
- p_2 = Sb bulk holes
- n_2 = Sb bulk electrons (possibly negligible)

By doping, we expect the Fermi energy, E_F, to move to higher energy. Thus,

- n_1 significantly increases
- p_1 significantly decreases
- p_2 significantly decreases (important only at high T)
- n_2 increases (important only at high T)

Also, we assume that E_F moves into the bulk gap, so n_2 and p_2 (intrinsic carriers) are very temperature dependent. Table 7.1 shows the carriers which are important at different temperatures. For undoped Sb QWs, surface holes, bulk holes and surface electrons are important at all temperature. For doped Sb QWs, bulk holes and bulk electrons (intrinsic carriers) dominate at high temperature. Thus, at room temperature, all the doped Sb QWs have the same value for $1/R_H$. When the temperature is reduced, the Fermi energy moves up in energy because the intrinsic carrier concentrations are reduced; hence we can see the contribution of surface electrons and surface holes in the transport measurements at lower temperatures. A schematic band diagram explaining this process is shown in Figure 7.4. Thus, the four-carrier system in undoped Sb QW reduces to a two-carrier system at low temperature when doped.

The behavior of $1/R_H$ vs. temperature (Figure 7.3) can be explained using a multiple-carrier model with two types of electrons and two types of holes. For simplicity, we make the rough approximation that both types of holes have the same mobility and both types of electrons have the same mobility. This simplifies the model to two carrier types (equation 5.27). Figure 7.5 qualitatively maps the behavior of $1/R_H$ with different concentrations of electrons for a two carrier model. By comparing the shape of the curve with the experimental curves we obtained for doped Sb QWs (Figure 7.3), we conclude that the doped Sb QWs are in the transition regime of the two carrier system as highlighted in Figure 7.5. Also, the electron concentration in lightly-doped Sb QWs are strong functions of temperature. On the other hand, the Hall effect in the doped GaSb epilayers (structures with no Sb QW) can be explained using single carrier model.

QW type	Low T	Medium T	High T
Un-doped QW (E_F in VB)	p_1 p_2 n_1 n_2	p_1 p_2 n_1 n_2	p_1 p_2 n_1 n_2
Doped QW (E_F in gap)	n_1 p_1 n_2, p_2	n_1 n_2, p_2 p_1	n_2, p_2 n_1 p_1

Table 7.1. Important carriers at different temperatures in undoped Sb QWs and remotely doped Sb QWs. Important carriers are shown in bold.

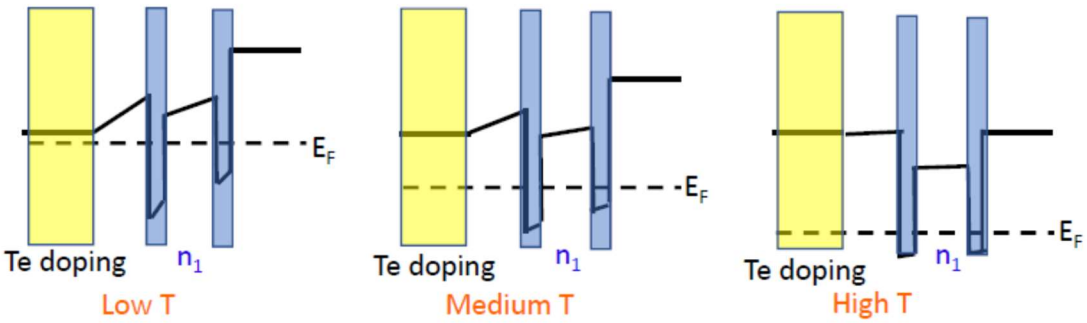

Figure 7.4. Fermi level in remotely doped Sb QW at different temperatures. The surfaces states are shown as two very thin QWs.

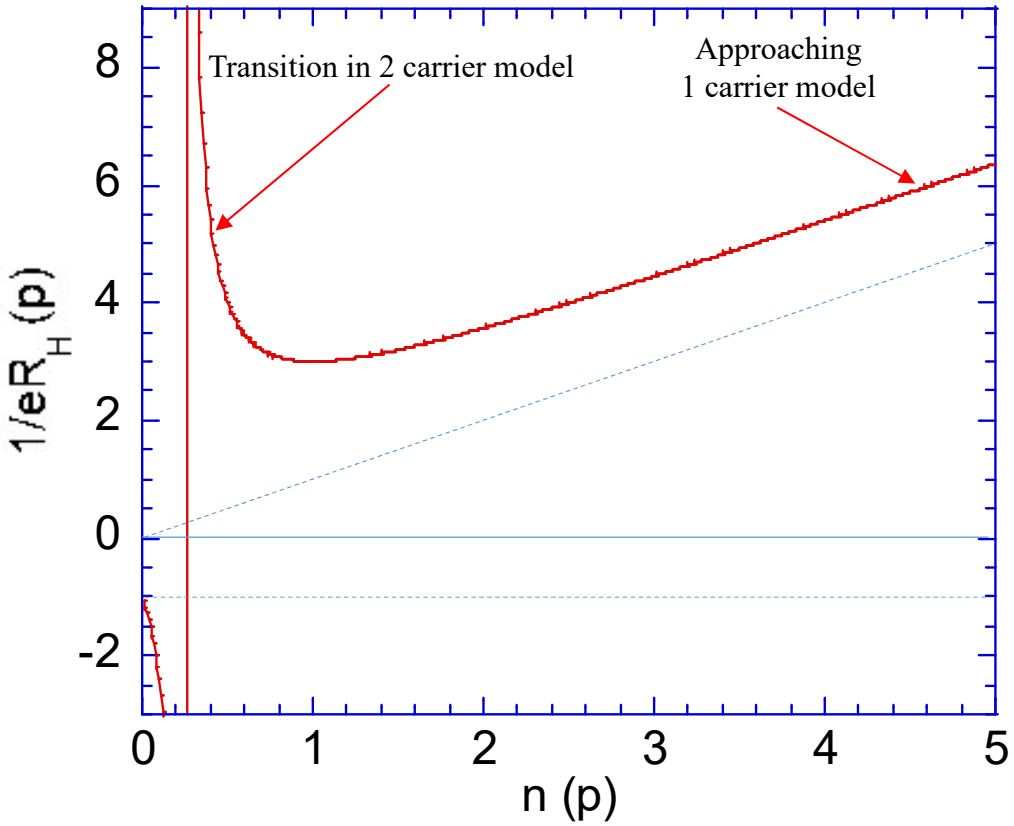

Figure 7.5. The Hall coefficient as a function of electron density in the two-carrier model given by the equation 5.27. For this plot, the hole density is independent of temperature and the electron mobility is twice the hole mobility.

7.1.2 GaSb Spacer Dependence of the Hall Coefficient at 20 K

The of Hall coefficient changes when the GaSb spacer thickness is reduced from 90 nm down to 20 nm as shown in Figure 7.6. The black line and red line show the spacer dependence of the Hall coefficient of the structures with the Sb QW and with no QW, respectively. For both structures, we observe a positive Hall coefficient which indicates that there are more electrons than holes in the system. There is a factor of 5 change in the Hall coefficient for the structures with the Sb QW whereas for the ones with no QW, there is only a ~ 17% change. This confirms that the change in the Hall coefficient is due to the Sb QW being populated as we reduce the GaSb spacer thickness. The change in the Hall coefficient as the spacer thickness is changed in the structures with no Sb QW may be due to surface depletion. For a thicker the spacer, fewer electrons are lost to surface depletion. Hence, we measure a higher density of electrons (smaller Hall coefficient) in the structures with a thicker spacer.

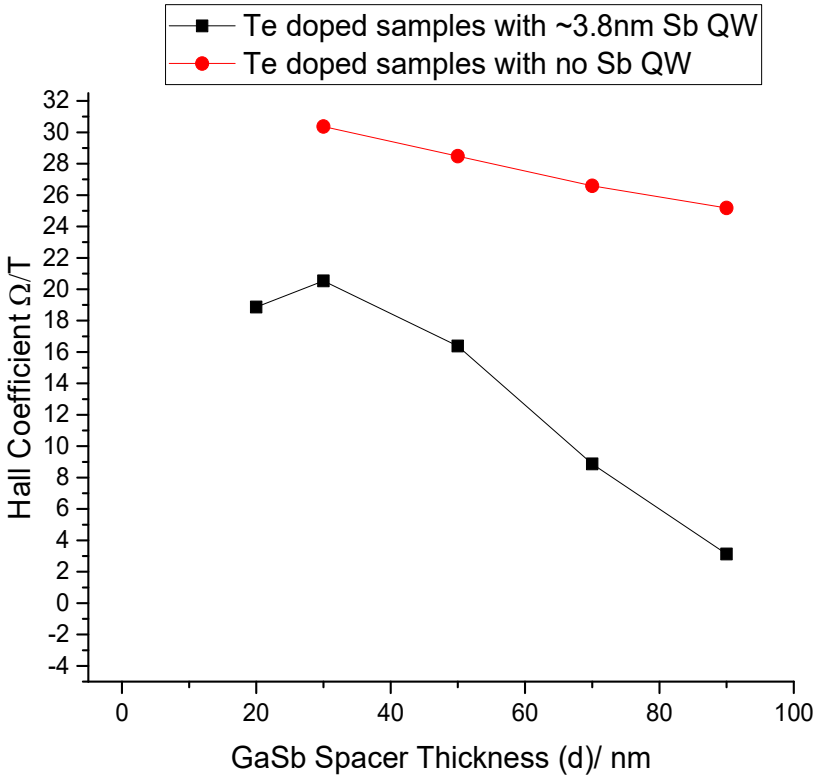

Figure 7.6. Plot of Hall coefficient versus GaSb spacer thickness. The measurements were made at 20 K and in a magnetic field of 0 – 0.15 T.

To explain the shape of the curves, increasing of the Hall coefficient as we increase the population of electrons in the QW and then decreasing below a GaSb spacer thickness of 30 nm. Recall for single carrier and two carriers, equation (5.15) and (5.27) in chapter 5;

$$R_H = \frac{1}{ne} \tag{5.15}$$

$$R_H = \frac{n\mu_n^2 - p\mu_p^2}{e(n\mu_n + p\mu_p)^2} \tag{5.27}$$

Here R_H is the Hall coefficient and n, p, μ_n, and μ_p are respectively 2D electron density 2D hole density, mobility of electrons, and mobility of holes.

Following our argument that only the electron surface states are populating not the bulk, if the concentration of the electrons is enough to dominate. Per equation (1), R_H should decrease as the thickness of the GaSb spacer is reduced. But we observe the opposite, R_H increasing as the GaSb spacer thickness is reduced from 90 nm to 30 nm. This implies that there is multiple carrier contribution to Hall resistance.

As the density of electrons in TI states increase, the density of holes in the TI states and the bulk states decrease due to an increase in E_F. Then the effect on R_H can be explained using equation (2). When the GaSb spacer is reduced from 90 nm to 30 nm, the percentage increment in the numerator of equation (2) is greater than the increment in the denominator, thus R_H increases. Yet it is not possible to state that contribution from the hole in the TI states and the bulk is negligible, but these observations confirms that the overall reduction in the percentage of holes in the system. Also, there can be parallel conduction through the doped layer via electron tunneling through the barriers.

For further analysis of the multiple carries in the system, we conducted resistivity and Hall measurement at very low temperature (<50 mK) and high magnetic fields up to 18 T at National High Magnetic Field Laboratory. Same piece of the samples that we used for low magnetic field measurements were used for high magnetic field measurements.

7.2 Remotely Doped Sb QWs in High Magnetic Fields

Due to the limited time available at the National High Magnetic Field Laboratory, we made high field magnetoresistance (MR) measurements, only for QW structures T960, T958, and T957 with a spacer thickness of 20 nm, 30 nm and 50 nm respectively (structure is shown in Figure 7.2c). For comparison, we also studied one structure with no Sb QW but with a GaSb spacer of 30 nm (T963, the structure is shown in the Figure 7.2.b) and a doping calibration sample (T965, the structure is shown in the Figure 7.2.a). Since T957 and T965 had one bad contact, we used only 3 contact points to collect data from these two samples. Further, there was a large contact resistance in T965.We were unable to observe any fine features in T957 and T965 and did not have enough time to remount the samples and recollect data. Because of that, detailed quantitative analysis was performed only for T958, T960 and T963.

Figure 7.7 shows the Hall resistance versus the magnetic field perpendicular to the sample surface, measured at a temperature < 50 m K. Hall voltage is not linear up to 18 T, confirming multiple carrier contributions. The Hall coefficient is slightly smaller for the structures with 20 nm GaSb spacer than the, 30 nm GaSb spacer.

The longitudinal resistivity (R_{xx}) as a function of magnetic field at different tilt angles is shown in Figure 7.8 for T958, T960 and T963. Tilt angle is measured from the surface of the sample; 0° tilt is parallel to the sample surface and 90° tilt is perpendicular to the sample surface. Measurements were made at a temperature <50 m K and in a magnetic field of 0 – 15 T.

Shubnikov-de Haas (SdH) oscillations in sample T963; no Sb QW:

Sample T963 shows very strong SdH oscillations in both perpendicular and tilted magnetic field. These oscillations do not move with tilted field implying that these are due to electrons in 3D which matches the design of the structure of T963; the n-doped layer is 165 nm thick. Table 7.2 shows the number of occupied Landau levels or filling factor υ for the oscillations observed with the corresponding magnetic field where minima occur. Recall equation 5.39 from chapter 5, We know that there are exactly n full Landau levels when υ = n, at a field $B_n = \frac{hn_{2D}}{en}$ where at B = B_n, the Fermi level (E_F) lies in the empty region between Landau levels hence the density of states at this point goes to zero. From the slope of the plot of n against $1/B_n$ shown in figure 7.9, we find the 2D electron density. The calculated 2D electron density with spin splitting is ~1.76×10^{12} cm^{-2}. Yet the oscillations are due to electrons in 3D, thus we calculate the electron density in the doped layer using equation (7.1) and the value is ~1.24×10^{18} cm^{-3} for 165 nm thick doping layer. The mobility of the electrons found to be ~ 4700 – 5000 cm^2/V s as expected for a slightly higher electron density in a system.

$$n_{3D} = \frac{2}{3}\sqrt{\frac{2}{\pi}}n_{2D}^{\frac{3}{2}} \tag{7.1}$$

Unlike for the undoped Sb QWs (a representative plot of a Hall resistance versus magnetic field is shown in appendix Figure 7.7, oscillations observed for these doped structures will be used to further analyze the carrier concentration.

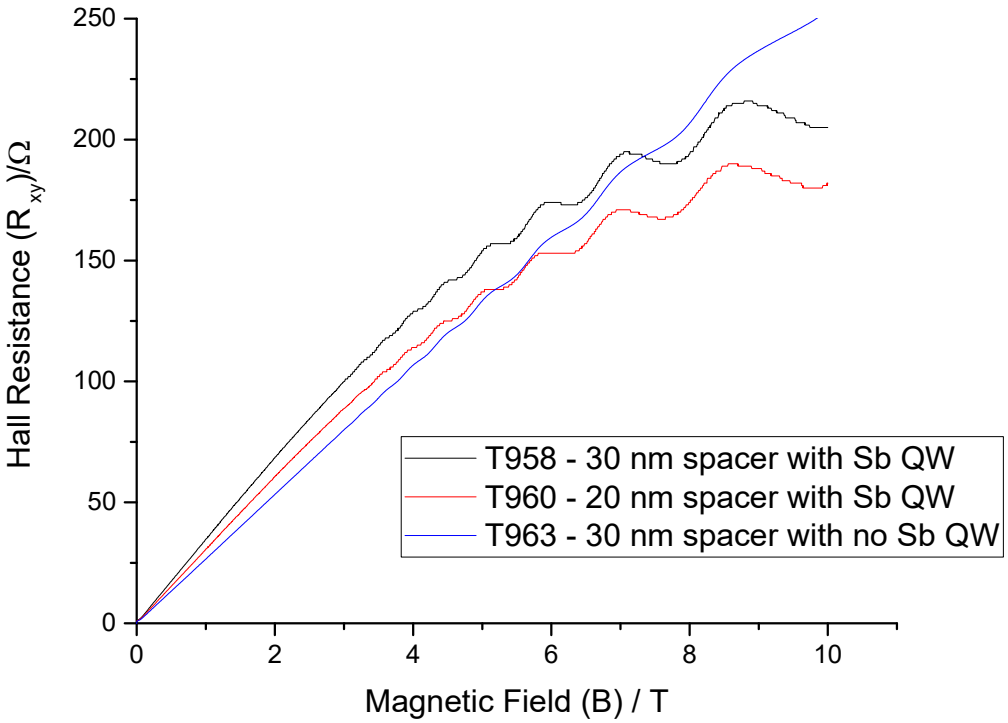

Figure 7.7. Plot of Hall resistance versus the magnetic field normal to the surface of the QW structures with the smallest GaSb spacer layers, 30 nm and 20 nm. Measurements were taken at temperatures < 50 m K.

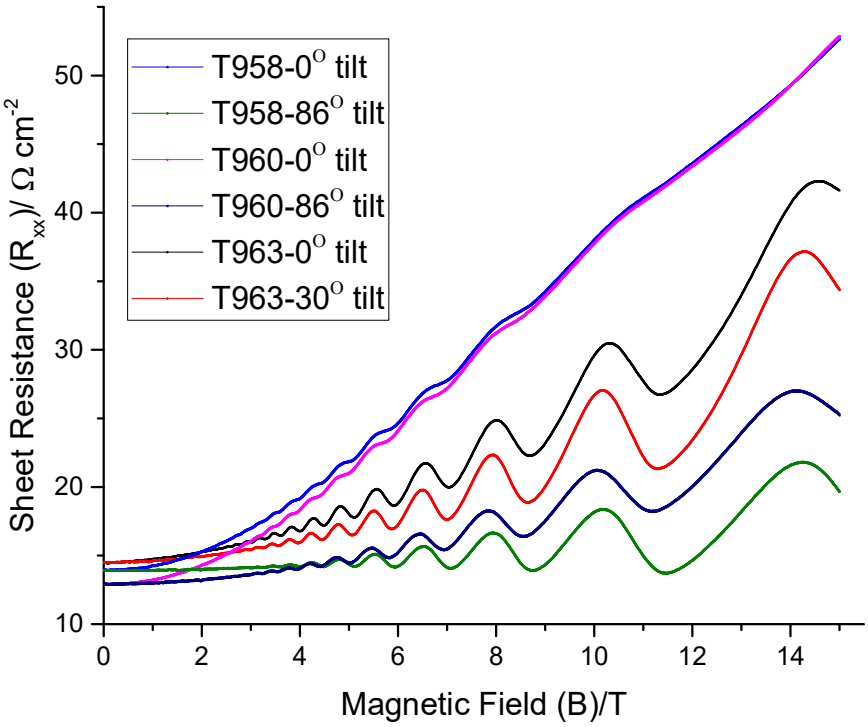

Figure 7.8. Longitudinal resistivity (R_{xx}) as a function of magnetic field at different tilts.Measurements were made at a temperature <50 m K and in a magnetic field of 0 – 15 T. The samples T958 and T960 have 3.8 nm thick Sb QW with 30 nm GaSb spacer and 20 nm GaSb spacer respectively (structure is shown in Figure 7.2.c). T963 has no Sb QW and the structure is shown in Figure 7.2.b)

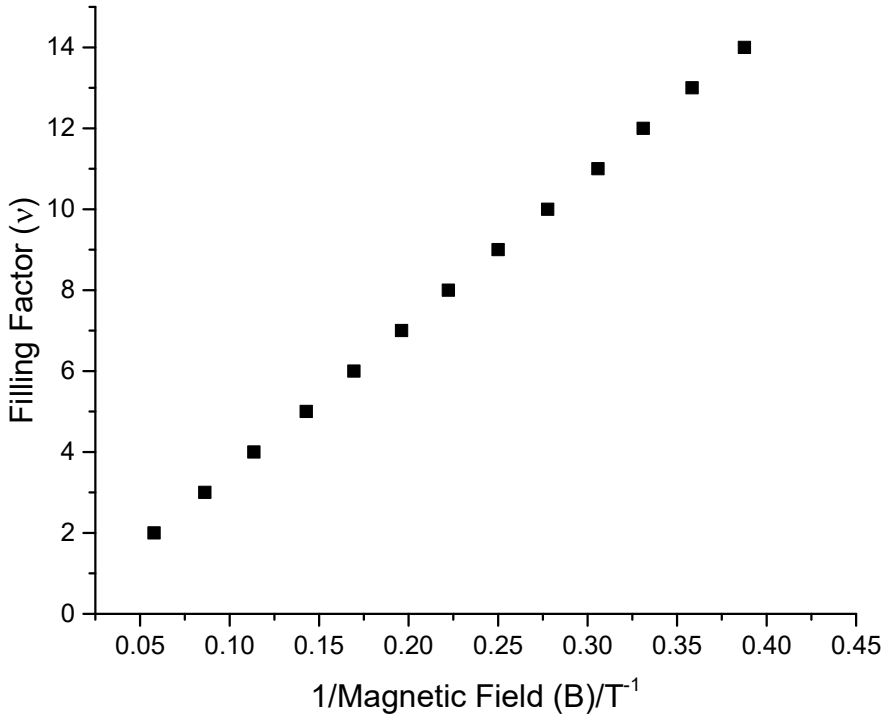

Figure 7.9. Plot of filling factor (υ=n) against $1/B_n$, where B_n is the magnetic field where the minima of the Shubnikov-de Haas (SdH) oscillations occurred for the sample with no Sb QW. Measurements were made at a temperature <50 m K and in a magnetic field of 0 – 18 T. Calculated 3D electron density considering spin splitting is1.24×18 cm^{-3}.

B (T)	17.4	11.6	8.7	7.0	5.8	5.0	4.4	3.9	3.5	3.2	2.9	2.7	2.5
υ	2	3	4	5	6	7	8	9	10	11	12	13	14

Table 7.2. Corresponding values of the integer filling factor (υ = n) versus the magnetic field (B/T) at which the minima of the SdH oscillations occur. The plot shown in Figure 7.9 is calculated using the values given in this table. All values of the magnetic field are round off to first decimal place. The plot from which the values of the minima are taken is given in the Appendix A7.

Shubnikov-de Haas (SdH) oscillations in sample T958; 3.8 nm thick Sb QW:

Samples T958 and T960 also show SdH oscillations but a large background dominates the raw signal. Therefore, we subtract a parabolic background to better study the oscillations. The background fit for these curves are shown in the appendix. Figure 7.7 shows SdH oscillations of samples T958 and T963 (no Sb QW) after removing the background. The amplitude (ΔR_{xx}) of the oscillations in T963 is reduced by a factor of 2 to fit in the intensity scale of T958. For the magnetic field perpendicular to the surface, we can see that minima and maxima of T958 coincide with T963 in the magnetic field regime of 0 – 9 T.

Positions of maxima and minima of the oscillations of T958 and T960 in the tilted magnetic field also coincide with the oscillations of T963 in the full magnetic field regime, 0-18 T as shown in the appendix Figure C5. This implies that the origin of the oscillations in the tilted field for T958 and T960 is due to 3D carriers; parallel conduction through the doped layer exists. The electrical contacts are not annealed, and as we have seen from the previous experiments, the indium does not make direct contact with any layer below Sb QW. Thus, the parallel conduction through the doped layer is possible only through tunneling mechanism which would occur for a thin spacer layer.

As we can see from Figure 7.10, for a magnetic field above 9 T which is perpendicular to the surface, maxima and minima of T958 and T960 start deviating from the positions of T963. Moreover, for T963 there is a minimum at B = 11.6 T whereas for T958 there is no minimum at B = 11.6 T for the perpendicular magnetic field. In the tilted field, however, minima of all three samples occur at B = 11.6 T. This

implies a possibility of a second series of SdH oscillations due to carriers confined in 2D, with oscillations that overlap with those due to the carriers in the doping layer. To fit a second series of Landau levels for the oscillations, we need to see fine features better. Hence we divided the oscillations into three regimes, 0 - 3.5 T, 3.5 – 8 T and 8 – 15 T, and subtracted the best background fit for each range. The best background fits for each range were different than the best fit for the full range, 0-18 T.

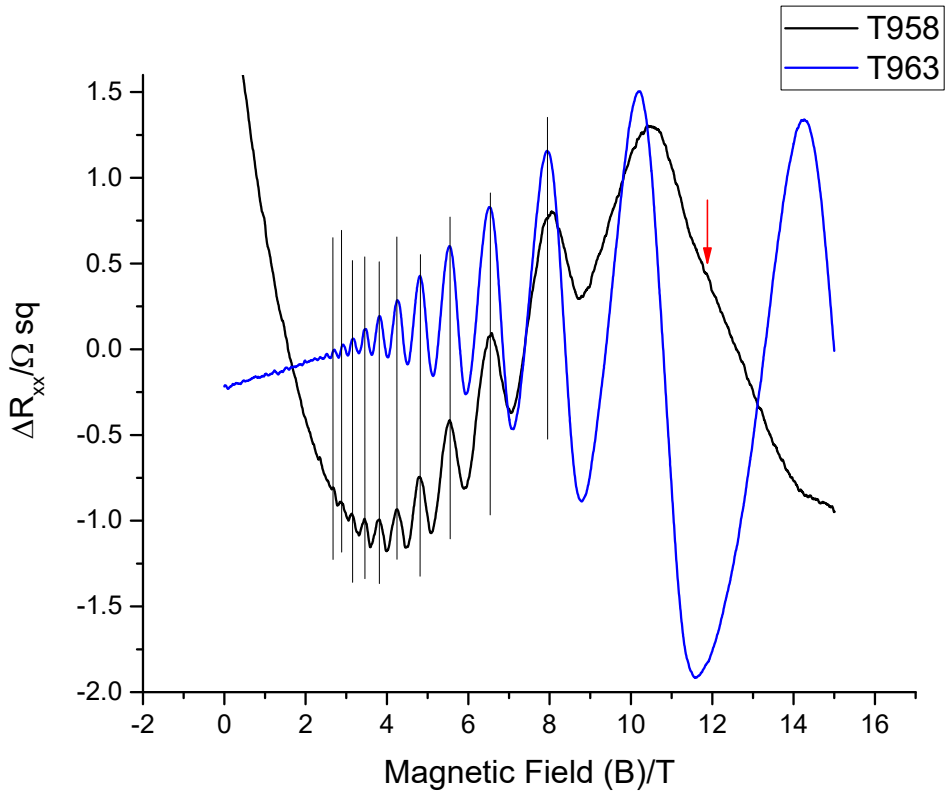

Figure 7.10. The Shubnikov-de Haas (SdH) oscillations occur on a large background. To better study the features, a parabolic background is subtracted. Since the SdH oscillations of T963 is stronger than those of T958, the intensity (ΔR_{xx}) of T963 was reduced by a factor of 2. Measurements were made at a temperature of <50 mK and in an applied magnetic field perpendicular to the sample surface with a field strength of 0 – 18 T.

Figure 7.11 shows SdH oscillations for T958, T960 and T963 in a magnetic field of 0 – 3.5 T applied perpendicular to the surface. The plot shown here is after removing a parabolic background. Oscillations of T958 and T960 coincide with T963 (no Sb QW). Oscillations start appearing between 2.2 - 2.5 T for all three samples which implies that the mobility of the carriers responsible for the oscillations in this regime is ~ 4500 – 5000 cm^2 / V s. This further confirms that the origin of the oscillation in this magnetic field regime for all three structures is due to the carriers remaining in the 165 nm thick Te doped GaSb layer. There are no features we could observe due to carriers confined in a 2D layer in this magnetic field regime.

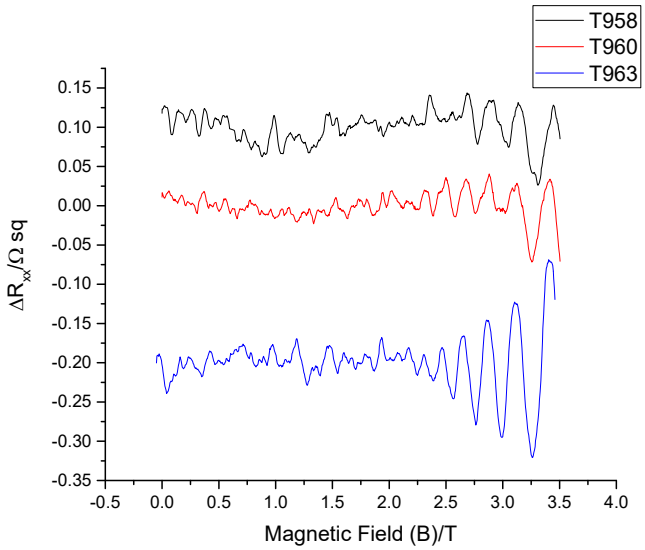

Figure 7.11. The Shubnikov-de Haas (SdH) oscillations occur on a large background that dominate the raw signal. To enhance the fine features, a parabolic background is subtracted in a magnetic field < 3.5T. Measurements were made at a temperature of <50 mK and in an applied magnetic field perpendicular to the sample surface. The curves of T958, T960 and T963 are shifted along the y axis by +0.1Ω, 0Ω and -0.2 Ω, respectively, to avoid overlapping.

In the magnetic field range of 3.5 – 8 T, for samples T958 and T960, shoulder-like features are observed at ~ 6.2 T and 7.8 T in Figure 7.12 (a). These features are not observed in the oscillations of the parallel field (see Figure 7.12 (b)) for these two samples or for T963 (see Figure 7.12 (a)). Since these features are of the order of the noise, we cannot be certain that they are due to 2D carriers in the Sb QW. Further, Figure 7.13 shows the oscillations in the regime 8 – 15 T and this has a missing minimum at ~ 11.6 T compared to T963; it has a minimum at ~ 13.8 T instead. But the oscillations in the parallel field for both samples have minima coinciding with T963. This could be either an indication of a second Landau series due to carriers confined to 2D or an artifact due to the very large parabolic background.

The carriers confined in 2D may generate some minima at the same positions as the carriers in 3D and some additional minima and maxima at some other positions which may not be clearly observed due to the intense oscillations generated by the large number of excess carriers in the doped layer below the Sb QW. Nevertheless, if we assume the shoulder like features are real and combine these with minima that we observe, we found a well-fitting Landau series for 2D carriers with a different density. The new Landau series predicted for 2D carriers are shown in Table 7.3. Using these values, the 2D carrier concentration is calculated to be ~3.3×10^{12} cm^{-2}. Since the fine features start appearing at ~ 6 T, the mobility of these carries should be ~ 1600 cm^2/V s. Using the band structure for the undoped Sb TI states, we calculated that the electron density is $(2 – 5)\times10^{12}$ cm^{-2} and the mobility of the electrons is ~ (800-2000) cm^2/V s in the surface states at the Dirac point [51]. By comparing with the theoretically predicted

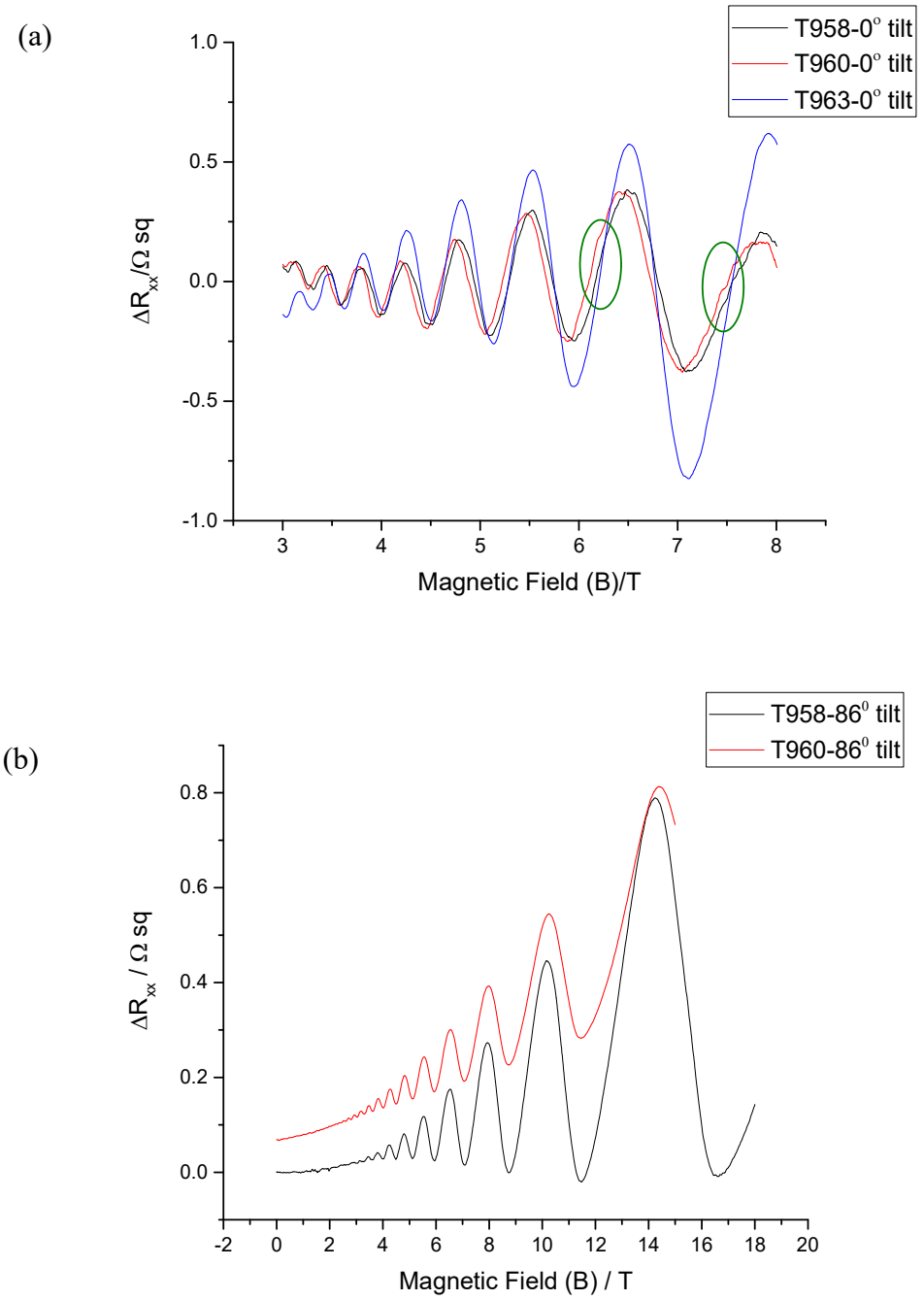

Figure 7.12. The Shubnikov-de Haas (SdH) oscillations occur on a large background that dominate the raw signal. To enhance the fine features in the magnetic field range 3 – 8 T, a parabolic background is subtracted. (a) Oscillations in the perpendicular magnetic field show shoulder like features (circled in green). The amplitude of oscillations in T963 is reduced by a factor of 16 (b) Oscillations in tilted field show no shoulder like features. The amplitudes of oscillations in T958 and T960 in tilted field are reduced by a factor of 10 and 20, respectively. Measurements were made at a temperature of <50 mK.

value we suggest that these 2D carriers are the electrons in the surface states of the Sb QW.

The longitudinal resistance (R_{xx}) of the undoped Sb QW shows a linear dependence on magnetic field above ~2 T (shown in the appendix Figure C2). None of the fine features that we have discussed above were observed in undoped QWs. In section 7.1, since we confirmed that the Sb QW is populated by remote doping, the electron density of the surface states of undoped QWs should be $< 3.3\times10^{12}$ cm^{-2}, less than the value we predicted in this section. If we consider the theoretically predicted electron carrier density (2×10^{12} cm^{-2}) for the undoped Sb QW is the initially available amount in the QW [51], we have populated the surface states with an additional electron concentration of ~ 1.3×10^{12} cm^{-2} by remote doping. This would be the maximum allowable electron concentration that can be added via remote doping because there is an electron density of 1.24×10^{18} cm^{-3} still available in the underlying GaSb epilayer. Thus, we have not transferred all electrons in the doping layer.

To confirm that these fine features are true SdH oscillations due to carriers confined in the 2D layer, we need to reduce the Te doping concentration at least by a factor of 10. New structures were grown with a Te doping concentration of ~2.2×10^{12} cm^{-2}. We need to perform high field MR measurements on these structure for confirmation of our interpretation.

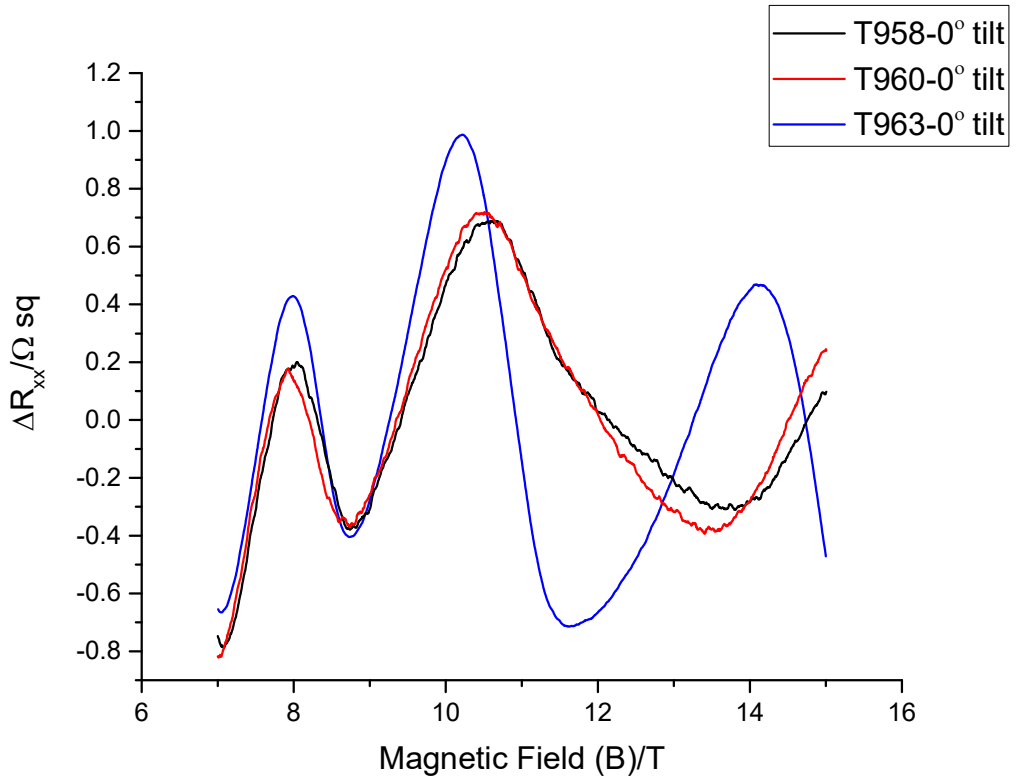

Figure 7.13. The Shubnikov-de Haas (SdH) oscillations occur on a large background that dominate the raw signal. To better study the features in the magnetic field range from 7 – 18 T, a parabolic background that is different from the background at < 8 T is subtracted. Measurements were made at a temperature <50 m K and in an applied magnetic field perpendicular to the sample. Since the SdH oscillations of sample T963 are stronger than those of T958 and T960, the intensity (ΔR_{xx}) of T963 is reduced by a factor of 4 when added to the same graph.

B (T)	17.4	13.9	11.6	9.9	8.7	7.7	7.0	6.3	5.8	5.4	5.0
$\upsilon = n$	4	5	6	7	8	9	10	11	12	13	14

Table 7.3. Predicted values for a second oscillation which could be responsible for the missing peak in the magnetic field range of 8-15 T. All values of the magnetic field are rounded off to the first decimal place.

7.3 Summary

Remote n-doping of Sb QWs was confirmed by analyzing the spacer dependence of the Hall coefficients in a low magnetic field of 0 – 0.15 T and a temperature of 20 K. Further, using high field magnetoresistance (MR) measurements, we deduced that Sb surface states have an electron concentration of ~3.3×10^{12} cm^{-2} with a mobility of ~ 1600 – 2000 cm^2/ V s. If the initial electron concentration, before doping the Sb QW, is 2×10^{12} cm^{-2} (lowest possible value predicted by the theory [51]) we calculated the maximum amount that is transferred to the QW is ~ 1.3×10^{12} cm^{-2}. By remotely n-doping the Sb QWs, we observed n-type Hall conductivity. Therefore, by doping we could decrease the hole contribution from the bulk states and enhance the conductivity due to surface states.

A parallel conduction path generates strong SdH oscillations in R_{xx} measurements, which dominate over the fine features that may be due to electrons confined in 2D. The Te doping should be reduced to eliminate the parallel path. Taking the predicted value into account, we reduced the thickness of the doping layer for the new structures by 10×. We need to conduct high-field transport measurements on these structures to verify our interpretation and make a precise conclusion.

Chapter 8: Conclusions and Future Work

8.0 Conclusions

In this dissertation, we discussed the growth and characterization of Sb QW structures for a potential application as a topological insulator (TI). We successfully developed a non-conventional method to grow ultra-thin Sb layers with control over thickness down to a few angstroms. We observed good crystalline quality with an Sb surface roughness (root mean square roughness) of ~ 0.45 nm for the structures grown on GaSb (111)A wafers bought from WaferTech. On the other hand, the structures grown on Galaxy wafers had a higher surface roughness of ~1.1 nm due to an inability to completely thermally removing the oxide layer from the substrate wafers.

We studied the electrical properties of undoped ultra-thin Sb QWs in the thickness range of 1 to 6 nm. The contribution of the surface states to the total conduction was deduced from the dependence of the low-temperature conductivity as a function of thickness. We found that for a thickness approaching zero, there would be a non-zero conductivity for the ultra-thin Sb film, which is attributed to the surface states. We deduced that the surface contribution for the total conduction of a 3.8 nm thick Sb film is approximately 20%. Thus, we were successful in suppressing the bulk conduction via quantum confinement, yet unable to completely remove the bulk contribution.

In a further attempt to increase the surface electron carrier density, we remotely n-doped the Sb QW by doping the underlying GaSb barrier layer using Te atoms. We confirmed successful remote n-doping of the Sb QWs by analyzing the spacer dependence of the Hall coefficients in a low magnetic field of 0 – 0.15 T and a

temperature of 20 K. Further, the MR measurements done in high magnetic field (from 0-18 T) showed tilt-independent SdH oscillations that were very strong. These oscillations dominated over the fine features that may be due to electrons confined in 2D. The tilted field studies confirmed that there are many carriers remaining in the doped GaSb epilayer. Therefore, we could not find evidence of the concentration of electrons in the surface states.

8.1 Future Work

To obtain a smooth Sb layer, we suggest performing HF etching of the substrates before growth, which will facilitate oxide removal. This will help to grow very smooth GaSb epilayers on which we can grow atomically flat Sb layers reliably.

For transport studies of the surface states, we need to reduce the doping in the GaSb epilayer such that all the dopant electrons are transferred into the Sb QW. This will enable us to observe SdH oscillations due to the electrons in the surface states. Further, we can increase the barrier height by changing the barrier material to $Al_xGa_{1-x}Sb$ so that more electrons are transferred into the QW.

We can also change the Fermi level by gating the QW. Fabrication procedures should be developed to achieve this goal.

References

1. *Scientific Background on the Nobel Prize in Physics 2016, Topological Phase Transition and Topological Phases of Matter* 2016; Available from: https://www.nobelprize.org/nobel_prizes/physics/laureates/2016/advanced-physicsprize2016.pdf.

2. Hasan, M.Z. and C.L. Kane, *Colloquium.* Reviews of Modern Physics, 2010. **82**(4): p. 3045-3067.

3. König, M., et al., *Quantum Spin Hall Insulator State in HgTe Quantum Wells.* Science, 2007. **318**(5851): p. 766-770.

4. Hsieh, D., et al., *Observation of Unconventional Quantum Spin Textures in Topological Insulators.* Science, 2009. **323**(5916): p. 919-922.

5. Zhang, P., et al., *Topological and electronic transitions in a Sb(111) nanofilm: The interplay between quantum confinement and surface effect.* Physical Review B, 2012. **85**(20): p. 201410.

6. Nakahara, M., *Geometry, Topology and Physics.* 1990.

7. Hasan, M.Z. and C.L. Kane, *Colloquium: Topological Insulators.* Reviews of Modern Physics, 2010. **82**(4): p. 3045-3067.

8. Tsui, D.C., H.L. Stormer, and A.C. Gossard, *Two-Dimensional Magnetotransport in the Extreme Quantum Limit.* Physical Review Letters, 1982. **48**(22): p. 1559-1562.

9. Thouless, D.J., et al., *Quantized Hall Conductance in a Two-Dimensional Periodic Potential.* Physical Review Letters, 1982. **49**(6): p. 405-408.

10. Haldane, F.D.M., *Model for a Quantum Hall Effect without Landau Levels: Condensed-Matter Realization of the "Parity Anomaly".* Physical Review Letters, 1988. **61**(18): p. 2015-2018.

11. Kane, C.L. and E.J. Mele, *Quantum Spin Hall Effect in Graphene.* Physical Review Letters, 2005. **95**(22): p. 226801.

12. Fu, L., C.L. Kane, and E.J. Mele, *Topological Insulators in Three Dimensions.* Physical Review Letters, 2007. **98**(10): p. 106803.

13. Fu, L. and C.L. Kane, *Topological insulators with inversion symmetry.* Physical Review B, 2007. **76**.

14. Hsieh, D., et al., *A topological Dirac insulator in a quantum spin Hall phase.* Nature, 2008. **452**(7190): p. 970-974.

15. Chen, Y.L., et al., *Experimental Realization of a Three-Dimensional Topological Insulator, Bi_2Te_3.* Science, 2009. **325**(5937): p. 178-181.

16. Desheng Kong, Y.C.e.a., *Ambipolar field effect inthe ternary topological insulator($Bi_xSb_{1-x})_2Te_3$ by composition tuning.* Nature Nanotechnology, 2011. **6**: p. 705-709.

17. Bian, G., et al., *Interfacial Protection of Topological Surface States in Ultrathin Sb Films.* Physical Review Letters, 2012. **108**(17): p. 176401.

18. D. Hsieh, D.Q., L. Wray, Y. Xia, Y. S. Hor, R. J. Cava , M. Z. Hasan, *A topological Dirac insulator in a quantum spin Hall phase.* Nature, 2008. **452**.

19. *Schematic of MBE chamber*. Available from: http://web.tiscali.it/decartes/phd_html/III-Vms-mbe.png.

20. Ledentsov, N.N., *Growth Processes and Surface Phase Equilibria in Molecular Beam Epitaxy.* 1999. **156**.

21. Foxon, J.O.a.T., *Molecular Beam Epitaxy, a Short History*. 1 ed. 2015: Oxford University Press.

22. Cohen, A.I.a.P.I., *Reflection High Energy Electron Diffraction*. 2004: Cambridge University Press.

23. *Reflection High Energy Electron Diffraction*. Available from: http://eng.thesaurus.rusnano.com/wiki/article799.

24. Lee, J.W., et al., *Advanced study of various characteristics found in RHEED patterns during the growth of InAs quantum dots on GaAs (0 0 1) substrate by molecular beam epitaxy.* Applied Surface Science, 2004. **228**(1–4): p. 306-312.

25. Hernández-Calderón, I. and H. Höchst, *New method for the analysis of reflection high-energy electron diffraction:α-Sn(001) and InSb(001) surfaces.* Physical Review B, 1983. **27**(8): p. 4961-4965.

26. Wikipeia, *Reflection high-energy electron diffraction.*

27. Ewald, P., *Introduction to the dynamical theory of X-ray diffraction.* Acta Crystallographica Section A, 1969. **25**(1): p. 103-108.

28. Srivastava, G.P., *Theory of semiconductor surface reconstruction.* Reports on Progress in Physics, 1997. **60**(5): p. 561.

29. Proessdorf, A., et al., *Analysis of GaSb and AlSb reconstructions on GaSb(111) A and B oriented surfaces by azimuthal-scan reflection high-energy electron diffraction.* Physical Review B, 2011. **83**(15): p. 155317.

30. *Laboratory for Advanced Semiconductor Epitaxy, University of Texas at Austin*. Available from: http://lase.ece.utexas.edu/mbe.php.

31. *Field Emission Electron Microscopy (FESEM) by Photometrics,Inc.*; Available from: http://photometrics.net/field-emission-scanning-electron-microscopy-fesem/.

32. Joseph Goldstein, D.N., David Joy, Charles Lyman, Patrick Echlin, Eric Lifshin, Linda Sawyer, and Joseph Michael *Scannig Electron Microscopy and X-Ray Microanalysis*. 3 ed. 2007: Springer Science+Business Media, LLC.

33. Mitani, K.S.a.T., *New Horizon of Applied Scanning Electron Micreoscopy*. Springer Series in Surface Sciences 45. 2009: Springer.

34. Leng, Y., *Materials Characterization: Introduction to Microscopic and Spectroscopic Methods*. 2 ed. 2013: Wiley-VCH.

35. Russell, J.J.B.a.L.D., *Electron Microscopy: Principles and Techniques for Biologists*. 2 ed. 1999: Jones and Bartlett.

36. *GEMINISEM Family*. Available from: https://www.zeiss.com/microscopy/us/products/scanning-electron-microscopes/geminisem.html.

37. Larson, D.P., *SEM Class Notes of Ziess Neon 40 EsB*.

38. *Atomic Force Microscopy*. Available from: https://en.wikipedia.org/wiki/Atomic-force_microscopy.

39. *Asylum Research Procedural Operation 'Manualette'*.

40. *MFP-3D™ Atomic Force Microscope Proprietary Specifications*.

41. *Atomic Force Microscopy-SPM User Guide*. Available from: http://www.nanophys.kth.se/nanophys/facilities/nfl/afm/icon/bruker-help/Content/SPM%20Training%20Guide.

42. Gaspe, C.K., et al., *Epitaxial growth of elemental Sb quantum wells.* Journal of Vacuum Science & Technology B, Nanotechnology and Microelectronics: Materials, Processing, Measurement, and Phenomena, 2013. **31**(3): p. 03C129.

43. Mishima, D.T. 2016.

44. Kittel, C., *Introduction to Solid State Physics*. 7 ed.: John Wiley & Sons, Inc.

45. Pauw, L.J.v.d., *A method of Measuring Specific Resistivity and Hall Effects of Discs of Arbitrary Shape* Philips Research Reports, 1958. **13**: p. 1-9.

46. *NIST Physical measurement laboratory, Engineering physics division*. Available from: https://www.nist.gov/pml/engineering-physics-division/hall-effect.

47. Yoshioka, D., *The Quantum Hall Effect*. Solid State Sciences. 2002: Springer-Verlag Berlin Heidelberg

48. Davies, J.H., *The Physics of Low Dimensional Semiconductors, An Introduction*. 2006: Cambridge University Press.

49. Janssen, T.J.B.M., et al., *Quantum resistance metrology using graphene.* Reports on Progress in Physics, 2013. **76**(10): p. 104501.

50. Pang, F., et al., *Origin of the metallic to insulating transition of an epitaxial Bi(111) film grown on Si(111).* Chinese Physics B, 2010. **19**(8): p. 087201.

51. Cairns, S., et al., *Observation of surface-state transport in ultrathin Sb.* Physical Review B, 2015. **91**(20): p. 205317.

52. Takayama, A., et al., *Rashba effect in antimony and bismuth studied by spin-resolved ARPES.* New Journal of Physics, 2014. **16**(5): p. 055004.

53. Ketterson, J. and Y. Eckstein, *de Haas-Shubnikov Effect in Antimony.* Physical Review, 1963. **132**(5): p. 1885-1891.

54. Öktu, O. and G.A. Saunders, *Galvanomagnetic properties of single-crystal antimony between 77 °K and 273 °K.* Proceedings of the Physical Society, 1967. **91**(1): p. 156.

55. Rao, G.N., et al., *Galvanomagnetic Effects in Antimony at Liquid-Helium Temperatures.* Physical Review, 1964. **133**(1A): p. A141-A152.

56. Rose, J. and R. Schuchardt, *A Pseudopotential Band Structure Calculation of Bismuth, Antimony, and Their Alloys.* physica status solidi (b), 1987. **139**(2): p. 499-518.

Appendix A: FESEM Images of GaSb (111)A Substrate

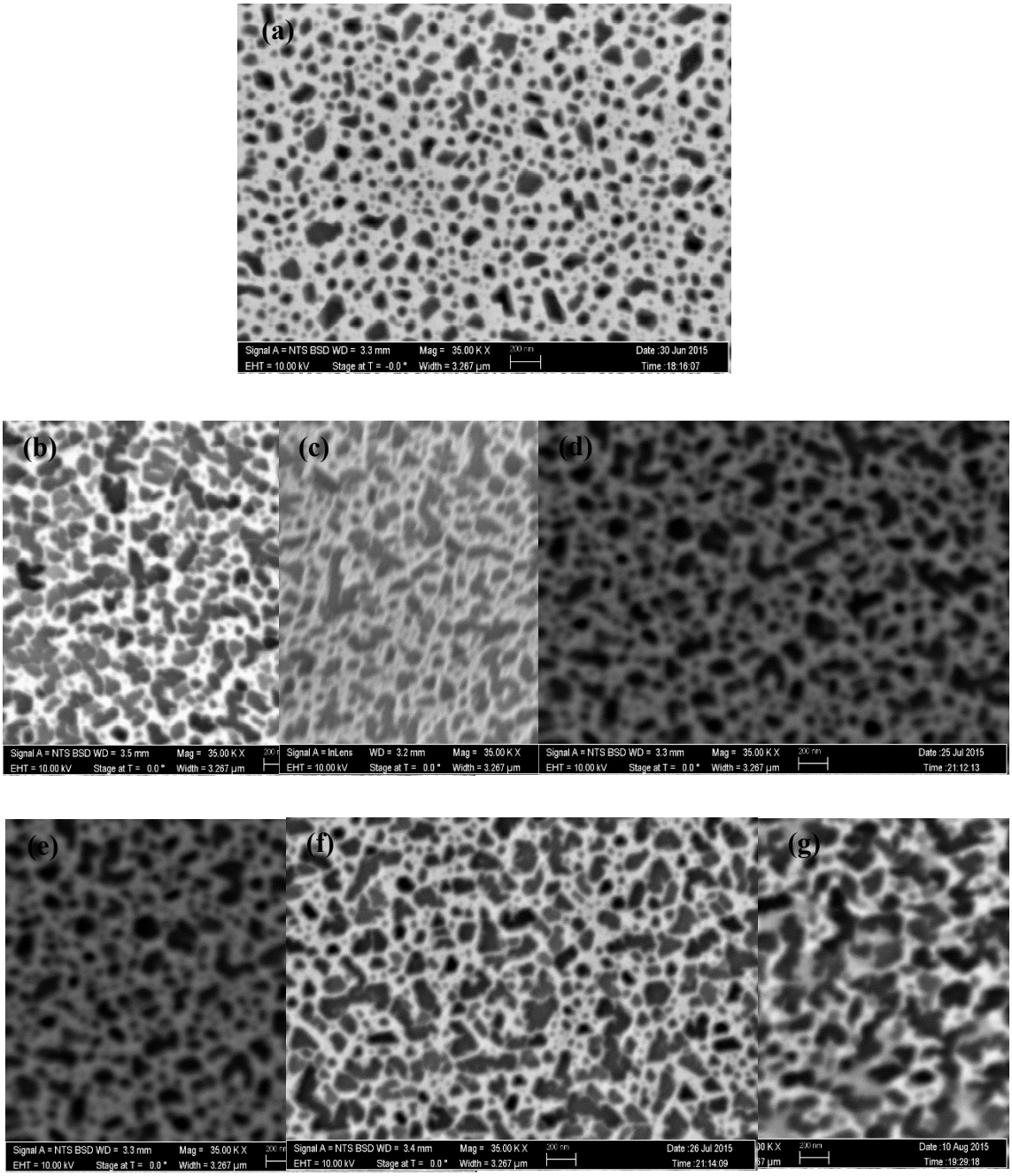

Figure A 1. Oxide desorption of GaSb (111)A substrate from Galaxy. FESEM image taken after annealing the substrate with Sb over pressure (a) at 610 °C for 10 minutes and at 620 °C for 10 minutes (normal oxide desorption procedure), (b) at 640 °C for 1 hour, (c) at 640 °C for 2 hours, (d), (e) at 640 °C for 3 hours, (f) at 650 °C for 3 hours, and (g) at 660 °C for 3 hrs, GaSb surface started melting. Oxide was not desorbed by annealing.

Appendix B: Figures Related to Chapter 6

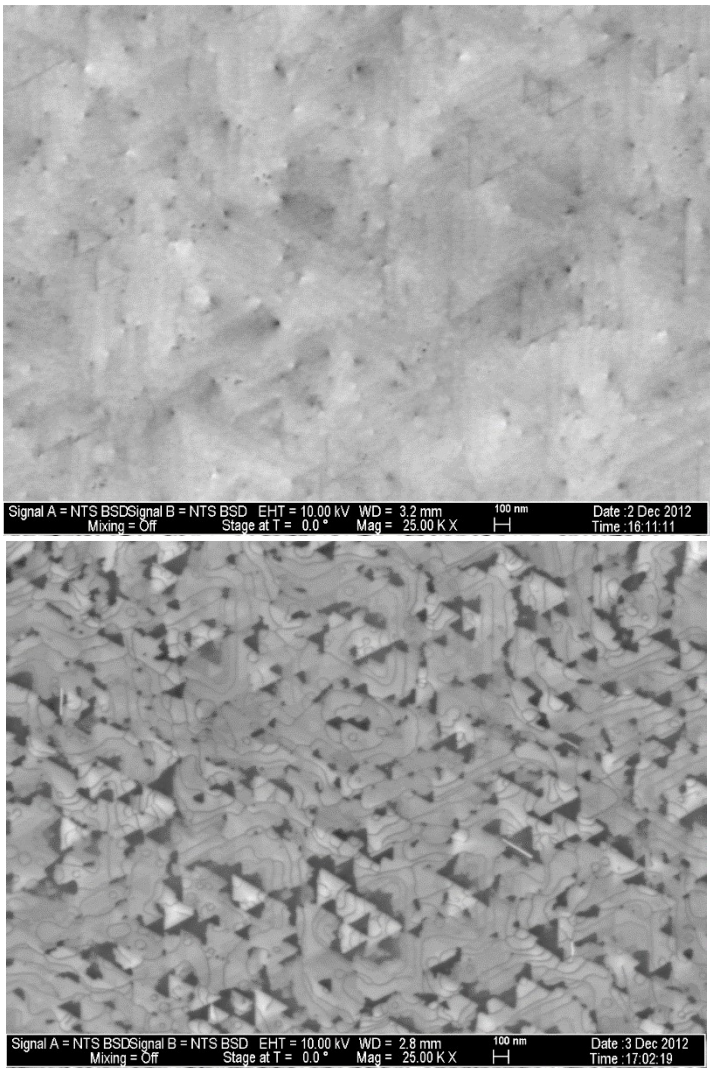

Figure B 1. Representative plan view FESEM images of all samples shown in Figure 5.1. (a) 1.5 nm thick Sb layer with a GaSb cap layer thickness of ~9 nm. This images shows fully covered Sb layer with GaSb cap layer. (b) 1.5 nm thick Sb layer with no GaSb cap layer. Quantitative analysis of this image shows a coverage of 96% of Sb layer.

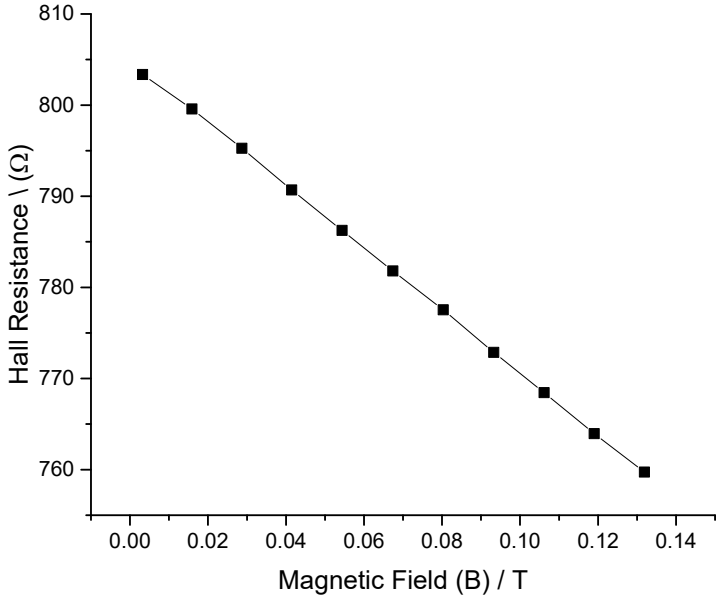

Figure B 2. Hall resistance versus Magnetic field for 500 nm thick GaSb epilayer (T720) grown on n- doped GaSb (111)A Galaxy substrate. Measurements are taken at 20 K. This has a negative Hall coefficient of ~ 300 Ω/T implying that the carriers are p-type.

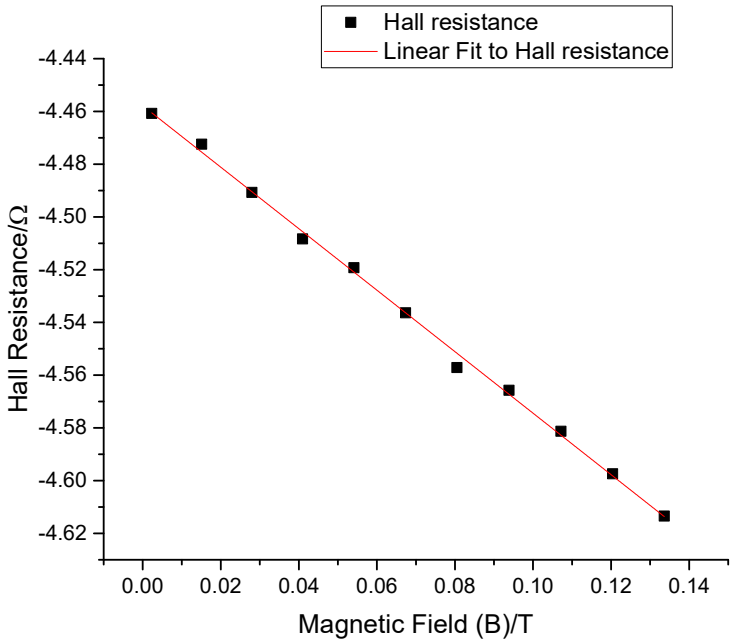

Figure B 3. Hall resistance versus Magnetic field for the capped Sb with film thickness of 3.8 nm. Measurements taken at 20 K

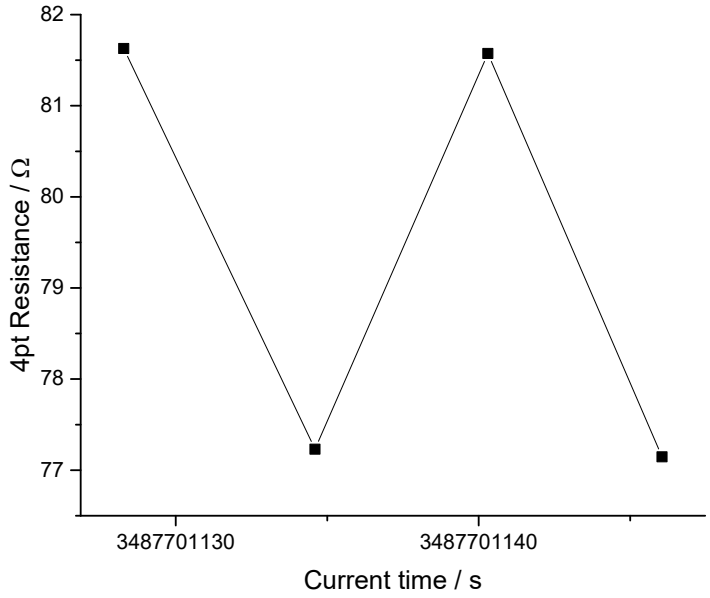

Figure B 4. 4pt resistance at zero magnetic field measured at 20 K for the capped Sb with film thickness of 3.8 nm

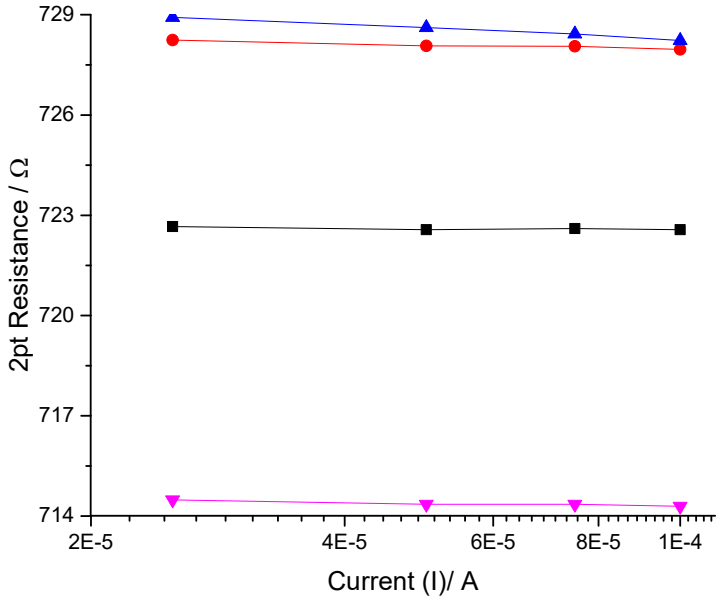

Figure B 5. 2pt resistance measured at 20 K for the capped Sb with film thickness of 3.8 nm. Resistance is independent of current confirming that the contacts are ohmic.

Appendix C: Figures Related to Chapter 7

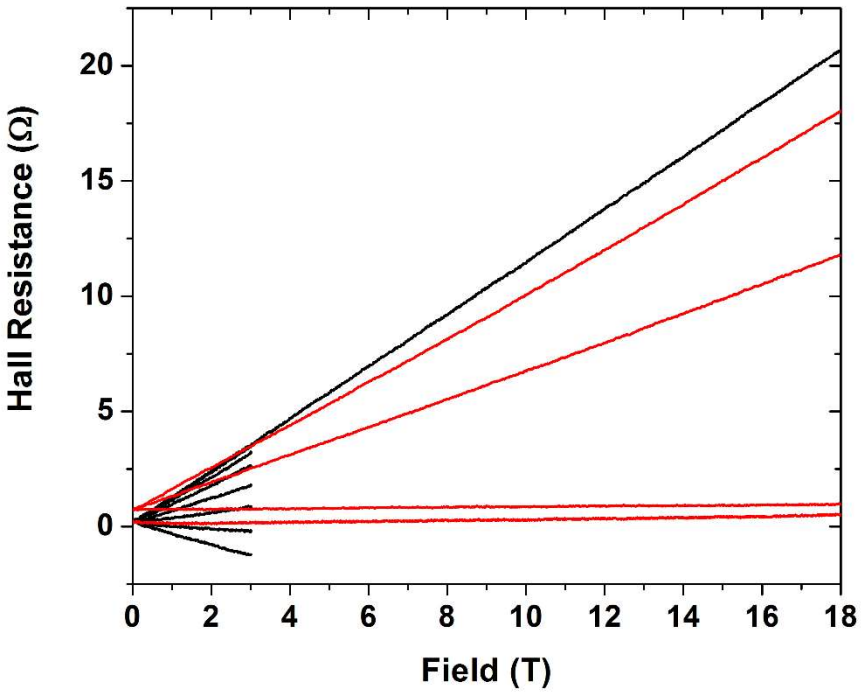

Figure C 1. Plot of Hall Resistance versus magnetic field. Hall signal is linear in the full range up to 18 T. Plot shown is for a 3.8 nm Sb QW and is representative of the Hall traces across all well thicknesses. The change in sign of the slope is due to the experimental configuration because if the field direction is flipped that changes the sign of the Hall effect. Figure is taken from Shayne's thesis [37]

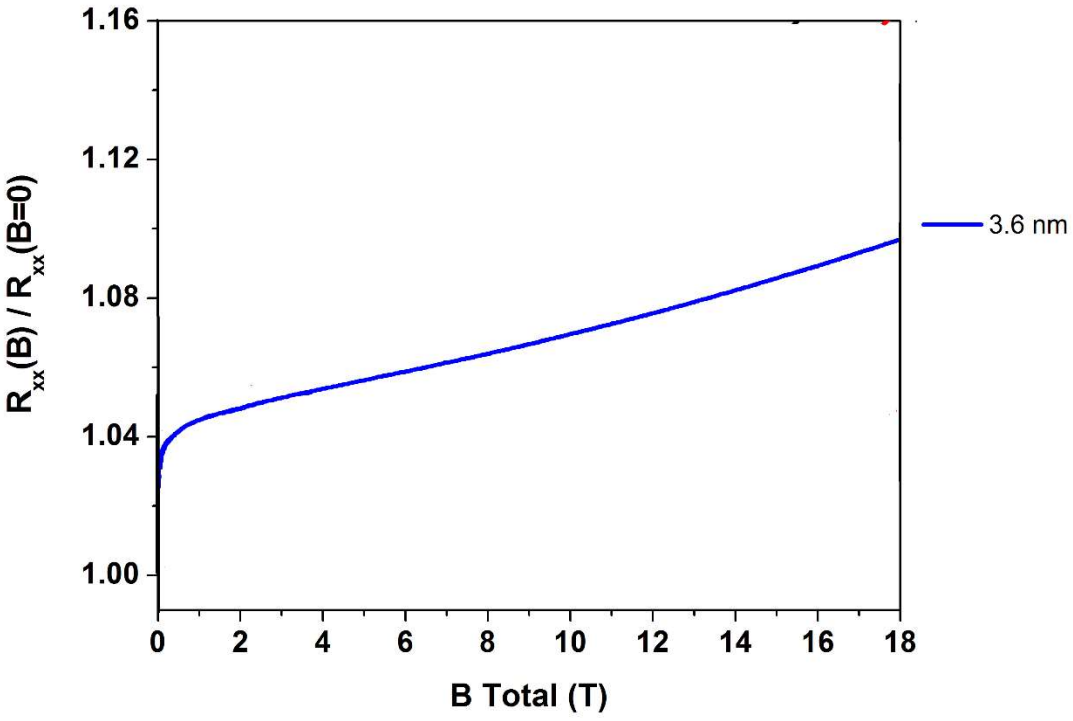

Figure C 2. High magneto resistance (MR) behavior of 3.6 nm un-doped Sb QW. Above 2 T R_{xx} shows a linear dependence with magnetic field; behavior is reported in the literature for other TI systems.

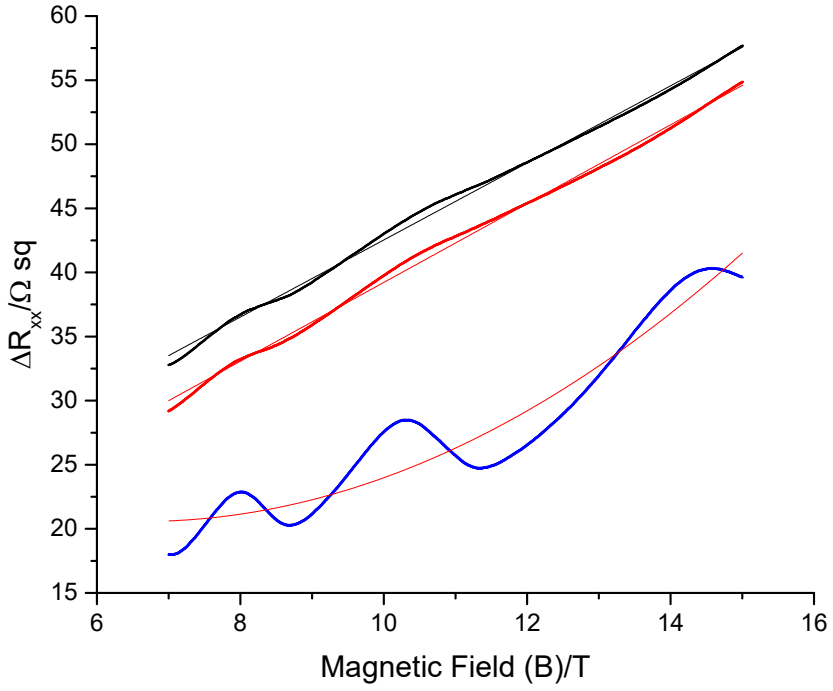

Figure C 3. Background fits for T958 (black line), T960 (red line) and T963 (blue line) for the perpendicular magnetic field.

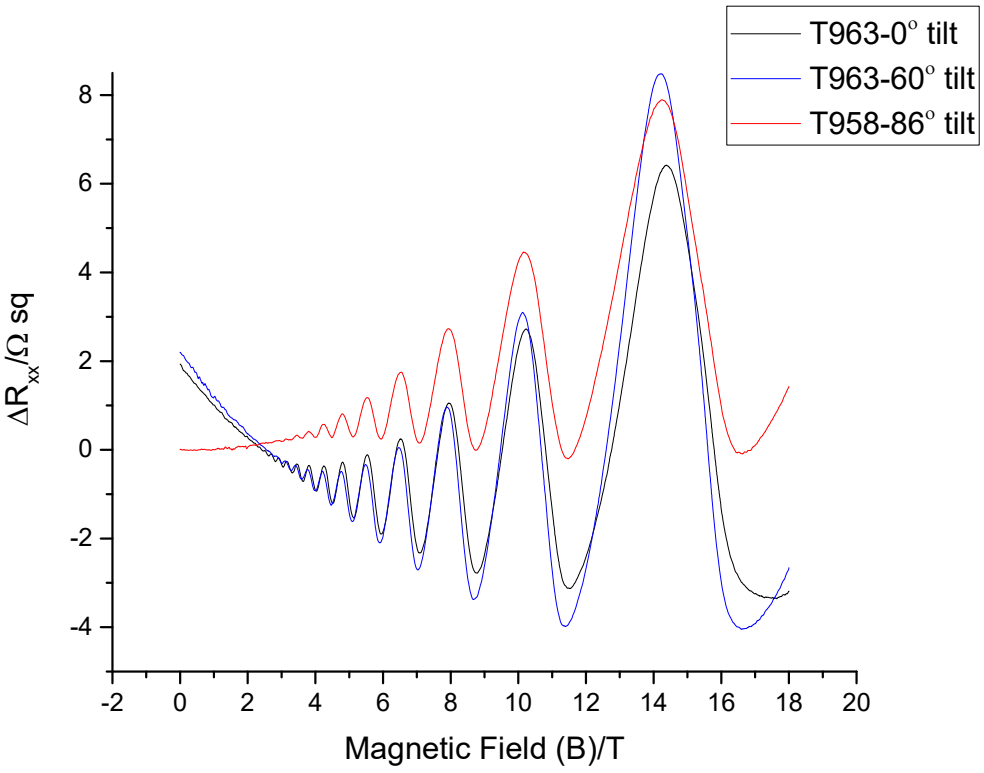

Figure C 4. Parabolic backgrounds removed for the samples T 963 and T958. Oscillations of the sample T958 in tilted field is due to the excess carries in the dopant layer; after an electron concentration of ~1.3E12 cm^{-2} is transferred to the Sb QW. The minimum of the blue curve (at ~ 16.3 T) is shifted by ~1 T with respect to the minimum of the black curve (at ~ 17.3 T). Oscillations of the T963 and T958 at tilted magnetic field coincide with each other.